Acknowledgements

I would like to thank Professor Joseph Cartwright for his extraordinary supervision and generous help in the development of this DPhil research. Special thanks to PhD. Martino Foschi, who supervised me and his continues help and support during my stay at University of Oxford at the Earth Science department to study contributions that would benefit in the successful completion of this thesis and Professor Gary M. Mavko at Stanford University for his recommendation to address part of this research work. I also want to thank professors and examiners Mike Kendall from University of Oxford and Mark Chapman from University of Edinburgh for their feedback and recommendations to improve the content in this thesis project after de VIVA exam. Thanks are extended to my sponsors CONACYT-SENER and PEMEX E&P for giving me the scholarship for the completion of my DPhil. I also want to thank Dr. Mikhail Markov, Dr. Ambrosio Aquino López and Dr. Marytere Gutierrez Guevara from Mexican Institute of Petroleum (IMP) and Dr. Ricardo Zavala Torres from Schlumberger for their guidance to tackle the effective field method (EFM) and (DEM) approach in this thesis.

The following notes posed by the exam reviewer are addressed in this document, listed as follows as part of the thesis´s corrections:

1. Anisotropic symmetry classes, particularly the relevance of orthorhombic symmetry to fractured shales

Chapter 4 (section 4.1.1)

The anisotropic symmetry systems are characterized by the constraints on the stiffness constants. If the medium is symmetric with respect to a certain coordinate transformation, then the stiffness matrix must be invariant under the same transformation.

The symmetry properties of a solid come from its physical constituents and the geometrical arrangement of those constituents. Beside spatial location, constituents themselves should be considered in describing the symmetry as irregular changes in physical properties of the constituents like density can break symmetry. However, there is no need to consider all symmetry properties of a solid for a study of every physical property (Winterstein, 1990)

The symmetry properties of the compliance tensor are the same as those of the stiffness tensor. Constraints applied to compliances are analogous to those applied to stiffnesses, however, they are not always the same.

Voigt notation should be convenient to use in representing the fourth-rank tensors for Hooke's Law. In this notation, the stress and strain tensors are written in vector form and the fourth-rank stiffness

and compliance tensors are shown using 6×6 matrices by following the Voigt rule (Nye, 1985) that $11 \rightarrow 1, 22 \rightarrow 2, 33 \rightarrow 3, 23\&32 \rightarrow 4, 13\&31 \rightarrow 5, and\ 12\&21 \rightarrow 6$

The symmetry property is an actual conceptual transformation of a solid in a way that after transformation the solid is the same as it was before transformation. The symmetry axis is a direction in a solid for which rotations of less than 360 degrees about the direction will no cause change in the solid compared to what it was before rotation (Winterstain, 1990). To identify the symmetry system, it is necessary to understand symmetries, but many interesting cases of such classification can be estimated by exploring how alteration of isotropic rocks creates members of different systems. Winterstain (1990) used a set of homogeneous parallel planar cracks introduced into homogeneous isotropic rock. Combinations of layered media and cracks also can result in different symmetries. For instance, one set of vertical fractures embedded in VTI medium leads to an orthorhombic medium.

The major symmetry systems are:

- Triclinic: As no symmetry at all. Its stiffness matrix has 21 constants.
- Monoclinic: It has a single two-fold symmetry axis, and the stiffness matrix has 13 constants
- Orthorhombic the orthorhombic system has a three orthogonal two-fold symmetry axes. The stiffness matrix has 9 constants.
- Tetragonal: It has a single 4-fold symmetry axes and seven independent constants in its stiffness matrix in general.
- Trigonal; The Trigonal system has a single 3-fold symmetry axis and seven constants in its stiffness matrix.
- Hexagonal: It has a 6-fold symmetry axis where every axis perpendicular to the 6-fold axis is a 2-fold axis and five stiffness constants are required to describe this system

- Cubic: Characterized by three stiffness constants. Its stiffness matrix has the same form as isotropic system, except that the three constants do not satisfy the equality relation governing those of an isotropic system.

Winterstain (1990) proposed five systems formed by arrangements of cracks (Table 4.1)

The symmetry plane is a plane in a solid such that reflection through this plane will cause no change in the solid (Winterstain, 1990).

Conditions:

1. Rock is initially isotropic.

2. Cracks are featureless (smooth and planar), and each crack set has an infinite fold axis, except as noted above.

3. Cracks of different sets are identical except possibly for spacing.

4.Cracks in a set are parallel or distributed symmetrically about the nominal direction.

5. Cracks in set A have spacing a, B have b, etc.

6. Each crack set fills rock uniformly.

7. Crack spacings are much less than a wavelength.

8. Vectors a, b, and d are coplanar.

9. $\alpha, \beta, \gamma, \delta$ are angles between crack plane normals.

Symmetry System	**Crack Set**	**Crack spacing**	**Crack normals**
Isotropic	(none)	N/A	N/A
TI	A	a	(Arbitrary)
Monoclinic	A,B	$a \neq b$	$\alpha \neq n * 90\ degrees, n = 0,1,2, \ldots$ $\alpha \neq n * 90\ degrees, n = 0,1,2, \ldots$
Orthorombic	A,B	$a = b$ and	

		Or $a \neq b$ and	… $\alpha = n * 90\ degrees$ $\alpha = n * 90\ degrees$
Tetragonal	A,B	$a = b$	$\alpha \neq n * 90\ degrees, n = 0,1,2, \ldots$ and
Triclinic	A,B,C	$a \neq b$	$\gamma \neq n * 90\ degrees, n = 0,1,2, \ldots$ $\alpha = \beta = \gamma = 90\ degrees$
Cubic	A,B,C		$\alpha = \beta = \gamma < 120\ degrees$
Trigonal	A,B,C		$\alpha \neq 90\ degrees$
Hexagonal	A,B,D		$\alpha = \delta = 60\ degrees$

Table 4.1. Symmetry systems and its fracture properties caused by cracks in an isotropic background. Crack set refers to a set of parallel cracks, or a distribution of crack orientations symmetrical direction (Winterstain, 1990).

Notes:

I. The hexagonal system is actually a symmetry class of the TI system.

2. The tetragonal and trigonal systems are symmetry classes of the tetragonal and trigonal systems, respectively.

3. Several conditions (listed under the diagram) are not necessary but convenient. For example, cracks of different sets would not have to be identical; but if they were not, it would be necessary to state further conditions.

In terms of stiffness matrices, the anisotropic systems are:

Triclinic system:

$$\begin{bmatrix} C_{11} & C_{12} & C_{13} & C_{14} & C_{15} & C_{16} \\ C_{12} & C_{22} & C_{23} & C_{24} & C_{25} & C_{26} \\ C_{13} & C_{23} & C_{33} & C_{34} & C_{35} & C_{36} \\ C_{14} & C_{24} & C_{34} & C_{44} & C_{45} & C_{46} \\ C_{15} & C_{25} & C_{35} & C_{11} & C_{55} & C_{56} \\ C_{16} & C_{26} & C_{36} & C_{46} & C_{56} & C_{66} \end{bmatrix} \quad (4.1)$$

21 constants

Monoclinic system:

$$\begin{bmatrix} C_{11} & C_{12} & C_{13} & 0 & C_{15} & 0 \\ C_{12} & C_{22} & C_{23} & 0 & C_{25} & 0 \\ C_{13} & C_{23} & C_{33} & 0 & C_{35} & 0 \\ 0 & 0 & 0 & C_{44} & 0 & C_{46} \\ C_{15} & C_{25} & C_{35} & 0 & C_{55} & 0 \\ 0 & 0 & 0 & C_{46} & 0 & C_{66} \end{bmatrix} \quad (4.2)$$

13 constants

Orthorhombic system:

$$\begin{bmatrix} C_{11} & C_{12} & C_{13} & 0 & 0 & 0 \\ C_{12} & C_{22} & C_{23} & 0 & 0 & 0 \\ C_{13} & C_{23} & C_{33} & 0 & 0 & 0 \\ 0 & 0 & 0 & C_{44} & 0 & 0 \\ 0 & 0 & 0 & 0 & C_{55} & 0 \\ 0 & 0 & 0 & 0 & 0 & C_{66} \end{bmatrix} \quad (4.3)$$

9 constants

Tetragonal system:

$$\begin{bmatrix} C_{11} & C_{12} & C_{13} & 0 & 0 & C_{16} \\ C_{12} & C_{11} & C_{13} & 0 & 0 & -C_{16} \\ C_{13} & C_{13} & C_{33} & 0 & 0 & 0 \\ 0 & 0 & 0 & C_{44} & 0 & 0 \\ 0 & 0 & 0 & 0 & C_{44} & 0 \\ C_{16} & -C_{16} & 0 & 0 & 0 & C_{66} \end{bmatrix} \tag{4.4}$$

7 constants

Trigonal system:

$$\begin{bmatrix} C_{11} & C_{12} & C_{13} & C_{14} & -C_{25} & 0 \\ C_{12} & C_{11} & C_{13} & -C_{14} & C_{25} & 0 \\ C_{13} & C_{13} & C_{33} & 0 & 0 & 0 \\ C_{14} & -C_{14} & 0 & C_{44} & 0 & C_{25} \\ -C_{25} & C_{25} & 0 & 0 & C_{44} & C_{14} \\ 0 & 0 & 0 & C_{25} & C_{14} & C_{11} - C_{12}/2 \end{bmatrix} \tag{4.5}$$

6 constants

Hexagonal system:

$$\begin{bmatrix} C_{11} & C_{12} & C_{13} & 0 & 0 & 0 \\ C_{12} & C_{11} & C_{13} & 0 & 0 & 0 \\ C_{13} & C_{13} & C_{33} & 0 & 0 & 0 \\ 0 & 0 & 0 & C_{44} & 0 & 0 \\ 0 & 0 & 0 & 0 & C_{44} & 0 \\ 0 & 0 & 0 & 0 & 0 & C_{11} - C_{12}/2 \end{bmatrix} \tag{4.6}$$

5 constants

Cubic system:

$$\begin{bmatrix} C_{11} & C_{12} & C_{12} & 0 & 0 & 0 \\ C_{12} & C_{11} & C_{12} & 0 & 0 & 0 \\ C_{12} & C_{12} & C_{11} & 0 & 0 & 0 \\ 0 & 0 & 0 & C_{44} & 0 & 0 \\ 0 & 0 & 0 & 0 & C_{44} & 0 \\ 0 & 0 & 0 & 0 & 0 & C_{44} \end{bmatrix} \tag{4.7}$$

3 constants

Different distributions of fractures and their orientation may result in different anisotropic systems. The anisotropic properties can be studies using seismic surface, VSP or other techniques in the geophysical field to identify fractured regions.

Orthorhombic symmetry for shales

Orthorhombic symmetry is commonly formed by embedding a set of parallel vertical fractures in the VTI background (Figure 4.1) or by embedding two sets of orthogonal and vertical fractures in either an isotropic or VTI background. Can be forms as well by combining two sets of conjugate fractures dipping with angle θ and $-\theta$ (Reiss, 1980; Nelson, 1985; Sayers, 2022).

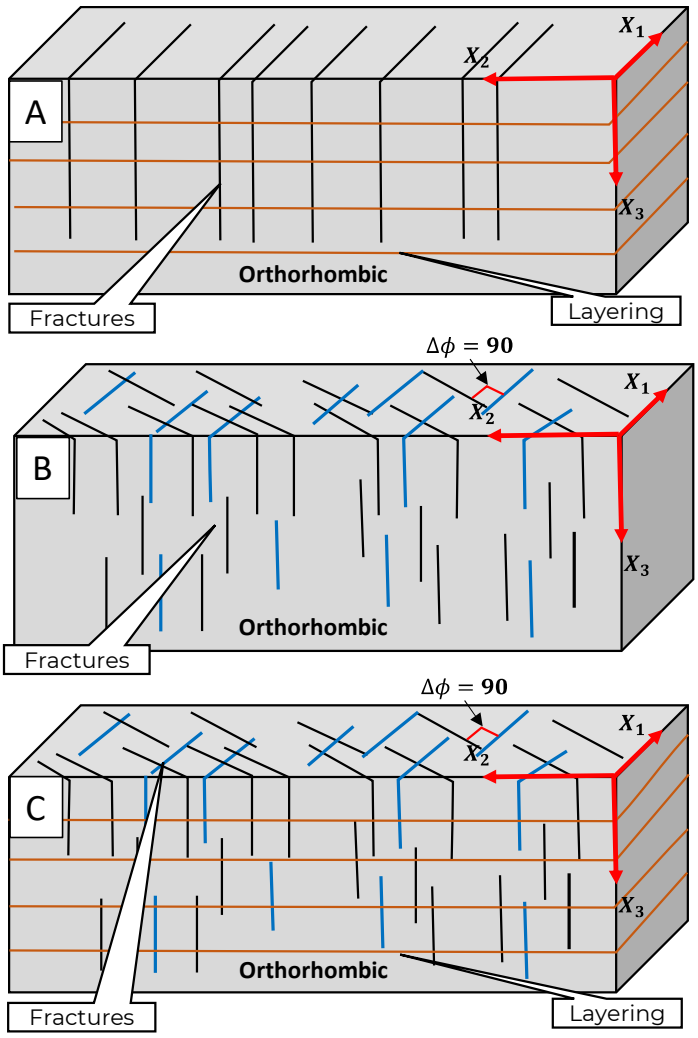

Figure 4.1 Orthorhombic symmetry is commonly formed by embedding a set of parallel vertical fractures in VTI background.

In general shales exhibit VTI anisotropy due to bedding planes, thin layers with preferred alignment of clay platelets and organic materials, and horizontal cracks or fractures (Thomsen, 1986; Wang, 2002). The interfaces can be treated as linear-slip interfaces where discontinuity is linearly dependent on the traction vector on the interface (Schoenberg, 1980).

In sedimentary basins, orthorhombic symmetry is commonly caused by parallel vertical fractures embedded within a VTI background medium (Figure 1b). It may also arise due to two or three mutually orthogonal fracture sets, or due to two identical fracture systems cross-cutting one another with an arbitrary angle (Tsvankin,1997). Such sets of fractures are common, e.g., for thick sandstone

beds and granites. Bakulin et al. (2000b) conclude that orthorhombic symmetry thus might be the most realistic symmetry for many geophysical problems. Despite this conclusion, the application of orthorhombic anisotropy in seismic inversion and processing is impeded by the large number (nine) of independent entries of the stiffness matrix. Moreover, if the orientation of the symmetry planes is unknown, as it is usually the case in seismic field experiments that the number of unknowns increases to 12, since the angles between the symmetry planes and the coordinate planes of the reference observation system must be determined additionally.

2. Assumptions and limitation, models Ruger Thomsen and Backus Averaging

Chapter 4 (section 4.2.4)

Inversion aims to determine the characteristics of causal features by analyzing the effects these features produce. In geophysics, inverse problems generally aim to characterize some subsurface property, for example seismic wave velocity or density, by analyzing a set of observations where the desired parameter(s) induce some causal effect, for example a set of features present in seismic data. In this work, parameters that characterize fractures, namely fracture density and fracture orientation, are the desired earth parameters to be inverted. A 3D seismic dataset constitutes the set of observations that are to be analyzed to invert for these fracture characteristics. In any inverse problem, a proper understanding of the forward problem is crucial.

The forward problem specifies how changes in the desired model parameters alter certain observations. The forward problem allows one to generate synthetic data based on a certain set of parameters. The synthetic data is then compared to the real data.

The parameters associated with the synthetic dataset that most closely match the real data are considered to be the most likely parameters, i.e., the "answer" to the inverse problem. Depending on the problem, finding this set of "best-fit" parameters might be an iterative process. The forward problems associated with the methods used in this work will be examined in detail in Chapters 4 and 5; however, in the interest of providing the theoretical framework for inversion, the following assumptions are necessary.

The Rüger method is based on in the approximation on the Rüger AVO reflectivity in the HTI media (Rüger, 1997; Rüger and Tsvankin, 1997) in the equation addressed in Chapter 5 eq. 5.1. This equation is modification of the two term conventional AVO equation, shown in the Shuey Equation for normal AVO. With addition of an azimuthally varying gradient term (B*ani*).

Variables A, $B_{iso}$and B_{ani}can be postulated in terms of elastic properties of the effective media generating the reflectivity (Rüger, 1997).

Rüger and Tsvankin (1997) conducted a thorough analysis showing that eq. 5.1 is an acceptable approximation to exact reflectivity in HTI media at relatively small incident angles (i.e., less than ~30 degrees) under the assumption of small jumps in reflectivity across the layer interface, arbitrarily weak anisotropy, and subcritical incident angles. Figure 4.6 shows for an evaluation of how Eq. 5.1 compares to exact expressions for reflectivity in isotropic, fluid filled fracture, and dry fracture end-cases.

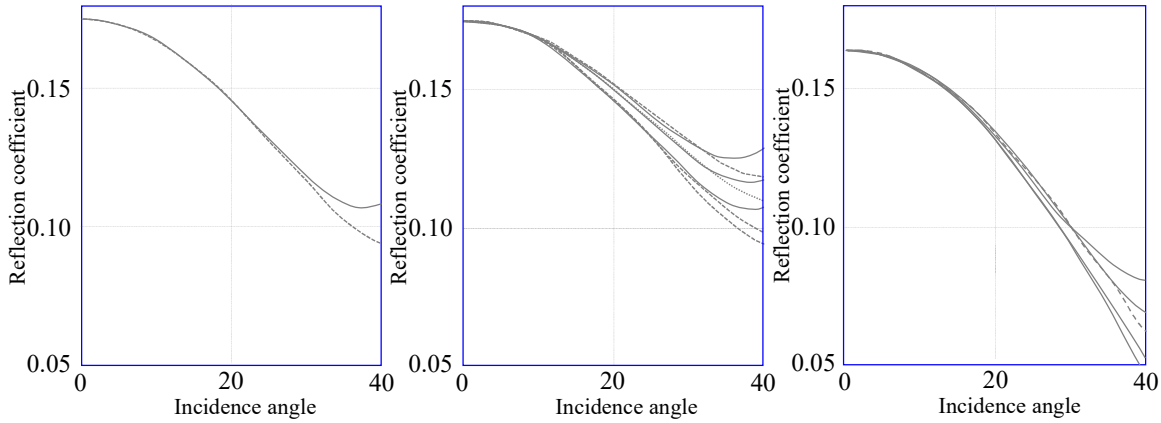

Figure 4.6 Comparison of exact and approximate reflectivity calculated using the Rüger AVO equation shown in eq 5.1. In all images the solid line represents exact reflectivity, and the dashed line represents approximated reflectivity. The leftmost image depicts the isotropic case. The middle image depicts the HTI case associated with fluid filled fractures. The rightmost image depicts the HTI case associated with dry fractures. The X axis represents incident angle, and the Y axis represents reflectivity.

Linearization of eq. (5.1) is performed using the method proposed by Xu and Li (2002), which utilizes trigonometric identities. In this context the Ruger Equation acts as a linear forward operator, and thus can be rewritten as:

$$\begin{pmatrix} R(\theta_1,\varphi_1) \\ R(\theta_2,\varphi_1) \\ \vdots \\ R(\theta_N,\varphi_1) \\ R(\theta_1,\varphi_2) \\ R(\theta_2,\varphi_2) \\ \vdots \\ R(\theta_N,\varphi_2) \\ \vdots \\ R(\theta_N,\varphi_n) \end{pmatrix} = \begin{pmatrix} 1 & sin^2(\theta_1) & -cos(2\varphi_1)sin^2(\theta_1) & -sin(2\varphi_1)sin^2(\theta_1) \\ 1 & sin^2(\theta_2) & -cos(2\varphi_1)sin^2(\theta_2) & -sin(2\varphi_1)sin^2(\theta_2) \\ \vdots & \vdots & \vdots & \vdots \\ 1 & sin^2(\theta_N) & -cos(2\varphi_1)sin^2(\theta_N) & -sin(2\varphi_1)sin^2(\theta_N) \\ 1 & sin^2(\theta_1) & -cos(2\varphi_2)sin^2(\theta_1) & -sin(2\varphi_2)sin^2(\theta_1) \\ 1 & sin^2(\theta_2) & -cos(2\varphi_2)sin^2(\theta_2) & -sin(2\varphi_2)sin^2(\theta_2) \\ \vdots & \vdots & \vdots & \vdots \\ 1 & sin^2(\theta_N) & -cos(2\varphi_2)sin^2(\theta_N) & -sin(2\varphi_2)sin^2(\theta_N) \\ \vdots & \vdots & \vdots & \vdots \\ 1 & sin^2(\theta_N) & -cos(2\varphi_n)sin^2(\theta_N) & -sin(2\varphi_n)sin^2(\theta_N) \end{pmatrix} \begin{pmatrix} A \\ B \\ C \\ D \end{pmatrix} \qquad (4.15)$$

where there are N incident angle bins, n azimuthal bins and $N * n$ data points at each location

After matrices in Equation 4.15 have been populated with specific values corresponding to the azimuthal and incident angle binning scheme used in the analysis, data vector $\boldsymbol{m}$ can be solved using the standard least squares approach. This is repeated at every Common Depth Point (CDP) location and every time sample. After linearized coefficients A, B, C and D are found the coefficients are calculated shown in eq. (5.1), namely A, B_{iso}, $B_{ani}$and φ_{iso}.

φ_{iso}represents the azimuthal isotropy plane, and it is an indicator of fracture strike. Analysis of Equation 4.1 shows that at azimuth $\varphi = \varphi_{iso}$, reflectivity is at a local minimum with respect to azimuth. B_{ani} represents the magnitude of the azimuthal variation, and it is a direct indicator of fracture density. This agrees well with the intuitive notion that denser fracture spacing will result in a larger difference in seismic waves when compared to waves travelling parallel to those traveling perpendicular to fracture strike. Note that seismic trace amplitude data was used in lieu of reflectivity because true impedances of the section are unknown.

Trace amplitude is roughly proportional to reflectivity, but this substitution limits inverted fracture density to be relative, rather than absolute. In general, the fracture number per unit length cannot be found, but areas of relatively high and relatively low fracture density can be identified. Unfortunately, substituting seismic amplitude for reflectivity is unavoidable in the analysis of real data.

Regrettably, the Rüger method presented above is fundamentally flawed. This comes largely from the linearization process used to make solving the problem computationally feasible. This leads to an inherent sign ambiguity in $B_{ani}$and thus an inherent inability to differentiate between the "fast" direction (parallel to φ_{iso}) and the "slow" direction (perpendicular to φ_{iso}).

The sign ambiguity in B_{ani} also indicates that the azimuth $\varphi = \varphi_{iso}$could correspond to either a local maximum or a local minimum in seismic data with respect to azimuth. In practice, this sign ambiguity leads to an inherent 90-degree ambiguity in φ_{iso}, and thus an inherent 90-degree ambiguity in determining fracture azimuth. This 90-degree ambiguity can also be seen by examining equation,

noting that tan (2 φ_{iso})is 180 degrees periodic and thus will not be affected by any 90 degree change in φ_{iso}. This 90-degree ambiguity in fracture azimuth poses serious problems for well orientation planning and in effect makes the Rüger method unusable for determining fracture azimuth without further modification. Partially for this reason, an alternate HTI method was implemented which utilizes Fourier decomposition of the seismic data.

In the Thomsen fracture model, the HTI anisotropy (Figure 4.7) is assumed to be caused by parallel fracturing and where the reflectivity modeling assumes an overlying isotropic layer. This is considered reasonable for potential reservoirs with typically more homogeneous seal units above.

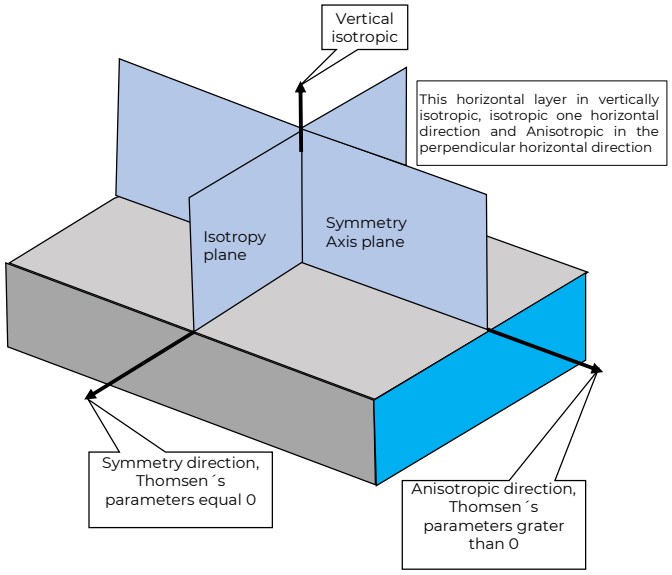

Figure 4.7 Thomsen´s model fractured HTI anisotropy.

Thomsen model

Chapter 4 (section 4.2.4.1)

Thomsen model

The theories of Hudson (1981) and Thomsen (1995) were designed for specific physical fracture models involving penny-shaped cracks and can be used to express Δ_N and $\Delta_T$through parameters that are dependent on the microstructure of cracks and pores.

Although determination of these microstructural parameters from seismic data requires additional information about the medium, both Hudson's and Thomsen's models are helpful in guiding the interpretation of the weaknesses in terms of the crack density and fluid content. Vertical, parallel, rotationally invariant fractures lead to a particular type of HTI media described by four independent parameters.

Thomsen-style anisotropic coefficients of HTI media $\varepsilon^{(V)}$, $\delta^{(V)}$,and $\gamma^{(V)}$ can be obtained in terms of the weaknesses Δ_N and $\Delta_T$and the Vp/Vs ratio in the background medium. One of the anisotropic parameters ($\varepsilon^{(V)}$, $\delta^{(V)} or\ \gamma^{(V)}$) can be found from the other two anisotropy parameters together with the Vp/Vs ratio.

$\varepsilon^{(V)}$, $\delta^{(V)}$,and $\gamma^{(V)}$in any fracture induced HTI model are always negative, while the anellipticity parameter $\eta^{(V)}$is predominantly positive.

All possible pairs $[\varepsilon^{(V)}, \delta^{(V)}]$ for HTI models resulting from parallel vertical fractures belong to a relatively narrow area with a quasi-triangular shape on the $[\varepsilon^{(V)}, \delta^{(V)}]$-plane These results can be used to identify fracture-induced HTI media from seismic measurements.

In the linearized weak-anisotropy approximation, all anisotropic parameters are proportional to the crack density, with the coefficients controlled by the Vs/Vp ratio and, for $\varepsilon^{(V)}$and $\delta^{(V)}$, fluid saturation.

The shear-wave splitting parameter $|\gamma^{(V)}|$ for dry or fluid-filled cracks and a wide range of the Vs/Vp ratios remains close to the crack density. Therefore, the travel times or reflection amplitudes of split S-waves at vertical incidence are strongly dependent on the degree of fracturing but cannot be used to discriminate between dry and fluid-filled cracks.

Backus Average

Chapter 4 (section 4.2.4.2)

The Backus average yields accurate replications of borehole acoustic logs that hinge on the formation elastic properties, wavelength and on the acoustic mode applied. Marion et.al. (1994), Liu and Schmitt (2006), and Mavko et al. (2009) propose that the transition from ray to effective medium theories for ultrasonic waves propagating in a stack of horizontal layers occurs when the thickness of the layers is approximately 10 times smaller than the wavelength.

The Backus averaging method (1962) presents analytical expressions for equivalent elastic properties of a stack of thin layers. the individual layers may be isotropic, TIV, TIH, Orthorhombic, or monoclinic (Kumar, 2013). The Backus and Hudson (1980) models are, respectively, the common models used for upscaling and for crack induced anisotropy modeling. As stated by Saberi (2017)

"Backus showed that at the long wavelength limit, a stratified medium composed of isotropic layers will behave like a transverse isotropic (TI) medium and derived the effective elastic constants for such a medium.

Hudson (1980) derived the effective elastic constants of a cracked medium by modeling an isotropic background superimposed with oriented cracks. This model is quite commonly used in carbonates for modeling fracture effects on velocities and modeling azimuthal inversion studies for fracture characterization.

Chapter 4 (section 4.3.1)

Figure 4.10 and **Figure 4.11** have been changed updated using DEM theory applied to estimate the elastic moduli

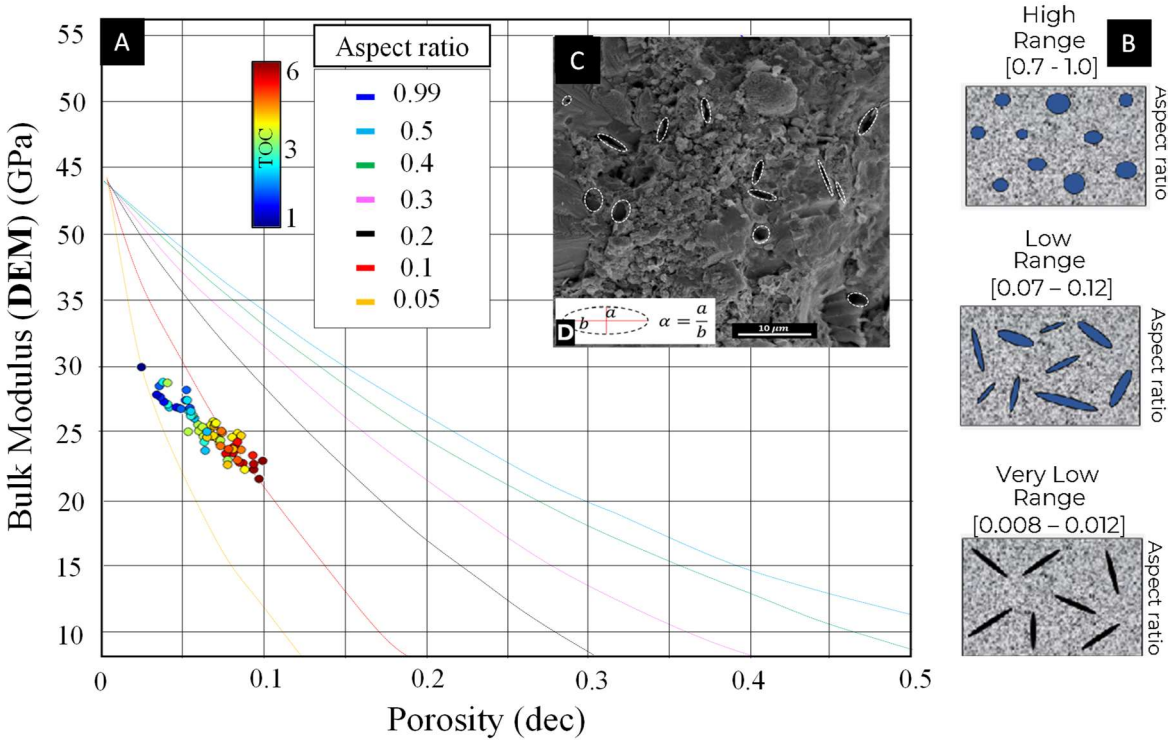

Figure 4.10 (A) Bulk modulus varying with porosity ϕ at Anhelido-1 showing the influence of pore aspect ratio in the Pimienta Formation with logging data (Porosity ϕ) overlapped the average value of aspect ratio between (0.1-0.2) approximately according with this graph; (B) Aspect ratio near to 1.0 increases Bulk modulus for a given porosity (Russell and Smith, 2007); (C) SEM photograph of a sample with ellipsoidal cracks of the mid unit of the Pimienta Formation in analogue well; (D) Graphical definition of pore aspect ratio.

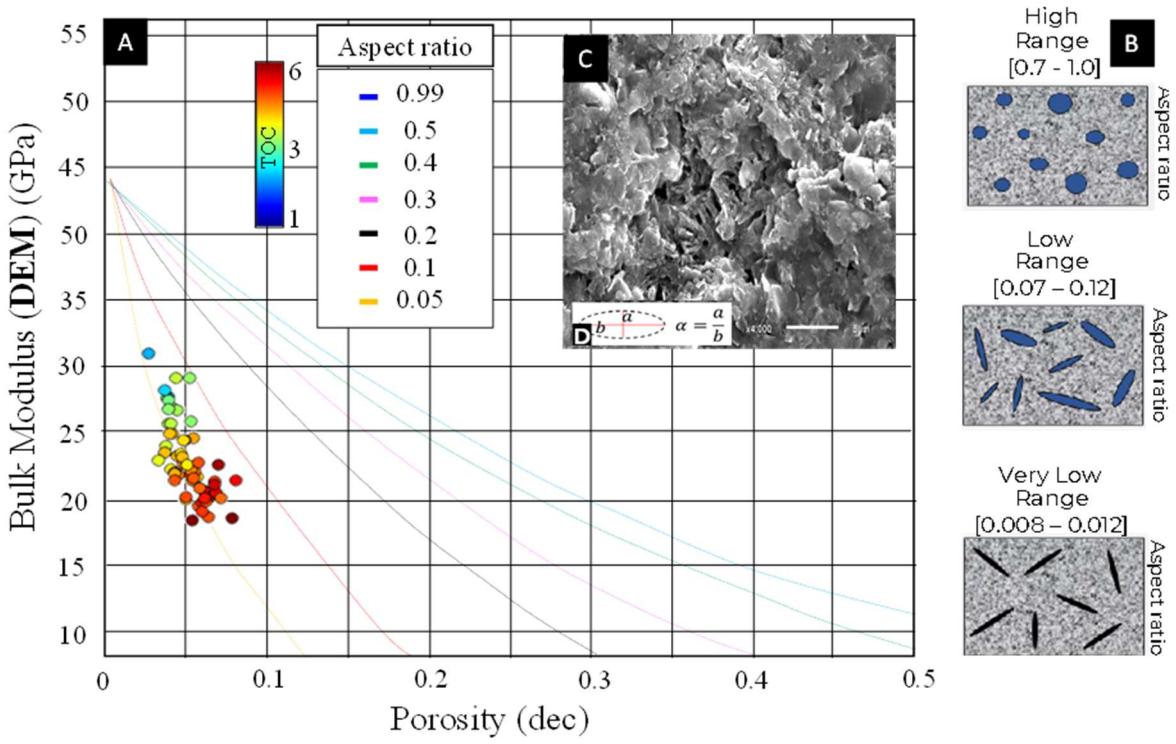

Figure 4.11 (A) Bulk modulus varying with porosity ϕ at Serbal-1showing the influence of pore aspect ratio in the Pimienta Formation with logging data (Porosity ϕ) overlapping with the average value of aspect ratio between (0.04-0.16) approximately according with this graph; (B) Aspect ratio near to 1.0 increases P-wave velocity for a given porosity (Russell and Smith, 2007); (C) SEM photograph of a sample at Serbal-1 with ellipsoidal crack of the mid unit of Pimienta Formation; (D) Graphical definition of pore aspect ratio.

The Thomsen´s parameters (Hudson's Model) have been corrected in Anhelido-1 and Serbal-1 as follows:

The parameters below were used to compute the anisotropy values for the cracked model (Hudson Model).

Depth = 2013m Anhelido-1(Pimienta Formation)

Gives

$V_p\ (dry)(^m/_s)$ = 4742
$V_p\ (dry)(^m/_s)$ = 3292
$Rho(gr/cc)$ = 2.59
e= 0.03
α=0.1
$Crack\ \phi$=0.03
Effective ϕ=0.06

Anisotropic parameters

$\boldsymbol{\varepsilon}$	$\boldsymbol{\gamma}$	$\boldsymbol{\delta}$
-0.08	-0.04	-0.07

Depth = 2908 Serbal-1(Pimienta Formation)

Gives

Input data

$V_p\ (dry)(^m/_s)$ = 3877
$V_p\ (dry)(^m/_s)$ = 2689
$Rho(gr/cc)$ = 2.35
e= 0.04
α=0.1
$Crack\ \phi$=0.023
Effective ϕ=0.05

Anisotropic parameters

$\boldsymbol{\varepsilon}$	$\boldsymbol{\gamma}$	$\boldsymbol{\delta}$
-0.10	-0.05	-0.10

Chapter 4 (section 4.3.2)

The Thomsen´s parameters (Linear-slip Model) have been corrected in Anhelido-1 and Serbal-1 as follow:

For Fractured Media (Linear-slip model)

Depth = 2013m Anhelido-1 (Pimienta Formation)

Gives

Input data

$V_p\,(dry)(^m/_s)$ = 4742
$V_p\,(dry)(^m/_s)$ = 3292
$Rho(gr/cc)$ = 2.59
$Z_N = 0.034$
$Z_T = 0.035$

Anisotropic parameters

$\boldsymbol{\varepsilon}$	$\boldsymbol{\gamma}$	$\boldsymbol{\delta}$
-0.01	-0.05	-0.13

Depth = 2908m Serbal-1 (Pimienta Formation)

Gives

Input data

$V_p\,(dry)(^m/_s)$ = 3877
$V_p\,(dry)(^m/_s)$ = 2689
$Rho(gr/cc)$ = 2.35
$Z_N = 0.056$
$Z_T = 0.058$

Anisotropic parameters

$\boldsymbol{\varepsilon}$	$\boldsymbol{\gamma}$	$\boldsymbol{\delta}$
-0.02	-0.05	-0.11

Due to the changes in Thomsen parameters in Hudson´s and Linear-slip models all the synthetic seismic modelling has been changed and these are embedded into the main body of the thesis.

3. Clarification of the wavefronts/slowness surfaces shown particularly with references to gaps in the curves

Chapter 4 (section 4.3.4)

The wave fronts and slowness surfaces have been updated according with the Thomsen parameters for Hudson and linear-slip model

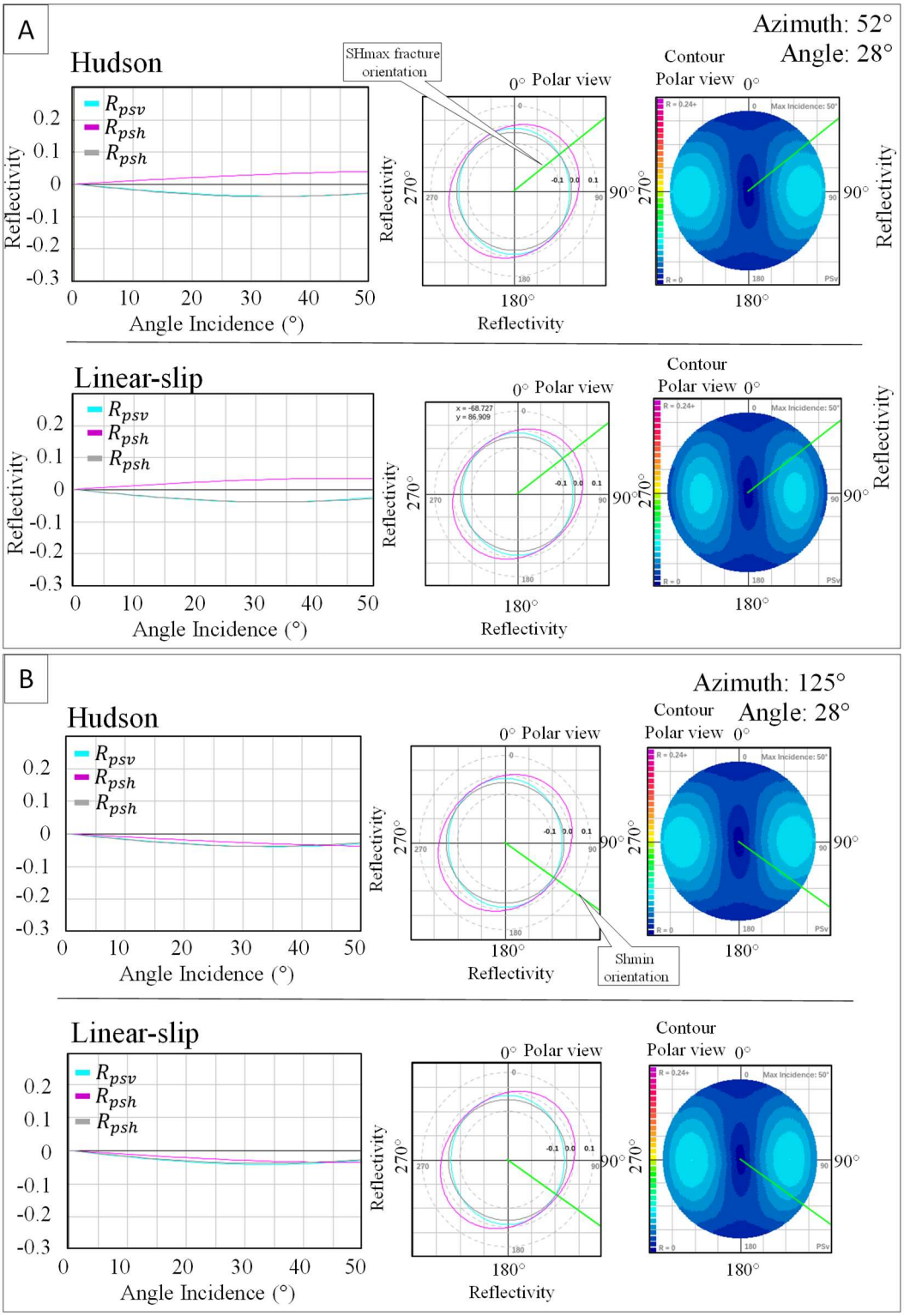

Figure 4.23 (A) Blocky models using the fracture models (Hudson and Linear-slip) parallel to stress SHmax and fractures, AVO curves of wave field R_{psv}, R_{psh}, and R_{ps-I} and its polar view, green line represent stress-fracture direction in azimuth according with the stress map (52° and 66°); (B) Blocky models using the fracture models (Hudson and Linear-slip) perpendicular to stress SHmax and fractures, AVO curves of wave field R_{psv}, R_{psh}, and R_{ps-Iso} and its polar view, green line represent Shmin direction in azimuth (114° and 125°).

The anisotropic phase velocity for the Pimienta Formation has thus far been obtained in both vertical transverse isotropy (VTI) and horizontal transverse isotropy (HTI) for the velocity of the waves $R_{psv}, R_{psh}, and\ R_{ps-Is}$ in (Blocky Ops) using the RokDoc software.

In the Figures, 4.24 and 4.25 at Anhelido-1 (2113 m depth) and in the Figures 4.26 and 4.27 at Serbal-1 (2908 m depth) the propagation for the R_{psv}, R_{psh}, and R_{ps-} reflectivity waves are displayed assuming VTI and HTI medium within the Pimienta Formation. For this purpose, I used the values corresponding to Hudson and Linear-slip models in both wells as input data in RokDoc software which has a module that can perform these calculations.

The anisotropic values were:

Thomsen's parameters from Hudson: $\varepsilon = -0.26, \gamma = -0.12, \delta = -0.26$ and the velocities for dry case

($\mathrm{v}_p = 4242\,{}^{m}/_{s}$ $\mathrm{v}_s = 3292\,{}^{m}/_{s}$).

Linear-slip: $\varepsilon = -0.071, \gamma = -0.13, \delta = -0.25$ and the velocities for dry case

($\mathrm{v}_p = 4242\,{}^{m}/_{s}$ $\mathrm{v}_s = 3292\,{}^{m}/_{s}$).

For Hudson's Model:

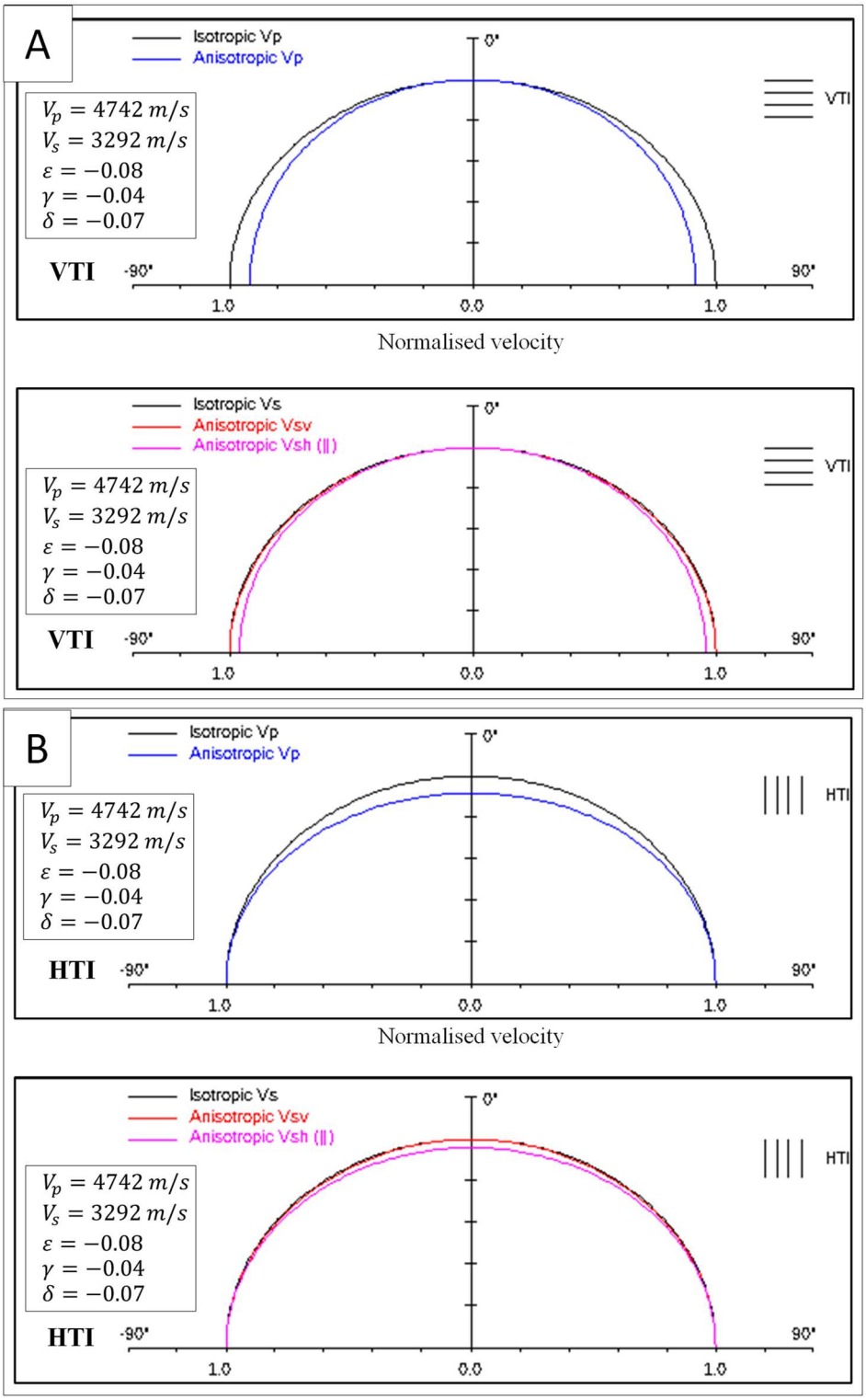

Figure 4.24 (A) Anisotropic wave propagation for given anisotropic parameters in VTI mode within the Pimienta Formation at Anhelido-1 using Hudson's Model; (B) Anisotropic wave propagation for given anisotropic parameters in HTI mode within the Pimienta Formation at Anhelido-1 using Hudson's Model.

Linear-slip gives

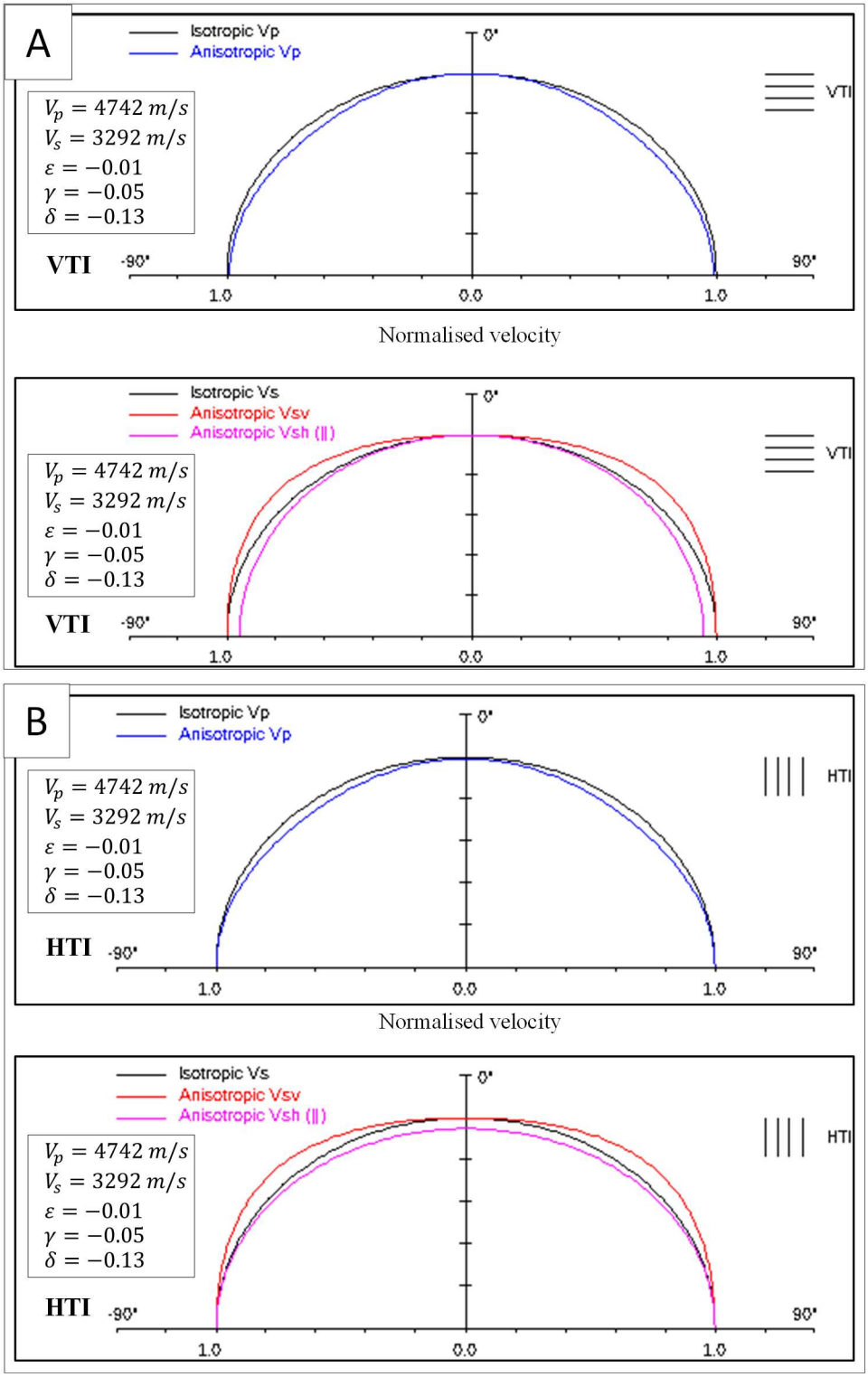

Figure 4.25 (A) Anisotropic wave propagation for given anisotropic parameters in VTI mode within the Pimienta Formation at Anhelido-1 using Linear-slip Model; (B) Anisotropic wave propagation for given anisotropic parameters in HTI mode within the Pimienta Formation at Anhelido-1 using Linear-slip model.

In Serbal-1 the anisotropic values were:

Hudson: $\varepsilon = -0.69, \gamma = -0.34, \delta = -0.69$ and the velocities for dry case

($v_p = 3877\, {}^{m}/_{s}$ $v_s = 2689\, {}^{m}/_{s}$).

Linear-slip: $\varepsilon = -0.18, \gamma = -0.34, \delta = -0.66$ and the velocities for dry case

($v_p = 3877\, {}^{m}/_{s}$ $v_s = 2689\, {}^{m}/_{s}$).

Serbal-1 depth:2908m Phase velocity plots

For Hudson Model gives:

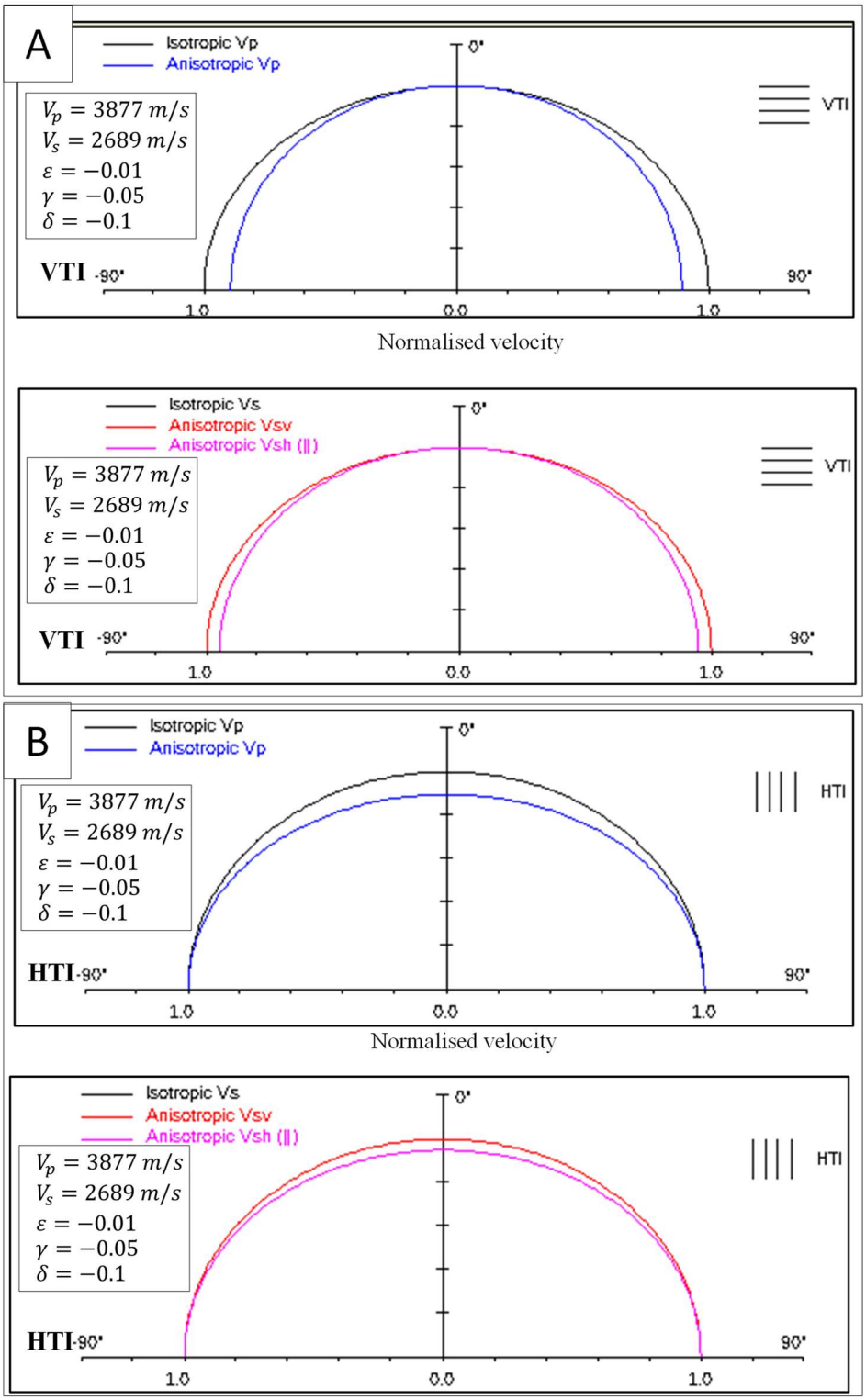

Figure 4.26 (A) Anisotropic wave propagation for given anisotropic parameters in VTI mode within the Pimienta Formation at Serbal-1 using Hudson's Model; (B) Anisotropic wave propagation for given anisotropic parameters in HTI mode within the Pimienta Formation at Serbal-1 using Hudson's Model.

For Linear-slip model gives:

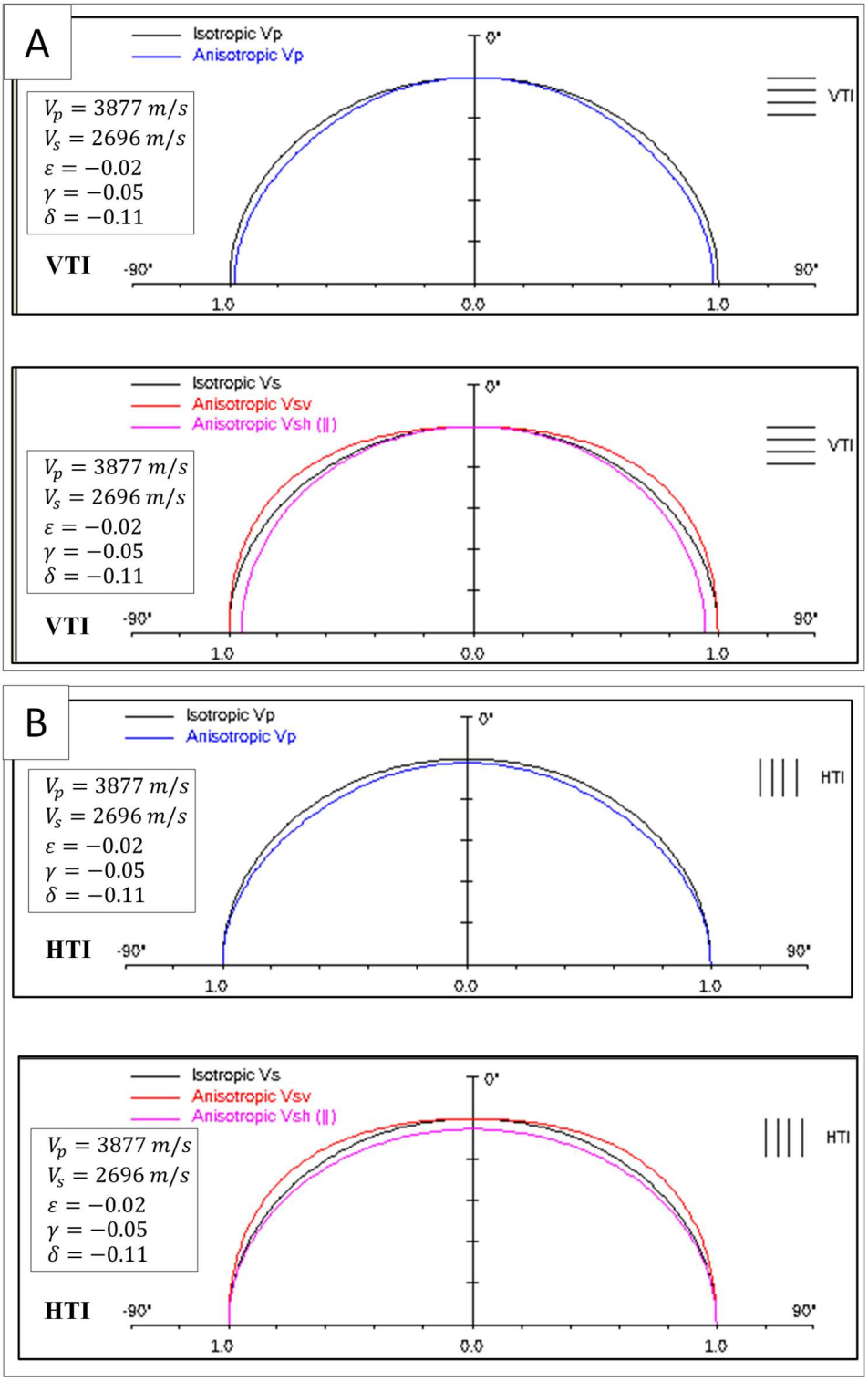

Figure 4.27 (A) Anisotropic wave propagation for given anisotropic parameters in VTI mode within the Pimienta Formation at Serbal-1 using Linear-slip Model; (B) Anisotropic wave propagation for given anisotropic parameters in HTI mode within the Pimienta Formation at Serbal-1 using Linear-slip model.

4. Links and comparisons between the various fracture models, interpretation of fracture compliances in the linear slip theory

Chapter 4 (section 4.3.5)

This thesis project has documentation that demonstrates the validity of these models and the relationship between them. Hsu and Schoenberg (1993) made measurements in simulated fractured media to test the assumptions of the linear slip model. They found that the linear slip theory agreed well with laboratory measurements. In this chapter, I explore the main results of Hudson's (1981, 1997) laboratory measurements using theoretical predictions from his penny crack model. The objective is to analyze the validity of the relationship between the linear slip model and the penny-shaped crack model.

For this purpose, I will consider the experiment of Hsu and Schoenberg (1993) described here, in which they measured the velocity in a rough-surfaced plexiglas plate, pressed together with static normal stress, to simulate a fractured medium.

In the experiment, the third axis is orthogonal to the fracture surface, the effective average model is VTI (transverse isotropy, vertical axis of symmetry). Measurements perpendicular, parallel and oblique to the crack showed that, for wavelengths greater than the single thickness of the plate, the plexiglass plate can be modeled as a specific type of VTI media that depends on four parameters: normal fracture compliance and tangential and two an isotropic background module. This behavior of a VTI medium is identical to that of an embedded isotropic solid with a set of parallel linear slip interfaces.

Under this assumption, the elastic stiffness matrix of the effectively fractured medium can be derived based on only four measurements of the velocities of the P and S waves, polarized parallel and perpendicular to the fracture plane. However, for the linear slip assumption, an additional constraint must be satisfied (eq. 4.31).

$$C_{11}C_{33} - C_{13}^2 = 2C_{44}(C_{11} + C_{13}) \quad (4.31)$$

In their experiments, Hsu and Schoenberg fitted a TI model to five different measurements made under different pressure regimes to obtain five elements of the stiffness matrix.

$(C_{11}, C_{33}, C_{44}C_{66}, C_{13})$.

Table 4.6 shows the five VTI moduli. Normalized by the density of the bulk lucite, determined from the five ultrasonic measurements of velocities. These velocities were performed at different stress states, from 6MPa to 24MPa.

To confirm the linear slip theory, they again predict the off-diagonal terms of the $C_{13}^{'}$ stiffness matrix using the equivalent equation 2.17 for a model with a vertical axis of symmetry, based only on measurements ($C_{11}, C_{33}\ and\ C_{66}$) values of the $C_{13}^{'}$, normalized by density are in column number 7 of Table 4.6.

Stress (Mpa)	C11/ρ (Mpa m3/Kg)	C33/ρ (Mpa m3/Kg)	C44/ρ (Mpa m3/Kg)	C66/ρ (Mpa m3/Kg)	C13/ρ (Mpa m3/Kg)	C13′/ρ (Mpa m3/Kg)
6	6.65	4.49	1.51	1.85	2.2	2.22
12	6.97	5.47	1.66	1.85	2.65	2.7
18	7.07	5.95	1.74	1.86	2.86	2.98
24	7.12	6.15	1.76	1.86	3.02	3.07

Table 4.6 Elastic stiffness coefficient in VTI mode from the experiment.

In the next step in the experiment, they derived the excess compliances (normal and tangential) caused by fractures ($E_N\ and\ E_T$). These compliances decrease with increasing stress which means that the asperities on either side of the plates are closer, implying that the contact area is increasing on the fracture surface.

The laboratory measurements and their fit are summarized to a linear-slip theory for all stress states previously mentioned as derived by Hsu and Schoenberg (Table 4.6). the velocities V_p *and* V_s are inverted for the unfractured Lucite block. The normal compliance E_N is estimated using the P-wave propagation perpendicular to the fractures and the S-wave velocity polarized parallel to the fractures (Table 4.7).

Stress (Mpa)	Vs(m/s)	E_T	Vp(m/s)	E_N	Vp´(m/s)	$E_{N'}$
6	1363	0.22	2703	0.62	2.71	0.63
12	1363	0.11	2686	0.31	2.73	0.36
18	1364	0.06	2679	0.2	2.73	0.25
24	1365	0.05	2707	0.19	2.73	0.21

Table 4.7. $V_p^{'}$ and $E_N^{'}$ are estimated from P-wave velocities propagating orthogonal and parallel to the fractures and the wave parallel to the fractures regarded to lucite block.

I investigated the relationship between the Hudson model (1981) and linear-slip using this method and a volumetric distribution. Using data from rock mechanics within the Pimienta Formation from four samples taken at various depths and confining pressures (Table 4.8), I also model the variation of the relative area of cracking of the surface of the fractures with increasing stress. This is done using Hudson's model (1997) with a planar distributions of cracks.

Depth (m)	sample	Vp(m/s)	Vs(m/s)	confined pressure (psi)	density(gr/cc)	v	E(Gpa)
2104	1	4248	2456	0	2.38	0.25	26.84
2108	2	4369	2528	500	2.35	0.25	26.37
2114	3	4325	2441	1000	2.55	0.26	31.55
2121	4	4005	2337	1500	2.59	0.26	41.12

Table 4.8. Rock mechanics data within Pimienta Formation, static measurement of Young´s Modulus and Poisson´s ratio.

For the estimation of crack densities using Hudson's penny-shaped model using the samples information at different depths of the Pimienta Formation, I use Equation 4.32 and Equation 4.33 to explore the equivalence between the linear-slip and Hudson's model for dry cracks to obtain the relation between fracture weaknesses and crack density for dry cracks.

$$\Delta_N = \frac{4e}{3g(1-g)} \tag{4.32}$$

$$\Delta_T = \frac{16e}{3(3-2g)}$$

The $\Delta_N and\ \Delta_T$ are not independent and Δ_N in terms of Δ_T are related in following form:

$$\Delta_N = \frac{3-2g}{4g(1-g)}\Delta_T = \frac{(2-v)(1-v)}{(1-2v)}\Delta_T \tag{4.33}$$

I obtain two different values for crack density using both weaknesses values which must satisfy the next conditions:

$$0 < \Delta_N < 1 \tag{4.34}$$

$$0 < \Delta_T < 1$$

$$\Delta = 0\ for\ unfractured\ rock$$

$$\Delta = 1\ rock\ that\ lost\ coherence\ and\ fal\ apart$$

Then (eq. 34) the crack density should validate these conditions

$$0 < e < \frac{3}{4} g(1-g) \tag{4.35}$$

$$0 < e < \frac{3}{16} g(3-2g)$$

I compare the results of Hsu and Schoenberg with Hudson's (1997) model with a planar distribution of cracks.

As the confining stress is increased, the same procedure applied using four samples at different depth within Pimienta Formation with different confining pressure (Table 4.9).

Depth (m)	Confined pressure (psi)	g	Crack Porosity	Aspect Ratio	Crack density
2104	0	0.334	0.029	0.150	0.046
2108	500	0.335	0.028	0.160	0.042
2114	1000	0.319	0.022	0.150	0.035
2121	1500	0.340	0.013	0.150	0.021

Table 4.9. Summarizes the calculations for crack density from crack porosity and aspect ratio at different confining pressures within Pimienta Formation. All these values are smaller than 0.1, which is the theoretical limit of validity for Hudson's (1981) model with a volumetric distribution of cracks.

I derive the equivalent crack densities using Hudson's (1997) model with planar distributions of cracks. The aspect ratio of the cracks is 0.1 on average within the Pimienta Formation. One important observation is that all the estimated crack density values are smaller than 0.1, the limit of validity for Hudson's model (1981) The highest estimated crack density value is 0.046 at 2014m within the Pimienta formation.

The crack density decreases as we increase the normal stress with aspect ratio average of 0.1 and crack porosity of 0.02 (Table 4.9) as with the equivalent values calculated using Hudson's model (1981). Good agreement is observed between the laboratory measurements on the simulated fractured medium (Hsu and Schoenberg, 1993) and the theoretical predictions of the penny-shaped crack models of Hudson (1981, 1997) (Figure 4.29).

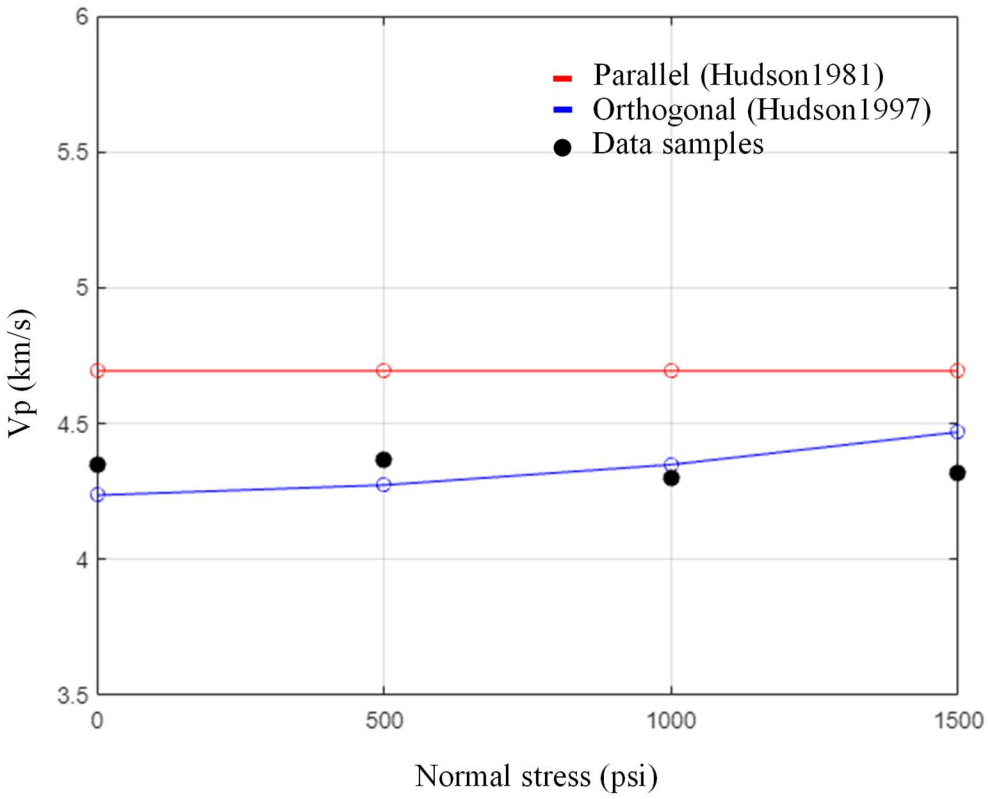

Figure 4.29. Comparison between ultrasonic velocity measurements at different depths within Pimienta Formation on simulated fractured medium (Hsu and Schoenberg, 1993) – red dots (Parallel), and blue dots (orthogonal) using the theoretical predictions of Hudson's models for volumetric distribution of cracks (Hudson, 1981) and planar distribution of cracks (Hudson, 1997). Aspect ratio of the cracks is considered 0.1 according to table 4.9.

Another observation is the similarity of the results from Hudson's (1981, 1997) two different models with volumetric and planar distributions of cracks. This demonstrates that to the first order, it does not matter whether the cracks are distributed volumetrically or confined in planar surfaces.

The first-order equivalence between Hudson's model and the linear-slip model implies that for a certain crack density, the ratio between the normal and tangential weaknesses is fixed for dry cracks. Furthermore, the weaknesses ($\Delta_N \; and \; \Delta_T$) are not independent.

Discussion

When the seismic wavelengths are much larger than the fracture size and spacing, it is convenient to use elastic compliance to formulate the equivalent anisotropic medium problem for seismic modeling of sets of aligned fractures embedded in host medium. The linear slip theory (Schoenberg and Sayers, 1995) provides a direct method to relate the seismic signatures to the properties of fracture systems. Normal (Δ_N) and tangential (Δ_T)) weaknesses, introduced by Hsu and Schoenberg (1993), are two essential parameters of linear slip theory for rotationally invariant fractures. For penny-shaped cracks, by comparing Schoenberg's method and Hudson's method (1981), the normal and tangential weaknesses can be expressed in terms of the crack density and the ratio of P-wave and S-wave velocities of the host rock. A set of vertical, aligned, rotationally invariant fractures leads to a particular HTI medium called TI (LSD).

Only four independent parameters are required to specify a TI (LSD) medium. Rüger's anisotropic parameters for TI (LSD) media ($\delta^{(V)}$, $\varepsilon^{(V)}$, $\gamma^{(V)}$) can be expressed in an approximated linear form in terms of the normal and tangential weaknesses and the ratio of P-wave and S-wave velocities. If the cracks are dry, the $\gamma^{(V)}$ approximately equals density. Interactions between fractures and the shape of cracks do not affect the accuracy of Schoenberg's method, according to Grechka and Kachanov (2006).

The information that can be obtained from seismic data is only the fracture orientation and a rough estimate of crack density. The estimation of shape, size, and distribution of the fracture is beyond the capability of long wavelength seismic data.

The effective medium theory above is based on several assumptions. The theory assumes that the cracks in the host rock are isolated and penny-shaped. Real fractures, however, are not always isolated voids with low aspect ratio in the host rock. So, the validation of the effective medium theory to practical field data seems to be a critical issue for the use of this theory. It is very important to know if the results of this effective medium theory are accurate enough, in spite of the fact that some of the basic theoretical assumptions are violated.

For real field data, most aligned sets of fractures are connected, non-circular, microcorrugated, and have a considerable aspect ratio. If there is more than one fracture set in a host rock, intersecting fractures might occur. However, Grechka and Kachanov (2006) state that, "Micromechanics analysis identified several geometric features of cracks that are insignificant for the effective properties. These features are (1) Fracture intersections; (2) Microcorrugation of fracture faces; and (3) Random irregularities of fracture shapes, provided that the cracks are flat." For a single set of fractures, I am mainly concerned with the effect caused by the interaction and the irregularities of fracture shapes which violate basic assumptions.

A model for interconnected cracks was proposed by Pointer et al. (2000) with equant porosity. An earlier model for aligned cracks was developed by Hudson et al. (1996). A theory for isolated cracks that are partially saturated with a single fluid was put forward by Hudson (1988). Model (a) was also studied by O'Connell & Budiansky (1977) and Mavko & Nur (1975). Partially saturated cracks have been investigated by Walsh (1965) and Mavko & Nur (1979). The results for cracks with equant porosity have also been given by Thomsen (1995) and Chapman (2003).

The occurrence of fluid flow either between cracks within cracks, or from cracks into a porous matrix lowers the mechanical strength of rocks, and has a marked effect on seismic properties, even though the volume occupied by the cracks and pores may be small. Seismic velocities exhibit behavior that is intermediate between that of empty cracks and that of isolated liquid-filled cracks over the range of frequencies in which fluid flow is significant. There is high attenuation and dispersion that becomes anisotropic if the cracks are aligned (Pointer et al. 2000; Chapman 2003).

Figure 4.30 (Grechka and Kachanov, 2006) shows how the interaction of fractures affect the anisotropic parameters with increasing crack density. When the crack density is lower than 0.05, the effects in Figure 4.30 (A) and Figure 4.30(B) for $\varepsilon^{(V)}$,and $\delta^{(V)}$are tolerable. The effects decrease with decreasing crack density, and disappears when crack density becomes 0, which on the face of it seems

reasonable. We are more concerned with the effect on $\gamma^{(V)}$ in figure 4.30(C) which is the direct estimation of crack density. Surprisingly, the interaction almost has no effect on $\gamma^{(V)}$so that violating the assumption of non-interaction is not going to reduce the accuracy of the result calculating by Schoenberg's theory.

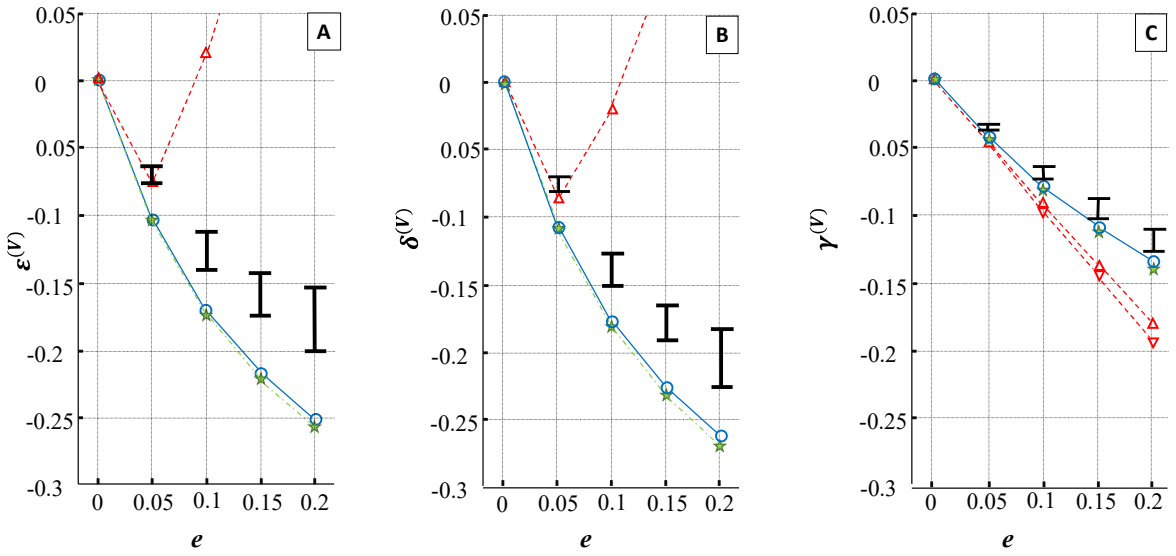

Figure 4.30. Anisotropic parameters (A) $\varepsilon^{(V)}$, (B) $\delta^{(V)}$ and (C) $\gamma^{(V)}$for a single set of vertical penny-shaped dry cracks (Grechka and Kachanov, 2006). Note: The background P-wave velocity is 3.0 km/s and S-wave velocity is 1.0 km/s; and density is 2.2g/cm3. Symbols indicate different theoretical predictions: red ∇-the first-order Hudson's method, red Δ-the second-orderHudson's method, Schoenberg's method, and blue O -the non-interaction approximation (Grechka and Kachanov, 2006) that considers the crack aspect equals 0.05 for all fractures. Bars correspond to the 95% confidence intervals (the mean values of standard deviations) of the numerically computed anisotropic parameters obtained for 100 random realizations of the fracture locations.

Finally using the data from Table 4.9 using the crack density at Anhelido-1 and the values of anisotropy (within the Pimienta Formation) suggest a similar behavior to the model of Grechka and Kachanov (2006) where crack density increases with normal stress and the anisotropy becomes more negative using effective medium theory (Figure 4.31).

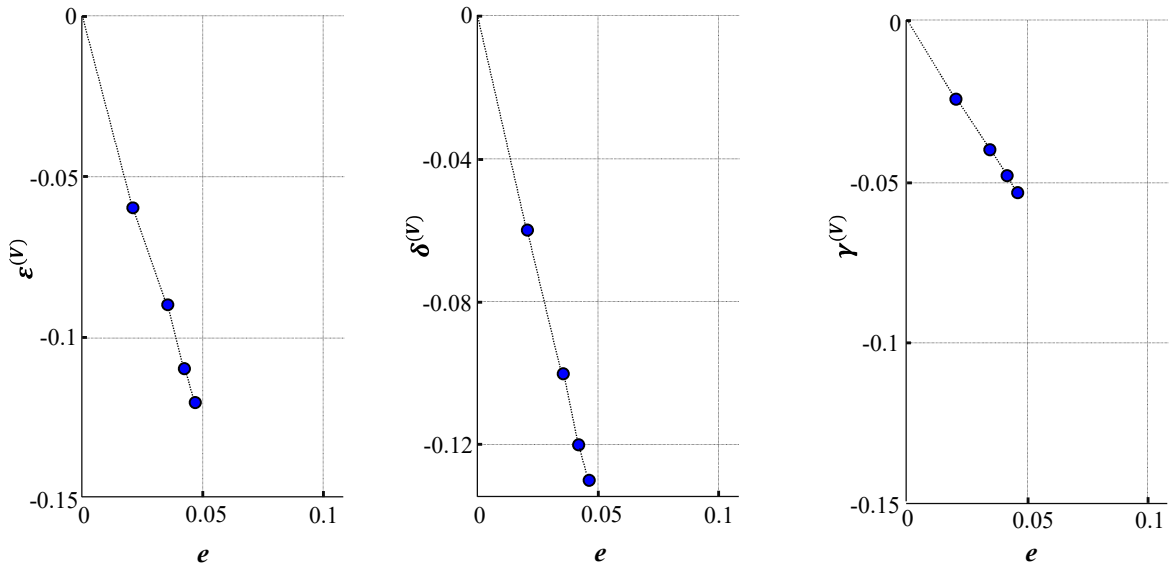

Figure 4.31. Anisotropic parameters (A) $\varepsilon^{(V)}$, (B) $\delta^{(V)}$ and (C) $\gamma^{(V)}$ from four samples at different confining pressures within Pimineta formation at Anehlido-1.

5. Discussion of the link between the B_{ani} parameter and non-fracture rock properties, as discussed in the literature

Chapter 4 (section 4.3.6)

Fracture density is a term used in the field of geophysics to refer to the concentration of fractures in a rock formation. Fractures can affect the physical properties of rocks, such as their permeability and elasticity, and can be detected using geophysical techniques such as AVO (amplitude versus offset) analysis. In AVO azimuthal analysis, the orientation of the fractures is also considered, which can provide additional information about the fractures and the rock formation. This type of analysis can be used to identify the presence of fractures and to map their distribution in the subsurface, which can be useful for a variety of applications such as oil and gas exploration.

The visualization of the B*ani* and φ attributes are combined tool (3D Viewer) for a display of fracture intensity and the primary direction of fracturing. I analysed the AVAz attributes analysis algorithms

on the 3D azimuthal seismic data to estimate the anisotropy magnitude and the isotropy planes. The AVAz anisotropy magnitude within a 3D volume shows areas where the amplitudes hold the greatest variability with azimuth, and the isotropy plane azimuth indicates the direction that the anisotropy is striking. The results give information not only on the relative degree of anisotropy in the Pimienta Formation but the directional variations of that anisotropy as well.

In this case study, Pre-Stack 3D seismic AVAz data is used to detect anisotropy due to the presence of fractures/or stress to directly identify fractured prone sweet spots for appraisal and field development plans. Properly conditioned input seismic and well data is used as input for AVAz modelling and attributes analysis at the well log and seismic scale this is performed as a basic practical requirement of the AVAz methodology to detect the intensity and direction of anisotropy. For AVAz modelling, Horizontal Transverse Isotropy (HTI) model and Linear Slip (LS) models are used for modelling the subsurface fractured media which helped to understand amplitude in azimuth response due to anisotropy caused by fractures or stress.

In a 3D prestack seismic survey the amplitudes are recorded at different azimuths and angles of incidence where AVAz is observed. The probable cause of the AVAz might be the result of an orientated anisotropic medium. In recent studies of HTI medium, it is possible to invert fracture density and orientation from AVAz information.

Approximation of reflection coefficients for HTI media, as presented in Equation 5.1 can permit a generalized linear inversion, like conventional AVO estimation when the incidence angles, azimuths and reflection coefficients are known (A, B*iso*, B*ani* and ϕsym). Hence, B*ani* might remain the only anisotropic parameter to be inverted as crack density.

However, the Bani inverted from real seismic data can never be said to be proportional to crack density due to the band-limited feature of seismic data and phase complexity. Scaling the inversion results to realistic crack density is thus being studied.

The AVAz modelling at the two existing wells provided a way to analyse the AVAz analysis result from B*ani*. The AVAz attributes analysis helped to identify the anomaly of anisotropic gradient

(B*ani*) in order to identify fracture density or stress magnitude in target intervals caused by the existence of intrinsic anisotropy, fine stratigraphic layering, fractures induced or stress- induced anisotropy.

Near offset Rüger equation results showed a promising indication of anisotropic gradient (B*ani*) and azimuth as the orientation of isotropy plane show that the high anisotropy in Serbal-1 and low anisotropy around Anhelido-1 in the vertical part. For example, in Figure 4.32 a forward model is shown of azimuthal synthetic ring gathers using the anisotropic parameters using approximation of Ryan-Grigor at different incidence angles.

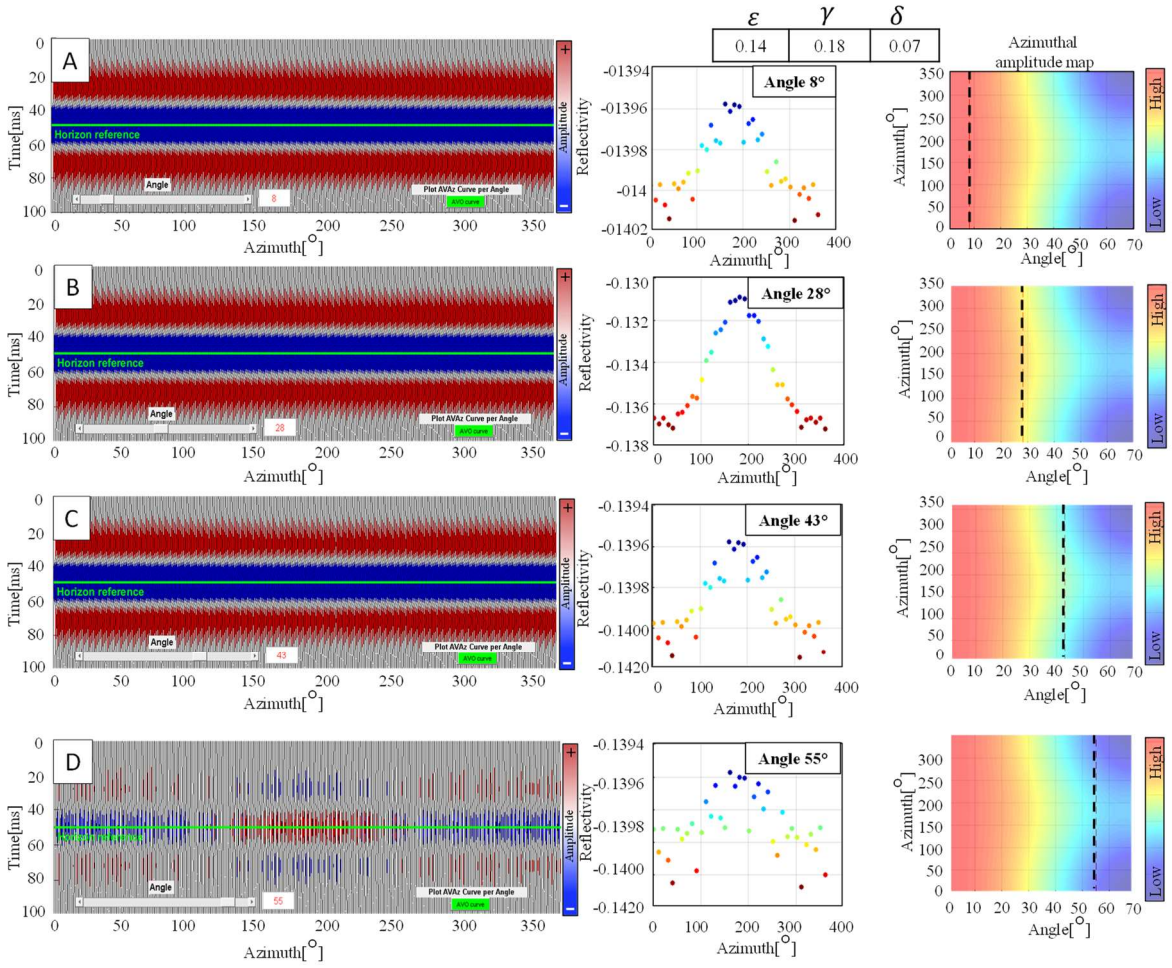

Figure 4.32 Azimuthal ring gather synthetic using Ryan-Grigor anisotropic parameters from well log data at Anhelido-1 within Pimienta Formation.

Finally, I evaluated AVAz analysis based on Rüger equation using 3D Pre-Stack seismic data set from a shale reservoir within Pimienta Formation in Burgos Basin, onshore Mexico. To confirm the maximum horizontal stress, I used the stress map (Figure 4.22). The existence of anisotropy suggests the presence of intrinsic anisotropy, fine stratigraphic layering, or highly possible due to the presence of fractures or localized stress-induced anisotropy but this is qualitative due to a sonic scanner log should be tested to confirm this assumption. This would help to predict the presence of fracture-prone zones and hence achieve optimum hydrocarbon recovery.

The AVAZ technique is sensitive to the contrast in two Thomsen parameters $\gamma(v)$ and $\delta(v)$ (these describe layer-localized shear wave splitting and layer-localized P wave NMO velocity differences parallel and perpendicular to fractures, respectively) across an interface. The AVAZ inversion is based on that class of anisotropy known as horizontal transverse isotropy (HTI). The HTI model assumes the existence of locally mono-oriented sets of vertical fractures. Unfortunately fracture sets in the real world do not always conform to this simple configuration:

The inherent errors are so large and variable that the fracture intensity attributes from AVAZ inversion are not suitable for use as direct quantitative interpretation of fracture intensity. However, the relative differences of fracture intensity attributes from AVAZ inversion qualitatively agree with the actual intensity differences and may be exploited as a qualitative measure of fracture intensity variation applied to a very limited range of incident angles. For noisy data, it is difficult to characterize fracture azimuth, not only by a single inversion but also by a statistical mean of multiple inversion results and an effective de-noising processing strategy is a critical step for fracture azimuth inversion.

For fracture research, using borehole logs or cores are the direct and intuitive methods to study the subsurface fractures. However, there are some limitations and problems from the method itself and the sampling problem is the most important one. For example, commonly mode 1 fractures in the subsurface are nearly vertical, and since most boreholes are vertical the wellbore trajectory commonly runs parallel to the fractures. If the wellbores do not intersect the fracture sets, the information

recovered from the logs might be of limited value. Because of this limitation, a more challenging method, based on seismic exploration, is required and it leads to a valuable and reliable tool for fracture characterization. The orientation and density of fracture sets from the effective medium theory above is based on several assumptions. The theory assumes that the cracks in the host rock are isolated and penny-shaped. Real fractures, however, are not always isolated voids with low aspect ratio in the host rock. So, the validation of the effective medium theory to practical field data seems to be a critical issue for the use of this theory. It is very important to know if the results of this effective medium theory are accurate enough, although some of the basic theoretical assumptions are violated. For real field data, most aligned sets of fractures are connected, and have a considerable aspect ratio. If there is more than one fracture set in a host rock, intersecting fractures might occur. However, Grechka and Kachanov (2006) state that, “Micromechanics analysis identified several geometric features of cracks that are insignificant for the effective properties.

6. DEM approach and detailed comparison with the literature on shale modelling

Chapter 5 (section 5.2.3)

Differential Effective Medium theory allows the calculation of elastic properties (namely bulk and shear moduli) of composite media. This theory "constructs" the model as a background solid medium with added ellipsoidal inclusions. The inclusions are added in an interactive manner to avoid violating the Kuster and Tuksoz (1974) premises.

DEM is widely used for estimating wave-velocity in porous media. For example, Xu and Payne (2009) proposed a rock physics model for calculating wave velocities in carbonates, extending the model proposed by Xu and White (1995). Both models use DEM theory.

The impact of fraction volume kerogen and total organic contents (TOC) on the seismic data response of organic-rich shale has received more attention (Aziz et al., 2018). Several researchers tried to model the impact of these parameters on shale's seismic properties with the rock physics model (Carcione et al., 2011; Vernik & Milovac, 2011; Li et al., 2015; Aziz et al., 2018). Zhu et al. (2012) suggested an improved rock physics model for shale plays. The impact of the fraction volume of kerogen on the anisotropy of shales was carried out by Sayers (2013).

A significant impact of volume fraction of kerogen on seismic properties is due to its low density (Passey et al., 2010). Three essential components: solid organic matter, void space, and rock matrix comprise the organic shale rock, while non-organic rocks are composed of the void space and rock matrix. In Figure 5.18 is shown the diagram of organic shale rock with different maturity levels.

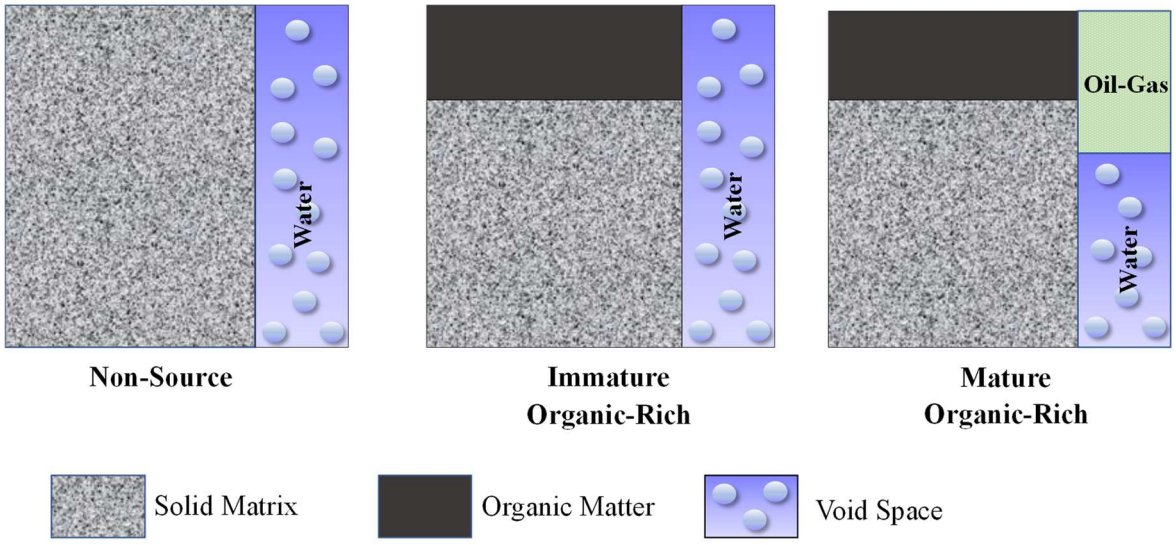

Figure 5.18 Diagram of organic shale rock

The solid organic matter is converted into gas or liquid hydrocarbons by time and temperature (catagenesis). The gas or liquid hydrocarbons migrate into the void space displacing the formation water or increasing the saturation of formation fluids. This displacement of pore fluid by hydrocarbon fluids has a significant effect on density, porosity and resistivity in the Pimienta Formation, which are reflected in the well log response (Passey et al., 2010).

The computation of vitrinite reflectance and level of maturity is addressed in Chapter 3 section 3.4 where information from RockEval was used to estimate the TOC using Passey´s method.

The combination of volume kerogen fraction and the TOC impact on seismic data is still a subject of active research and needs to be investigated further. Here I analyzed the effect of kerogen fraction and TOC on seismic data properties of the shale reservoir within the Pimienta Formation in comparison with the research work reported by Vernik and Liu (1997) in the Bakken Shale with the elastic stiffness coefficients at (70MPa) versus kerogen content computing from bedding-parallel and bedding-normal ultrasonic P-velocity measurements.

The content of organic matter in shales has specific density, resistivity and radioactivity values that influence on well-log and seismic responses (Zhu et al., 2011). Thus, logs and seismic can characterise shale oil/gas reservoirs.

Rock physics provides an essential link between various microscopic and macroscopic physical properties of rocks and fluids (Das et al., 2018). Rock physics modelled is used to quantify the effect of volume of kerogen, porosity, and TOC on seismic properties of organic-rich Pimienta Formation shale. The mixture of kerogen and hydrocarbon-filled pores is assumed to have a non-zero shear modulus (Passey et al., 1990).

The effective medium DEM theory proposed by Kuster and Toksöz (1974) has been used to calculate the elastic moduli of mixture (oil, gas, kerogen, and water) and the organic shales. S_k, S_o, S_g and S_w are the saturation of kerogen, oil, gas, and water respectively. The K_{ogw} represent the bulk modulus of the mixure (oil/gas/water) which is calculated using the equation addressed by Wood (1931). The mineral fraction and gamma ray information within Pimienta Formation are presented in Figure 5.19.

$$K_{ogw} = \left[\frac{S_o}{K_o} + \frac{S_g}{K_g} + \frac{S_w}{K_w}\right]^{-1} \tag{5.3}$$

Where

$K_o - Bulk\ moduli\ of\ oil$

$K_g - Bulk\ moduli\ of\ gas$

$K_w - Bulk\ moduli\ of\ water$

For the estimation of the elastic parameters, Bulk modulus, Shear Modulus and Poisson´s Ratio are given by the following relationship of P-wave, S-wave velocities, and density from log data:

$$\mu = \rho * V_s^2 \tag{5.3}$$

$$K = \rho * \left(V_p^2 - \frac{4}{3}V_s^2\right) \tag{5.4}$$

$$v = \frac{1}{2}\left[\frac{\left(V_p/v_s\right)^2 - 2}{\left(V_p/v_s\right)^2 - 1}\right] \tag{5.5}$$

	Bulk Modulus (GPa)	Shear Modulus (GPa)	Density(g/cc)
Calcite	77	32	2.71
Quartz	37	43	2.65
Clay	21.5	9	2.5
Dolomite	95	45	2.85
Kerogen	6.8	2.02	1.4
Oil	0.6	0	0.7
Gas	0.06	0	0.12
Water	2.25	0	1.04

Table 5.1 Elastic properties of different constituents of shale gas reservoir used in rock physics modelling modified (Mavko et al., 2009) within the Pimienta Formation.

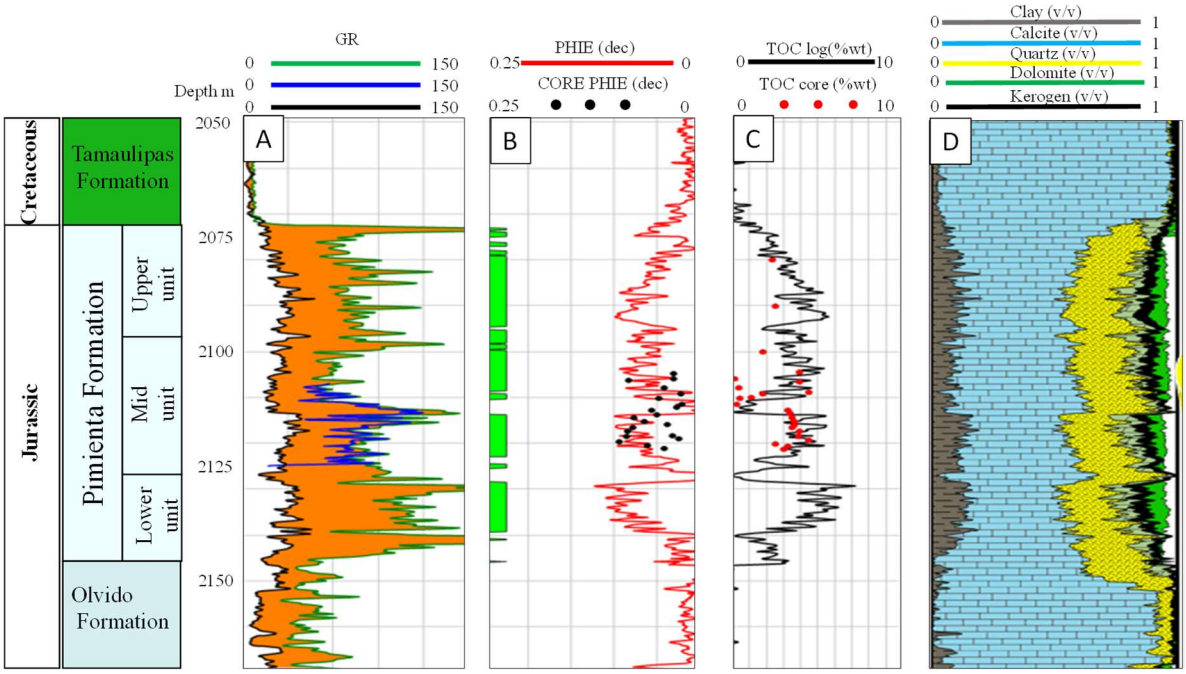

Figure 5.19 Petrophysical evaluation within Pimienta Formation; A) Gamma ray log (black) with no radioactive components Uranium (U), Thorium (Th), and Potassium (K), the Gamma ray log (green) with radioactive components (U), (Th), and (K), the core Gamma ray (blue) with its radioactive components (U), (Th), and (K); B) Effective porosity log(red) and core porosity (black dots); C) TOC log (black) and TOC samples from RockEval (red dots); D)Mineral proportions including kerogen fraction (black).

The TOC effect and the fraction of kerogen on the elastic properties such as Poisson´s Ratio, Bulk Modulus, and Shear modulus of shale Pimienta Formation a 3D scatter data is plotted as a function of TOC and volume fraction of kerogen shown in Figure 5.20 using Plotly python library online and MATLAB. The relationship between Vp and TOC is inverse according to the 3D scatter data. P-wave velocity reduces in organic-rich shale intervals as compared to non-organic shales. The correlation between TOC and quartz fraction contents in the organic shale Pimienta Formation seems inverse, whereas a positive correlation between TOC and the clay content is noted; high volume clay and low velocity represent high values in TOC (Figure 20A). Thus, the dependency of seismic velocities increases with an increase in stiffer quartz fraction and decreases with increase in clay contents as confirmed by Zhu et al. (2012) (Figure 20B).

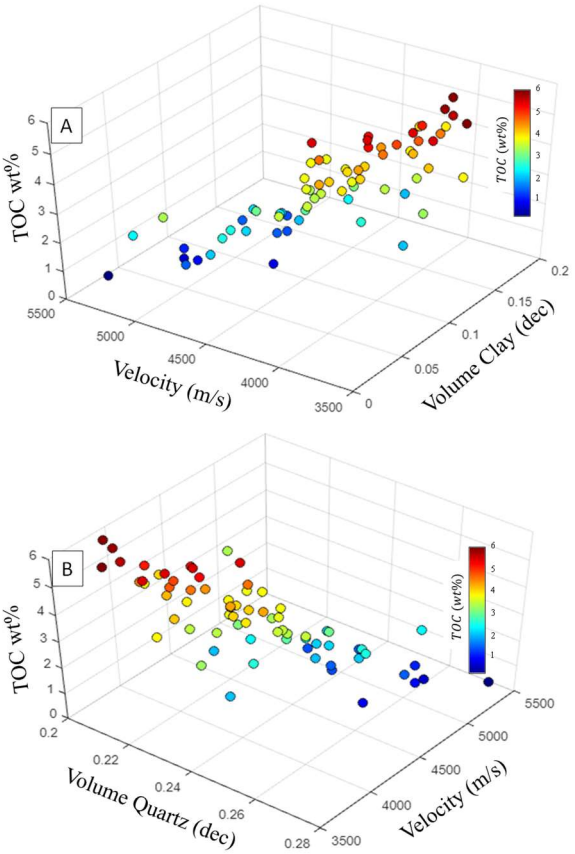

Figure 5.20. Relationship between TOC, P-wave velocity, the volume fraction of quartz and clay in 3D scatter data within Pimienta Formation; A) Velocity decreases with high clay fraction and high TOC; B) Velocity increases with high quartz fraction and low TOC content.

Bulk modulus and shear modulus indicate the elastic behavior of the reservoir rock. The bulk and shear modulus of the Pimienta Formation shales also have an inverse relation with TOC content Low values of bulk modulus represent high TOC and relatively high porosity contents within the Pimienta Formation (Figure 5.21)

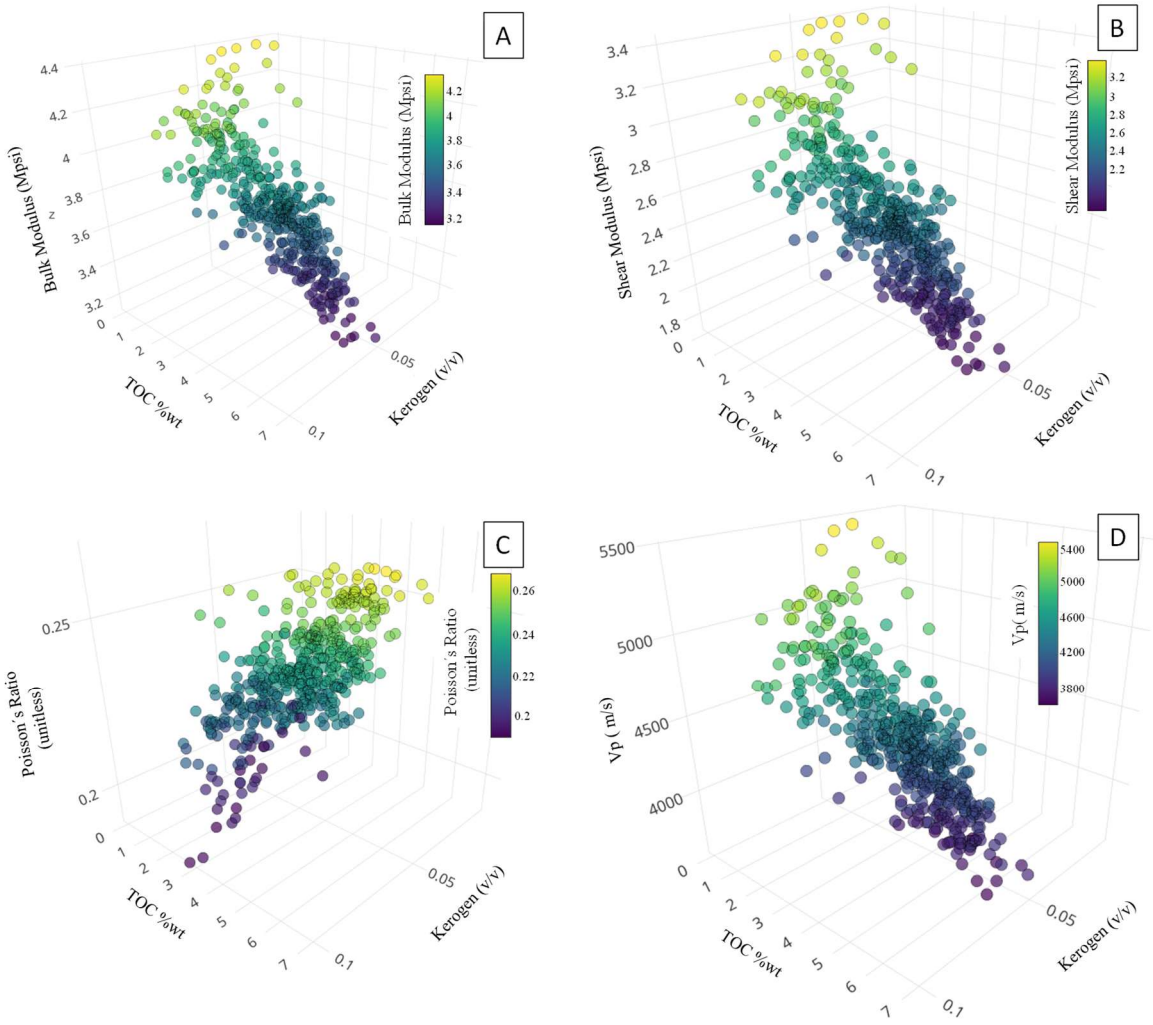

Figure 5.21. Effect of volume fraction of kerogen and TOC on A) Bulk Modulus; B) Shear Modulus of incompressibility; C) Poisson's ratio of Organic-Rich shale within Pimienta Formation encountered at 2074-2145m depth in Anhelido-1.

Recent research on unconventional resources has demonstrated that organic shales have an impact that is found to be strongly anisotropic due to the partial alignment of anisotropic clay minerals and the bedding-parallel lamination of organic material within the shale (Vernik and Nur, 1992; Vernick, 1993, 1994; Vernik and Landis, 1996; Vernik and Liu, 1997; Sondergeld et al., 2000; Sondergeld and Rai, 2011). In their research, these authors investigated the effects of kerogen on seismic anisotropy modelling the Organic-Rich shale as a 1D layered medium consisting of layers of shale and kerogen (Vernik and Nur, 1992; Vernik and Landis, 1996; Vernik and Liu, 1997). In their model, Vernik and Landis (1996) assumed that kerogen could be treated as isotropic, whereas shale is assumed to be

transversely isotropic (VTI) with an axis of rotational symmetry oriented perpendicular to the layers. Figures 5.22 and 5.23 show the relationship between elastic stiffness coefficients (C_{11}, C_{33}, C_{55} *and* C_{66}) and kerogen fraction within the Pimienta Formation described below:

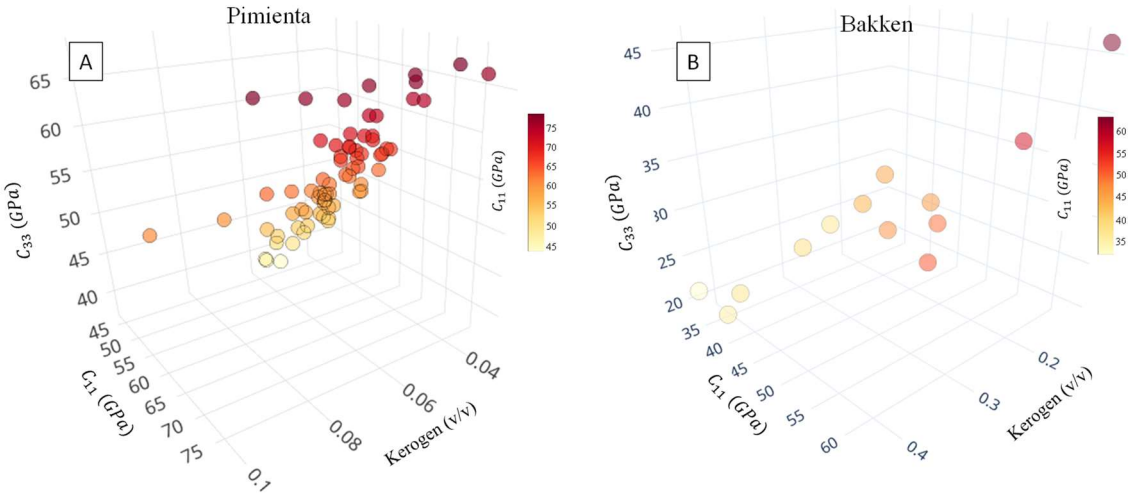

Figure 5.22 Relationship between elastic stiffness coefficients (C_{11} and C_{33}) and kerogen fraction; A) Impact on kerogen fraction as a function of (C_{11} and C_{33}) within the Pimienta Formation B) Impact on kerogen fraction as a function of (C_{11} and C_{33}) on the Bakken Shale suggesting the same behaviour.

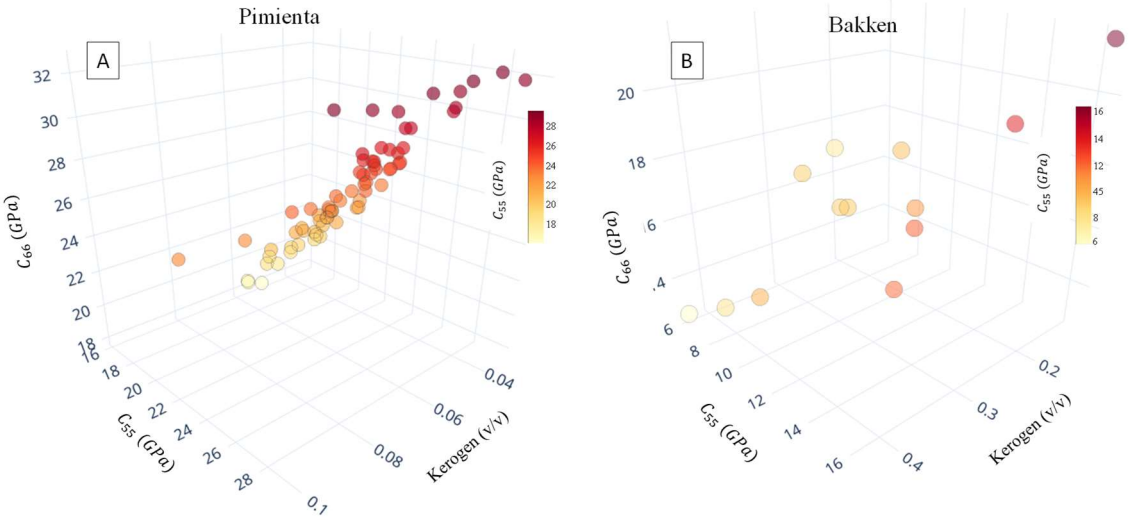

Figure 5.23 Relationship between elastic stiffness coefficients (C_{55} and C_{66}) and kerogen fraction; A) Impact on kerogen fraction as a function of (C_{55} and C_{66}) within the Pimienta Formation B) Impact on kerogen fraction as a function of (C_{55} and C_{66}) on Bakken Shale suggesting the same behaviour.

To establish a relationship of elastic stiffness coefficients within the Pimienta Formation, a comparison with the research work reported by Vernik and Liu (1997) in the Bakken Shale with the elastic stiffness coefficients ($C_{11}, C_{33}, C_{55}, \text{and } C_{66}$) at (70MPa) versus kerogen content computed from bedding-parallel and bedding-normal ultrasonic P-velocity measurements have been made in this thesis project.

The average ranges of elastic coefficients (C_{11}, C_{33}) within the Pimienta Formation are 58 and 50 GPa, respectively, ($C_{55}, \text{and } C_{66}$) are 21 and 24 GPa, according with the Figures 5.22 and 5.23 these coefficients have a substantial impact depending on the kerogen fraction content suggesting that the elastic coefficients in the Pimienta Formation are inverse to the kerogen content. In contrast, the research addressed by Vernik and Liu (1997) in the Bakken Shale suggests that the elastic constants decrease with higher kerogen content according with the average values of C_{11}, C_{33}which round 45 and 28 GPa respectively and 10 and 16GPa for (C_{55}, C_{66}), confirming the same behavior for the Pimienta Formation (Figure 5.24). This is an important finding when it is considered that in the Pimienta Formation the mineralogical content is mostly calcite and quartz (Figure 5.19D), and this would also have an impact on high values of the elastic coefficients.

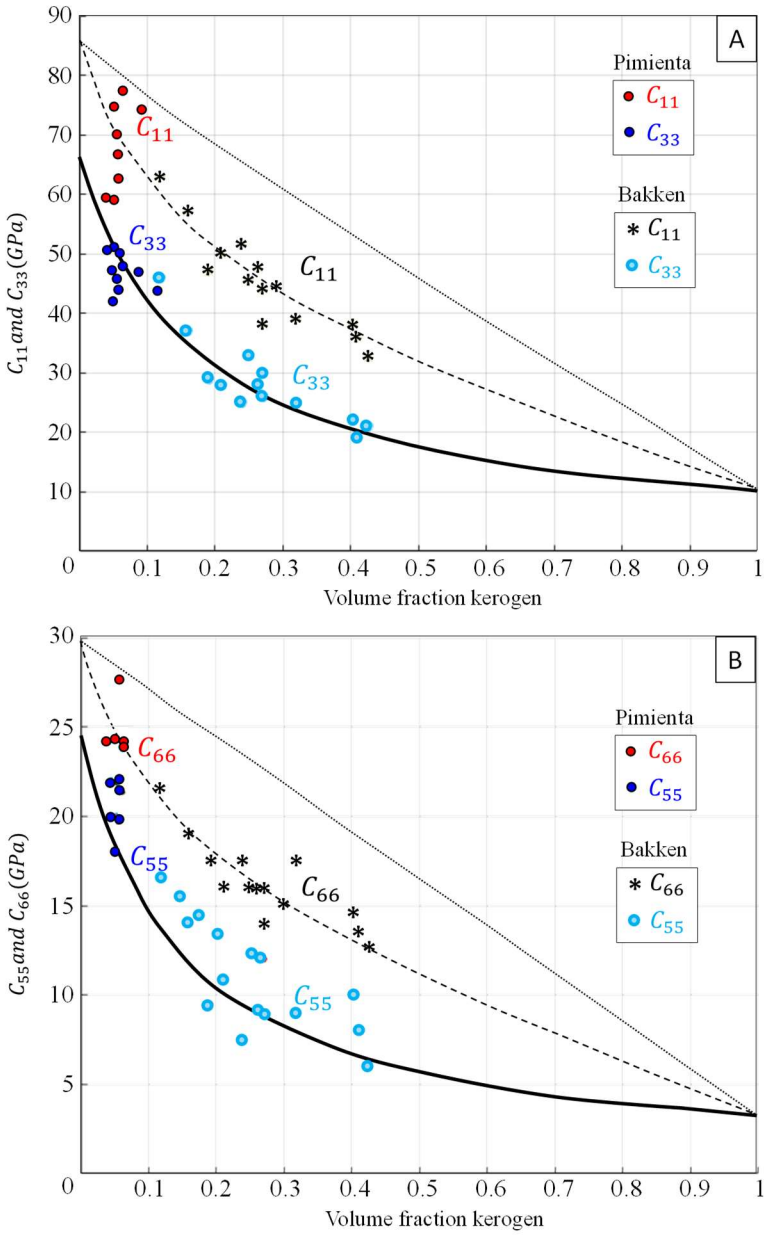

Figure 5.24 A) Elastic stiffness coefficients C_{11} (stars) and C_{33} (blue light points) computed from bedding-parallel and bedding-normal ultrasonic P-velocity measurements reported by Vernik and Liu (1997) in Bakken shale at high confining pressure (70 MPa) versus kerogen content and stiffness coefficients within Pimienta Formation using ultrasonic measurements from log data P-velocity C_{11} (red points) and C_{33} (blue points); B) Elastic stiffness coefficients C_{66} (stars) and C_{55} (blue light points) computed from bedding-parallel and bedding-normal ultrasonic P-velocity measurements reported by Vernik and Liu (1997) in Bakken shale at high confining pressure (70 MPa) versus kerogen content and stiffness coefficients within Pimienta Formation using ultrasonic measurements from log data P-velocity C_{55} (red points) and C_{66} (blue points).

As an lternative approach, a number of studies have employed the DEM scheme (e.g., Hornby et al., 1994; Draege et al., 2006; Vasin et al., 2013). The DEM scheme assumes that hypothetical ellipsoidal inclusions with known aspect ratio distribution are presented and account for the rock's total porosity. The assumption of ellipsoidal penny-shaped pore geometry (see Chapter 4.2.1) makes this model quite controversial due to the elastic inclusion (e.g., Berryman, 1980; Kuster and Toksöz, 1974).This may lead to an inaccurate representation of the rock shale microstructure. However, its microcrack-density parameter does at least offer physics-based approach and any drawbacks can be outweighed by the unrealistic premise about those aspects of pore geometry which represent real limitations. Figure 5.25 shows different model approaches for the estimation of P and S-wave velocities within organic shale rock applied in the Pimienta Formation (Hu et al., 2015; Vernik and Kachanov, 2010).

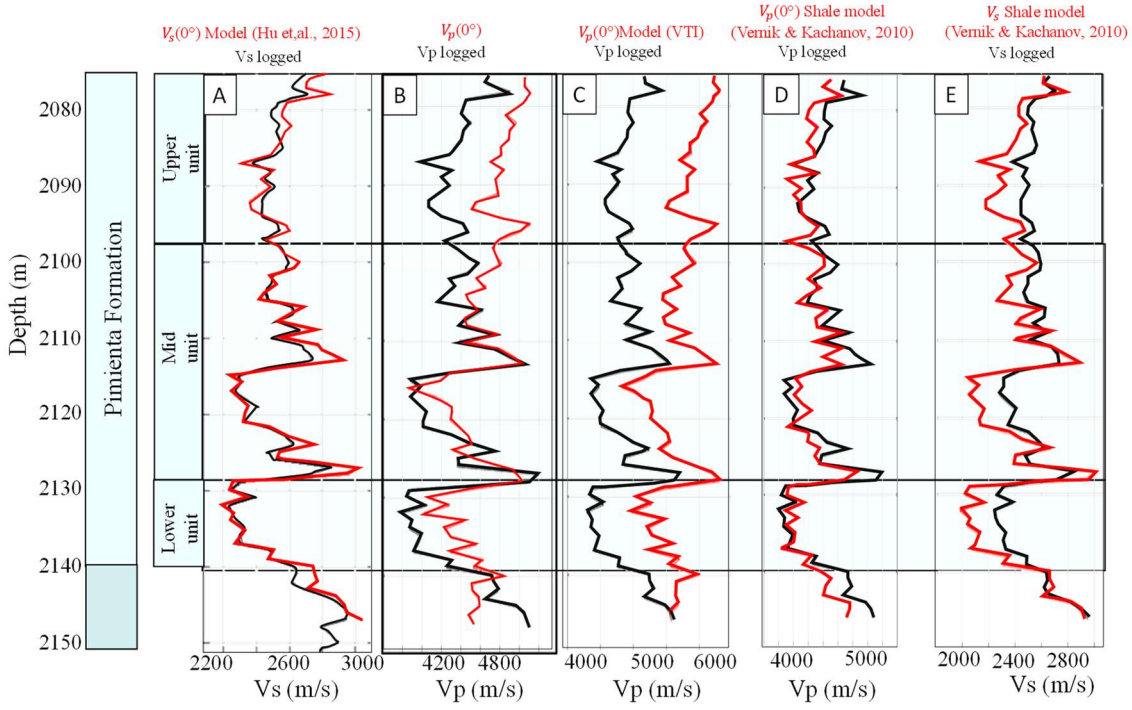

Figure 5.25 Vertical P and S-wave velocity logs (black) within Pimienta Formation at Anhelido-1with different model approach.

Another limitation is that the effect of pore geometry is difficult to estimate from the seismic velocity and porosity of the rock. The modelling of elastic inclusion relates moduli to porosity through an equivalent aspect ratio; in most cases, it fails. In contrast, empirical relations are often hard to extrapolate beyond their range of validity, often leading to incorrect results at high and low porosities.

However, this model was applied to the reservoir zone within the Pimienta Formation since it is the first time it has been carried out on this geological formation in the study area.

The bulk K_{dry} and shear modulus μ_{dry} are estimated using the DEM analytical model (eqs. 5.6-5.14). The parameters of this model are elastic moduli of the solid matrix, porosity (ϕ), and pore aspect ratio (α). Km and μm of the solid matrix were computed using mineral components of the rock XRD data.

$$K_{dry} = K_m \frac{(1-\phi)S_0\left[S_1 + S_2 + S_3 + \left(\frac{(S_1 - S_3)(S_2 - S_3)}{S_3 + \left({}^{K_m}/_{\mu_m}\right)}\right)\right]}{\left[1 + \frac{bK_m}{a\mu_m} - \frac{bK_m}{a\mu_m}(1-\phi)^a\right]^{\frac{S_0}{b}}} \tag{5.6}$$

$$\mu_{dry} = \mu_m \frac{(1-\phi)S_0\left[S_1 + S_2 + S_3 + \left(\frac{(S_1 - S_3)(S_2 - S_3)}{S_3 + \left({}^{K_m}/_{\mu_m}\right)}\right)\right] - a}{\left[1 + \frac{bK_m}{a\mu_m} - \frac{bK_m}{a\mu_m}(1-\phi)^a\right]^{\frac{S_0}{b}-1}} \tag{5.7}$$

$$S_0 = \frac{2 - 3g - 3\theta}{2(2\theta - 3\theta^2 - 2g)} \tag{5.8}$$

$$S_1 = \frac{\theta - g}{2 - 3g - 3\theta} \tag{5.9}$$

$$S_2 = \frac{4}{3} \tag{5.10}$$

$$S_3 = \frac{2(\theta - g)}{3(2\theta - 3\theta^2 - 2g)} \tag{5.11}$$

$$\theta = \begin{cases} \frac{\alpha}{(1-\alpha^2)^{3/2}}\left[cos^{-1}(\alpha) - \alpha\sqrt{1-\alpha^2}\right](\alpha < 1) \\ \frac{\alpha}{(1-\alpha^2)^{3/2}}\left[\alpha\sqrt{\alpha^2-1} - cosh^{-1}(\alpha)\right](\alpha < 1) \end{cases} \tag{5.12}$$

$$g = \frac{\alpha^2}{1-\alpha^2}(3\theta - 2) \tag{5.13}$$

$$P^{*i} - Q^{*i} = a + b\left(\frac{K^*(y)}{\mu^*(y)}\right) \tag{5.14}$$

Bulk and shear modulus are K_{dry} and μ_{dry} , respectively. K_m and $\mu_m$are the mineral matrix moduli, ϕ is the porosity, a is estimated from eq 5.14 where $\frac{K^*}{\mu^*} = \frac{K_m}{\mu_m}$ is placed, b is the first derivative of $P^{*i} - Q^{*i}$, the pore aspect ratio is represented by α (See Appendix A of Li and Zhang (2011) to verify the calculation of $P^{*i} - Q^{*i}$ and its derivatives). The DEM model is favourable for the experimental conditions with high frequency. Assuming dry rock conditions and it is important to calculate then the elastic bulk and shear moduli using Gassman´s model (Gassman. 1951).

Based on the follow assumption, Gassman´s models work as follows:

(1) The rock fabric is homogeneous in terms of macroscopic features.

(2) There is an interconnection between the pores.

(3) A frictionless fluid fills the pores.

(4) The fluids are not drained.

(5) The pore fluids do not interact with the solid particles of the rocks (Adam et al., 2006). The equations of Gassmann's fluid substitution model are given below:

$$K_{sat} = K_{dry} + \frac{\left(1 - \frac{K_{dry}}{K_m}\right)^2}{\frac{\phi}{K_f} + \frac{1-\phi}{K_m} + \frac{K_{dry}}{K_m^2}} \tag{5.15}$$

$$\mu_{sat} = \mu_{dry} \tag{5.16}$$

The fluid-saturated rock moduli are represented by K_{sat} and μ_{sat} and the bulk moduli for fluid is K_f , which is calculated using Eq 16 (Dvorkin et al., 1999):

$$\frac{1}{K_{fluid}} = \frac{S_g}{K_g} + \frac{S_w}{K_w} + \frac{S_{oil}}{K_{oil}} \tag{5.17}$$

$$K_{fluid} = S_g K_g + S_w K_w + S_{oil} K_{oil} \tag{5.18}$$

The saturations of the gas, water and oil are given by S_g, S_w, *and* S_{oil} respectively and K_g, K_w, *and* K_{oil} represent the bulk moduli then can be estimated the fluid saturated rock density using (Mavko et al. 2020):

$$\rho_{sat} = \phi\rho_f + (1-\phi)\rho_{mat} \tag{5.19}$$

$$\rho_f = S_g\rho_g + S_w\rho_w + S_{oil}\rho_{oil} \tag{5.20}$$

$$\rho_m = \sum_{i=1}^{n} f_i\rho_i \tag{5.21}$$

$\rho_{sat} - Density\ of\ saturated\ rock$

$\rho_f - Fluid\ of\ the\ rock$

$\rho_m - mineral\ matrix$

$\rho_g - gas\ density$

$\rho_w - water\ density$

$\rho_{oil} - oil\ density$

Using the previous variables then can be used to estimate the V_P and V_s velocities using the next equations (Mavko et., al. 2020):

$$V_P = \sqrt{\frac{K_{sat} + \frac{4}{3}\mu_{sat}}{\rho_{sat}}} \tag{5.21}$$

$$V_S = \sqrt{\frac{\mu_{sat}}{\rho_{sat}}} \tag{5.21}$$

In this section, I introduce the DEM theory for the analysis of the bulk modulus and porosity relationship in the scatter data analysis within the Pimienta Formation (Li and Zhang, 2010) where the aspect ratio is low according to the theory (Figure 5.26). The comparison to the experiment of Walsh et al., (1965) with spherical pores and the self-consistent theory is shown in Figure 5.27 for bulk and dry shear modulus. For the DEM calculation I have developed a code GUI in MATLAB called DEMmodR1 (Appendix B.1). The result in the modelling suggests very good agreement between well-log data and the prediction log using DEM theory, high correlation is shown between $V_p\ and\ V_S$ (Figure 5.28).

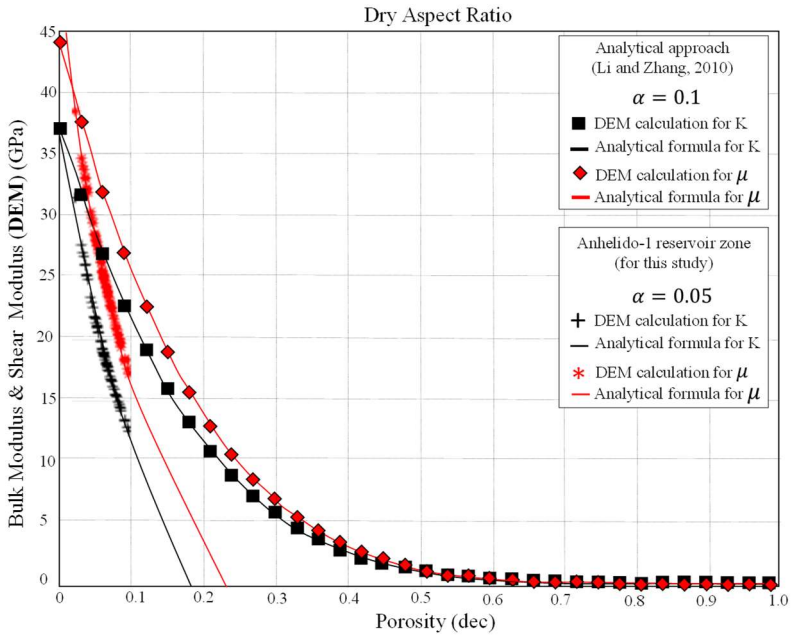

Figure 5.26 The dry-rock bulk and shear moduli for aspect ratio pores (α= 0.1) (Li and Zhang, 2010) and aspect ratio (α= 0.05) within the Pimienta Formation (reservoir zone); Agreement between the complete DEM calculation and the analytical formula is very good.

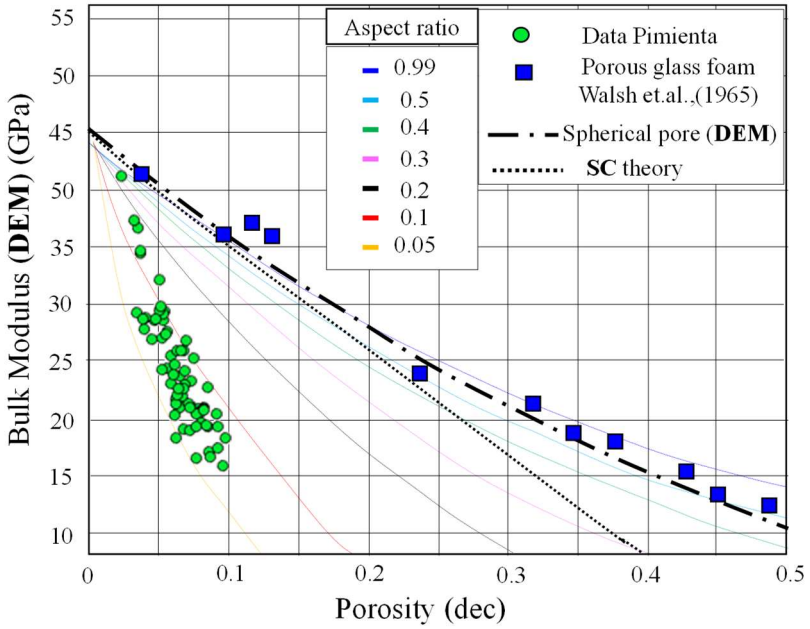

Figure 5.27 Bulk moduli of porous glass foam computed from compressibility's measured by Walsh et al. (1965). Measured values (black rectangles) are compared to theoretical predictions of DEM theory (spherical pores). The dashed line is computed from the approximate formula. The dotted (black) curve is the theoretical prediction of self-consistent theory for spherical pores, and colored curves (are theoretical predictions of DEM theory using different aspect ratios and superposed samples of the Pimienta Formation.

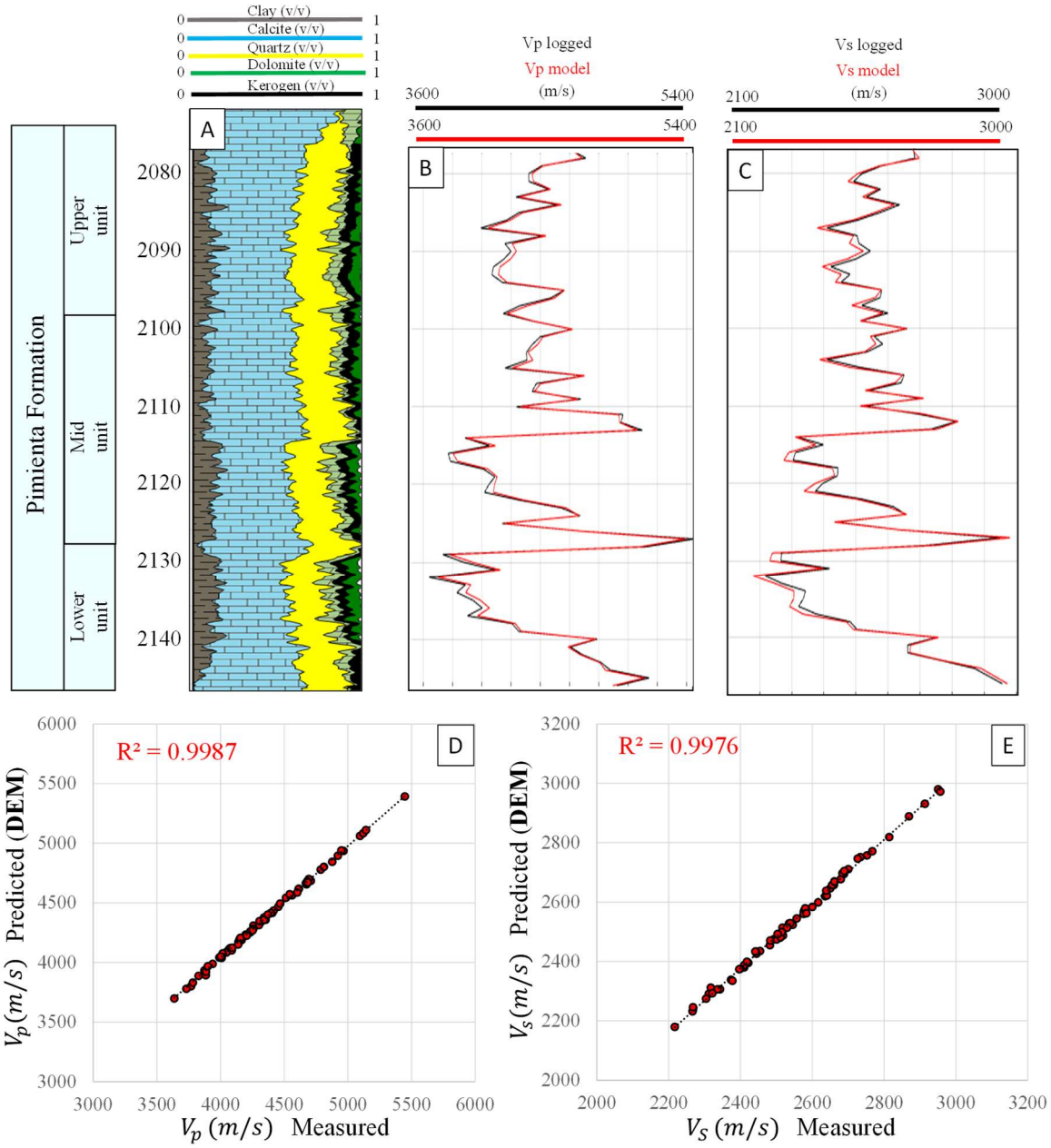

Figure 5.28. A) Minerals volume fraction; B) Vertical P -wave velocity (black) from log data measured; and Vp predicted from modelling (red) DEM analysis and Gassman´s theory; B) Vertical S -wave velocity (black) from log data measured; and Vs predicted from modelling (red); D) Correlation R^2=0.9987 between V_p logged and V_p predicted from modelling; E) Correlation R^2=0.9976 between V_s logged and V_s predicted from modelling.

Chapter 5 (section 5.2.4)

Description of different brittleness index estimated in Anhelido-1 and Serbal-1 within Pimienta Formation. (Figure5.37)

Guo et al. (2012) presented an analysis of brittleness, fractures, and microstructure of the Barnett Shale in order to achieve a better understanding of the correlation between mechanical properties, mineralogy, and pore geometry using the self-consistent approximation (SCA) model. They found that the brittleness defined by Young's modulus is not consistent with the definition in terms of $(\lambda + 2\mu)/\lambda$ and Poisson's ratio. They also found that Young's modulus is a good indicator for the variation of crack density whereas the pore-type inversion showed that the variation of pore types coincides with inverted crack density.

Sharma et.al., (2012) proposed a new attribute $(E\rho)$ in the form of a product of Young's modulus and density, and suggested it represented a good lithology indicator. They described this new attribute as a scaled version of the $(\mu\rho)$ attribute and illustrated that it intensifies the sensitivity to variation in lithology. This attribute can be derived seismically, and Sharma et al. (2012) have shown that it is a viable parameterization of the brittleness of a formation. Chen et.al., (2014) proposed a rock physics effective model, from four aspects of quartz content, organic matter, porosity, and fluid types. Their new brittleness factor was compared with the standard index of rock brittleness –Young's modulus. Tests on real datasets showed that the new brittleness factor is more sensitive than Young's modulus when used in predicting gas-bearing brittle shale reservoirs. Goodway et.al., (2010) introduced a parameter that is a combination of Lame coefficients and shear modulus to characterize brittleness.

7. Effective field method (EFM) within Pimienta Formation

Chapter 5 (section 5.2.5)

For over two centuries, engineers, physicists, and mathematicians have studied heterogeneous random media in detail. Examples of random microstructures include composites and nanomaterials, geological features, metals, and polymers at a particular scale. Such scientists as Poisson, Mossotti, Clausius, Lorenz, Lorentz, Maxwell, and others have focused on the challenge of estimating their effective physical qualities (the homogenization problem) (Kanaun and Levin, 2013). They provided the first approximations in their ground-breaking publications, which implicitly employed variants of the self-consistent effective field approach. However, the precise formulation of the method only emerged in the first part of the 20th century.

The estimation of elastic wave propagation velocities in cracked rocks is addressed by the effective field method (EFM), which is a component of the self-consistent scheme. The data from DSI cross-dipole measurements from well-log were used to model the crack density for sub-vertical fractures and their orientation angles.

Effective medium approaches are a different class of self-consistent schemes (EMM). These techniques treat each inclusion as an isolated entity within the medium with the composite's functional characteristics. As a result, the interactions between inclusions are considered in different ways in the EFM and EMM. The predictions made by the approaches differ as a result. In Kanaun and Levin (2008), the EFM and EMM are compared. One advantage of the EFM over the EMM is that the EFM produces explicit equations for the effective characteristics for composites with ellipsoidal inclusions,

whereas the EMM results in implicit equations that are frequently only amenable to numerical solutions.

In this work we aim to characterize unusual spatial distributions of inclusions affect their effective qualities using the effective field method, an aim which is not achievable using any other approach.

Natural rocks with voids, cracks, and inclusions can be viewed as an elastic homogenous medium with a random field of different types of inhomogeneities. Such materials have random functions for physical fields. When applied to rock materials, the main challenge of micromechanics is to assess the statistical moments of these fields due to various forms of external forcing. The homogenization challenge is the finding of the mean values of various fields (such as the stress and strain fields) and the correlations between these mean values. After this issue is resolved and these relationships are built, it will be possible to substitute an inhomogeneous rock material with a homogeneous one that has the same effective (overall) qualities as the original medium. The interactions between both the original media and this homogeneous medium at the macroscopic level.

The homogenization problem becomes that of an isolated inclusion contained within a homogeneous matrix when the inhomogeneities volume concentration (or density) is low (no interaction). This issue can be precisely resolved for elliptic fractures and homogeneous ellipsoidal inclusions, allowing for the construction of the precise homogenization problem solution in these circumstances (Nur, 1971; Anderson et al.,1974; Hudson, 1981, 1990; Peacock & Hudson, 1990; Sayers & Kachanov, 1991; Kachanov, 1992, 1993; Cheng,1993; Thomsen, 1995; Xu, 1998; Schubnel & Gueguen,2003)

The homogenization problem becomes more challenging since it requires solving the so-called many-particle problem at high crack densities when interactions between inclusions are crucial.

There is only an approximation to the exact solution of the many-particle issue for a medium with a random set of inhomogeneities. We are able to provide approximations of solutions to numerous particle problems of various types using a class of techniques known as self-consistent approaches.

These techniques reduce a many-particle problem to a problem for a single particle by employing physically plausible theories. If the latter can be resolved, the homogenization problem's solution can likewise be built. Self-consistent schemes, which are frequently employed in geomechanics (O'Connell & Budiansky, 1974; Budiansky & O'Connell, 1976; Korringa & Thompson, 1977; Berryman, 1980, 1992), are variations of the so-called effective medium method (EMM).

The many programs created by Henyey and Pomphrey (1982), Norris (1985), Sheng (1991), and Hornby et al (1994), LaRevalec and Gueguen (1996), Jacobsen et al. (2000), and Saenger and Shapiro (2002) are also essentially a version of EMM (this version is also called the differential effective medium method (DEM) addressed in this chapter section 5.2.5.

Another self-consistent approach in theoretical physics is distinct from EMM (or DEM). Each inclusion in an inhomogeneous media is viewed as an isolated inclusion in the homogeneous background medium according to this method (matrix). The external field acting on the medium is not the same as the field acting on this inclusion (effective field). The perturbations brought on by all nearby inclusions are added to this external field. A self-consistent strategy like this is referred to as an effective field approach (EFM). The effective field is taken to be constant and the same for all inclusions in the most basic version of the EFM (quasi-crystalline approximation).

This approach has a lengthy history and has mostly been applied to the theory of phase transitions and nuclear physics to describe various kinds of interactions involving several particles. This technique has been applied by Kanaun [1982, 1983], Kanaun and Levin (1993, 1994), and Markov (2001) to the mechanics of composite materials. Unfortunately, this approach is rarely used when dealing with geomechanics-related issues.

Over the EMM, the EFM has some advantages. Instead of the system of nonlinear algebraic or differential equations for these parameters that were produced under multiple iterations of the EMM, the EFM frequently offers unambiguous expressions for the effective parameters of inhomogeneous materials. The later equations are typically only amenable to numerical solutions.

In all inclusion density ranges, the formulas for the effective parameters of inhomogeneous materials produced with the EFM are physically accurate. The EFM offers several advantages over the EMM for inclusion and matrix qualities that are arbitrary constants.

In many circumstances, the effective parameters of inhomogeneous materials are expressed explicitly by the EFM rather than through a set of nonlinear algebraic or differential equations, as they would be by different EMM iterations. In most cases, the latter equations can only be quantitatively solved. The formulas for the effective parameters of inhomogeneous materials generated with the EFM are physically accurate over the entire ranges of inclusion density and for any arbitrary constant features of the inclusions and the matrix.

When the component attributes are highly contrasted, the EFM's predictions are more in line with the experimental data than the EMM's. The EFM provides for the description of the effect of the peculiarities of the spatial distribution of the inclusions on the effective qualities, which is not achievable in any version of the EMM (Kanaun & Levin, 1994). With comprehensive statistical data regarding the microstructure of the composite material, it is possible to incrementally enhance the predictions of the EFM (Kanaun, 2003).

The EFM will be used in this study to determine the effective elastic moduli of rock materials having dry and fluid-filled fractures found in the Pimienta Formation. The method used in this study is different from the DEM method discussed in section 5.4.4. Every crack-like inclusion in the rock material is thought to have a unique local external field operating on it. The orientation of the inclusion under examination must be considered, though. A better description of the interactions between fissures in rock materials is now possible because to this modification of the EFM, which Kanaun (1993) first suggested.

The EFM reduces the many-particle issue's solution to that of a single-particle problem. In the latter, an isolated inclusion in an infinitely homogenous media loaded by a constant external field faces an elastic issue. Physically, the ratio of the characteristic elastic moduli of the confinement and the medium, and geometrically, the ratio of the characteristic diameters of the confinement, are the two minor parameters in this problem for crack-like confinement. For applications, only the asymptotes of the solution for these parameters are necessary.

Penny-shaped cracks

Let us consider penny shaped cracks with orientation m coaxial to the inclusion for this case, tensor $Q_{ijkl}(m)$ in the T basis is defined by.

$$Q_{ijkl}(m) = q_1 T^2_{ijkl} + q_2 \left[T^1_{ijkl}(m) - \frac{1}{2} T^2_{ijkl}(m) + q_3\left(T^3_{ijkl} + T^4_{ijkl}\right) + q_5 T^5_{ijkl}(m) + q_6 T^6_{ijkl}(m)\right], \tag{4.34}$$

$$q_1 = -\mu_0[4\kappa_0 - 1 - 2(3\kappa_0 - 1)f_0 - 2f_1],$$

$$q_2 = -2\mu_0[1(-2 - \kappa_0)f_0 - f_1],$$

$$q_3 = -2\mu_0[(2\kappa_0 - 1)f_0 + 2f_1],$$

$$q_5 = -4\mu_0(f_0 + 4f_1),$$

$$q_6 = -8\mu_0(\kappa_0 f_0 - f_1),$$

Where

$$f_0 = \frac{1 - g}{2(1 - \Upsilon^2)}, f_1 = \frac{\kappa_0}{4(1 - \Upsilon^2)^2}[(2 - \Upsilon^2)g - 3\Upsilon^2], \tag{4.34}$$

$$g = \frac{\Upsilon^2}{\sqrt{\Upsilon^2 - 1}} arctan\sqrt{\Upsilon^2 - 1}, \Upsilon = \frac{\alpha}{\alpha_3} > 1$$

And κ_0 is determinated in equation (Appendix B.4)

Considering the case when all the cracks have the same orientation m. In this case, the average over orientations in the right-hand side of equation (54) for S^* is absent, and the tensor of elastic compliances can be written in the form.

$$S^*_{ijkl} = S^0_{ijkl} + \frac{4\bar{M}_1}{4 + \bar{M}_{1q5}} T^5_{ijkl}(m) + \frac{\bar{M}_2}{4 + \bar{M}_{2q6}} T^6_{ijkl}(m), \quad (4.34)$$

Where

$$\bar{M}_1 = \langle \frac{\tau}{2\mu_0} \left[\frac{a\mu}{2h\mu_0} + \frac{(2 - v_0)}{(1 - v_0)} \right]^2 \rangle \quad (4.34)$$

$$\bar{M}_2 = \langle \frac{\tau}{2\mu_0} \left[\frac{a(\lambda + 2\mu)}{2h\mu_0} + \frac{\pi}{4(1 - v_0)} \right]^2 \rangle$$

$$\tau = \frac{4}{3} \pi a^3 n_0$$

Figure 5.40 shows the result for the $V_{sH}$and V_{sv} measured and calculated using effective field method (EFM) in the Upper Cretaceous Tamaulipas formation and Pimienta formation. The crack density has been estimated in both formations to establish V_{fast} and V_{slow} showing differences in velocity Figure 5.41 suggesting that the anisotropy is present in both formations, the higher anisotropy can be observed between (1920-1960m) within Tamaulipas Formation. The angle between the hole axis and the normal to the crack system have been determined as well showing a degree angle according to the crack density estimation of Figure 5.42.

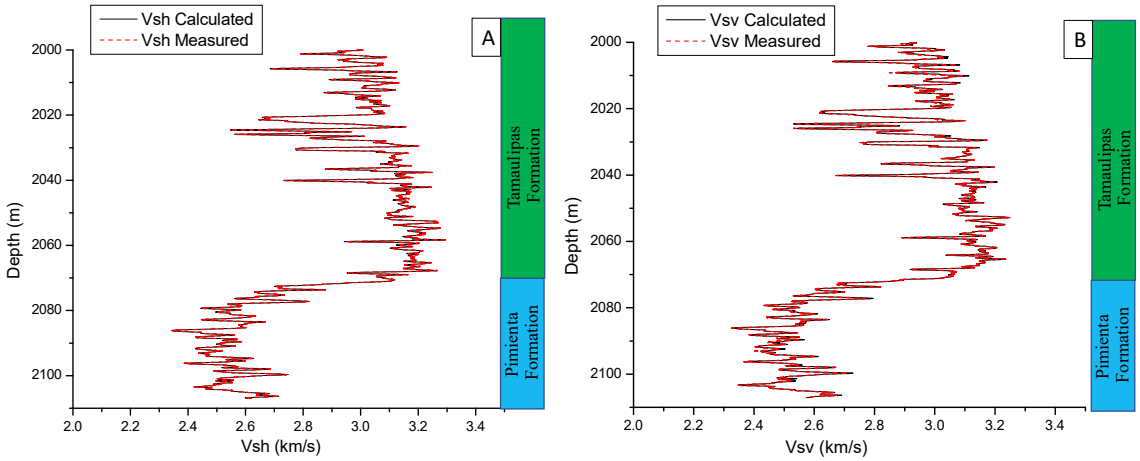

Figure 5.40. $V_{sH}$and V_{sv} measured and estimated using effective field method (EFM) within Tamaulipas and Pimienta Formation.

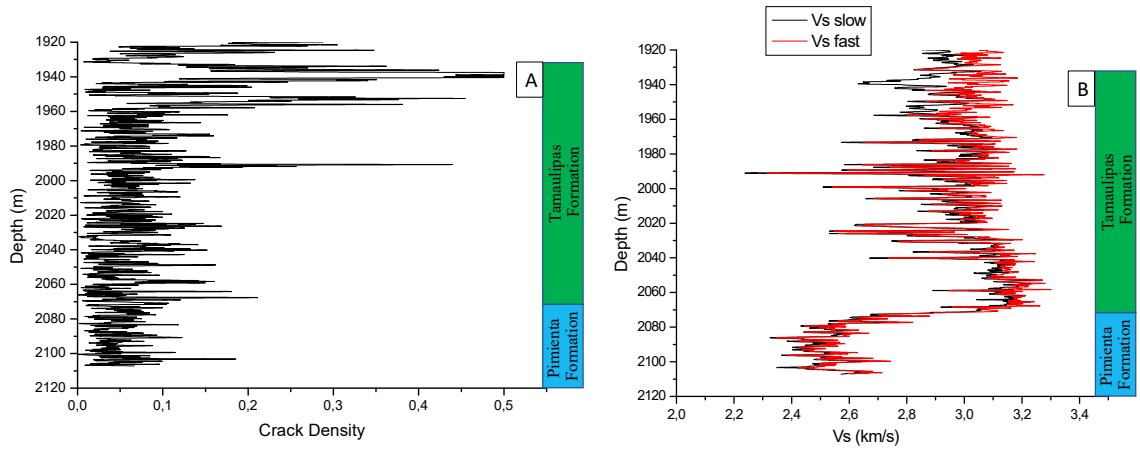

Figure 5.41. A) Crack density log estimation; B) $V_{fast}$and V_{slow} within Tamaulipas and Pimienta Formation

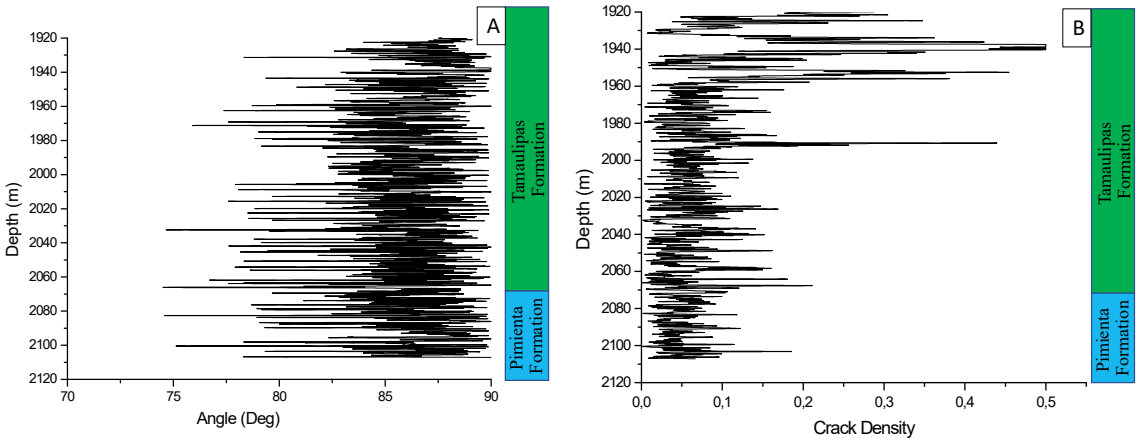

Figure 5.42 Angle between the borehole axis and the normal to the crack system.

To see the correlation of the $V_{sv} and\ V_{sH}$ using the effective field method the scatter plot (Figure 5.43) shows a very high correlation according with the result in R^2. Both methods DEM and EFM addressed in this thesis shows very high correlations.

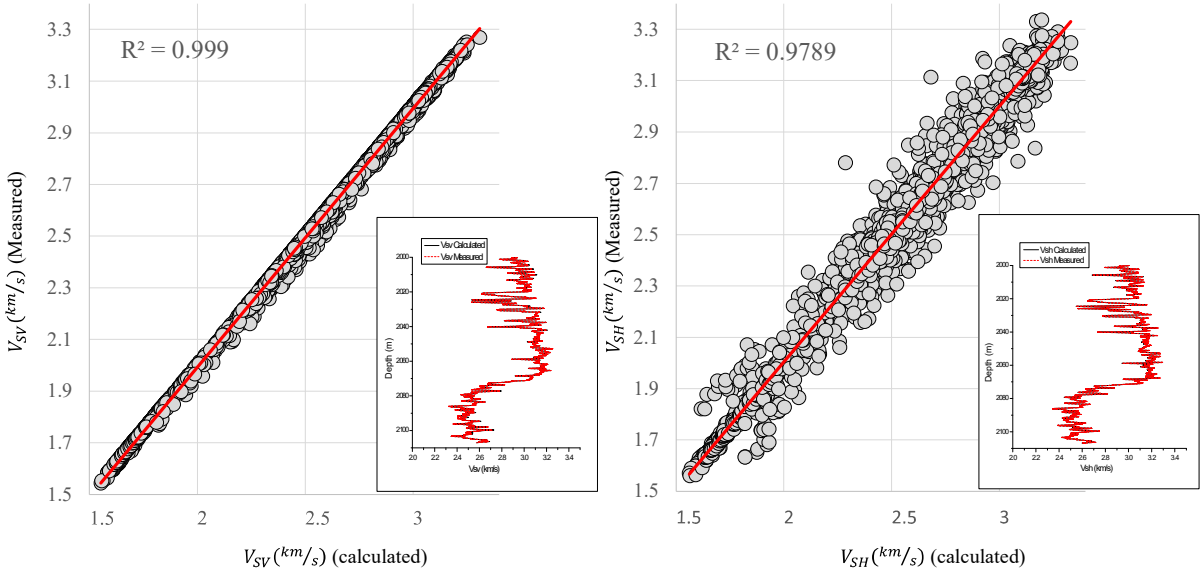

Figure 5.43. Scatter plot $V_{sv} and\ V_{sH}$ using effective field method EFM and the correlation between measured and calculated velocities.

8. Description of how attributes were extracted from the data

Chapter 5 (section 5.2.6)

For Azimuthal AVO B*ani* Map extraction

Analysis of the azimuthal anisotropy plays an important role in shale reservoirs characterization as it can be used to map pre-existing fractures or help in optimal horizontal wells placement. Here I focus on the Pimienta Formation.

The fracture density maps attributes were extracted from the B_{ani}volume of the azimuthal AVO with an investigation window of approximately 80 m from the top of the Pimienta Formation and the top of the Olvido Formation. The extraction of the value of the anisotropic gradient could then be associated with the intensity of fractures.

In order to map the orientation of fractures and the principal stresses, the seismic amplitude of the Pimienta Formation was observed in different azimuths to detect any anisotropy. The data is best sorted in the COCA gather common offset by common azimuth since this allows the extraction of the horizontal transverse isotropy (HTI).

For this case the horizontal transverse isotropy (HTI) model was used. This measures the reflectivity within a fractured layer (Pimienta Formation) underlain by an isotropic layer. For fractured reservoirs it requires an overlapping seal, which in this case is represented by the Lower Cretaceous layer, and this has very high impedance response (Figure 2.5).

The overlapping seal should ideally be relatively homogenous so that the anisotropy results in HTI media can be explained by Thomsen parameters ($\varepsilon^{(v)}, \gamma^{(v)}, \delta^{(v)}$). ′v′ represents the vertical velocities and are used as reference. The Thomsen parameters measure the degree of anisotropy and are dimensionless and isotropic when all these parameters are zero.

The top reservoir (Pimienta) represents the source rock and has regional areal extent. The B_{ani} response changes quickly in the lateral direction (Figure 5.45). It provides the geological basis for fracture reservoir prediction. The target layer average thickness is about 80m. The reservoir thickness about 80 m is higher than λ/4 (about 46m in this area and tunning thickness about 36m) (Figure 3.7).

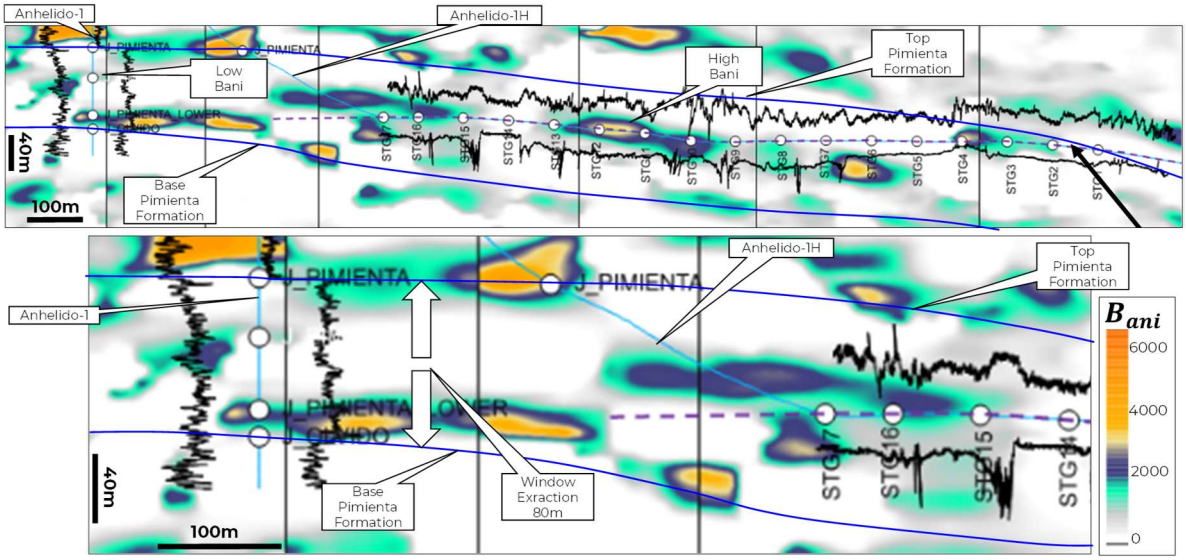

Figure 5.45. Lateral view of horizontal wellbore Anhelido-1H and the extraction window of B_{ani}

The seismic information is conditioned, and azimuthal seismic attributes are generated that contain the magnitude and orientation. This process is carried out for each CDP where, according to Rüger, the following attributes are estimated: There are four main terms of the (eq. 5.41); ($A_{iso}, B_{iso}, B_{ani}$ and ϕ) (Figure 5.46)

A_{iso} Intercept

Isotropic gradient B_{iso}

anisotropic gradient B_{ani}

isotropy plan direction ϕ

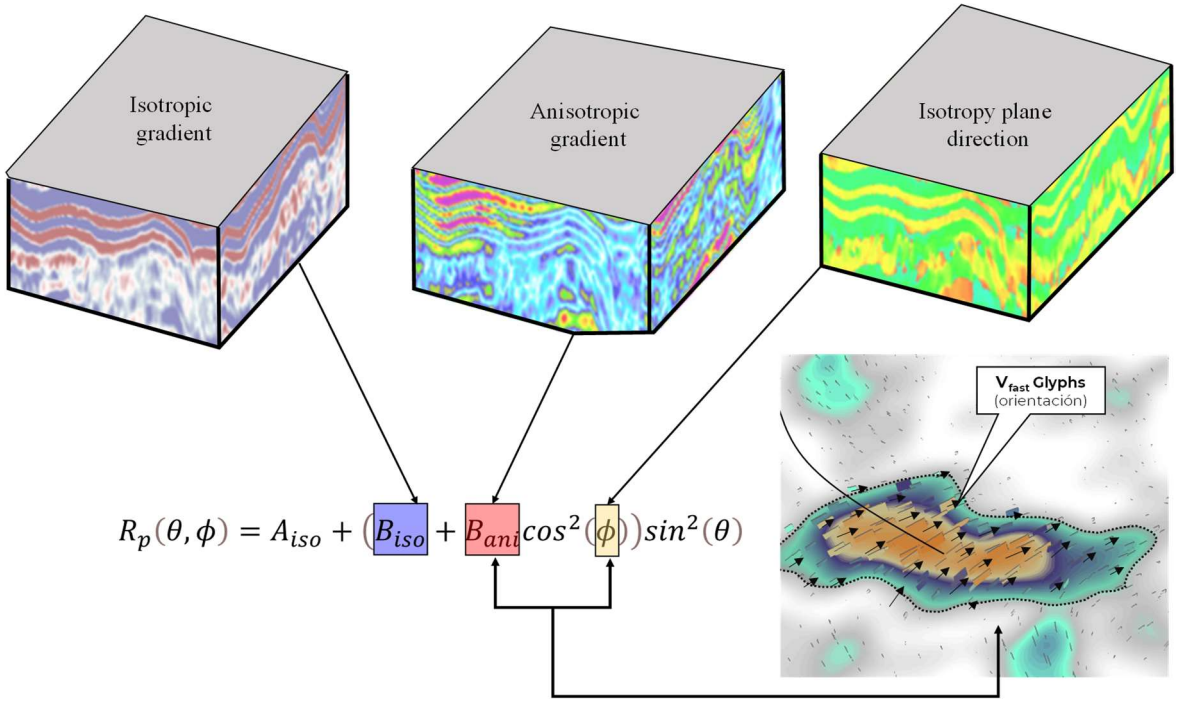

Figure 5.46. Terms obtained in Rüger equation where B_{ani} is related the fracture density and isotropy plane direction ϕ the azimuth volume; when these volumes are combined it can estimate the glyphs (vector distribution of possible fracture orientation) which is related to the direction of fast velocity or stress.

According with the (eq. 5.1) Rüger style can be written in linearized manner (Xu and Li, 2002), such that:

$$R_p(\theta,\phi) = A_{iso} + \left(B_{iso} + B_{ani}cos^2(\phi)\right)sin^2(\theta) \tag{5.41}$$

$$B_{ani} = \frac{1}{2}\Delta\delta^{(v)} + 8\left(\frac{\bar{\beta}}{\bar{\alpha}}\right)^2 \Delta\gamma \tag{5.42}$$

The azimuthal angle ($\boldsymbol{\phi}$) is the difference between the source-receiver azimuth and one of the model parameters that is to be inverted for $\boldsymbol{\phi s}$. The other model parameters are A_{iso}, B_{iso}, and B_{ani}. The objective function is the sum of the square of the differences between the measured data and theoretical data, $\boldsymbol{R}$p($\boldsymbol{\theta}$, $\boldsymbol{\phi}$), modeled using Ruger (1998) for the AVAz done in this thesis.

For penny-shaped cracks model (Hudson, 1981), B_{ani} can be proportional to the crack density, as shown by Figure 5.47. For simplicity, this rock physics model is often used by industry; I do so here.

The ambiguity in inverted symmetry axis can be resolved by some priori information, such a rough estimate of B_{ani} or knowledge about symmetry axis directions (Rüger, 1996).

Higher anisotropy is shown along the horizontal wellbore side around Anhelido-1H however in Anhelido-1 shows lower values (Figure 5.45). The AVAz volume using near-offset Rüger equation show Bani as anisotropic gradient and the orientation of the isotropy plane.

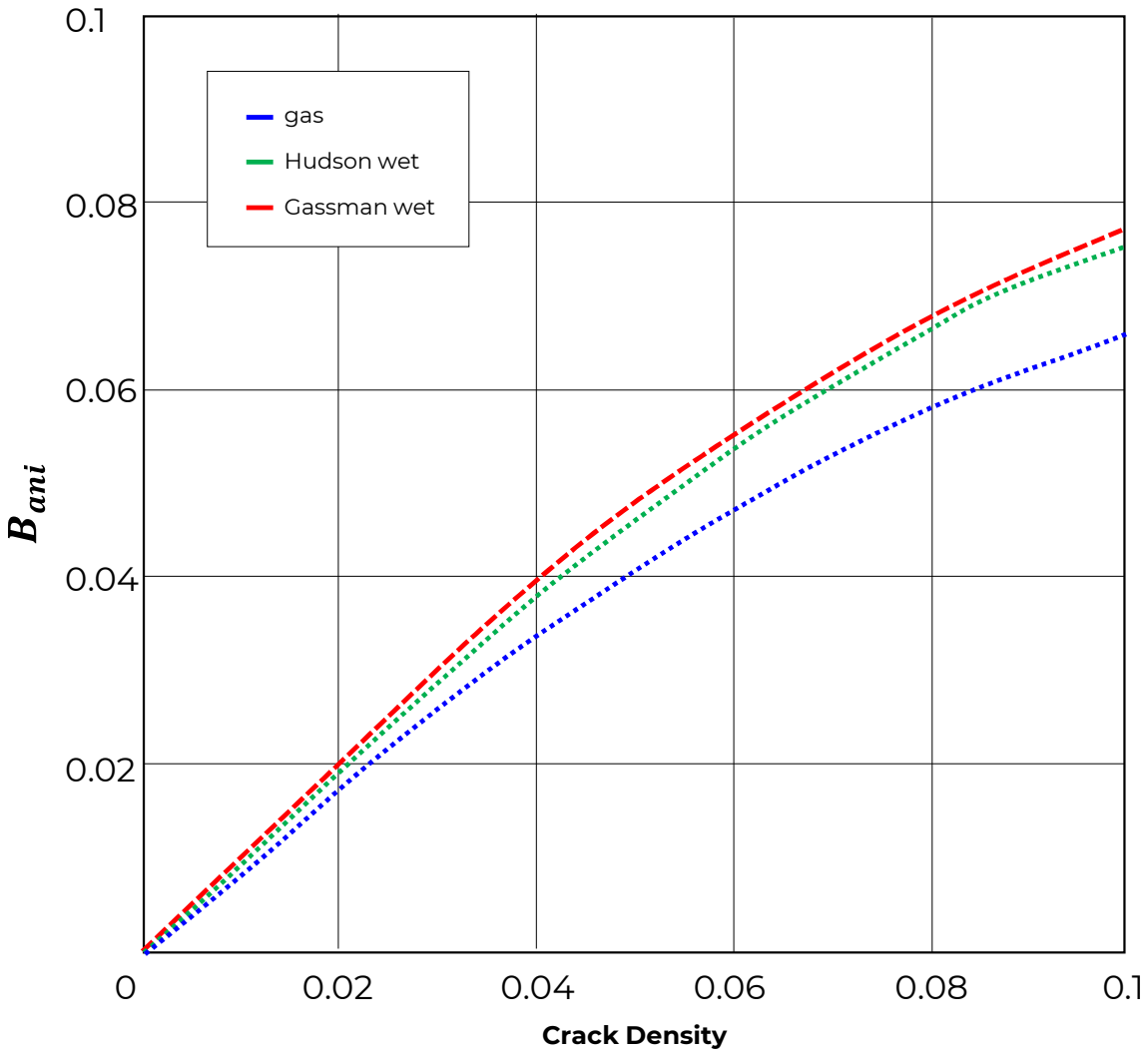

Figure 5.47 Relationship between Crack density and B_{ani}.

To test the algorithm, a synthetic gather was created using the velocities and densities from well logs the synthetic gather is displayed on Figure 5.48. After several iterations of the optimization routine, the isotropy plane was obtained to be 45°. The values for anisotropic gradient and isotropy plane obtained by inversion were identical to the values used for forward modelling of the synthetic data.

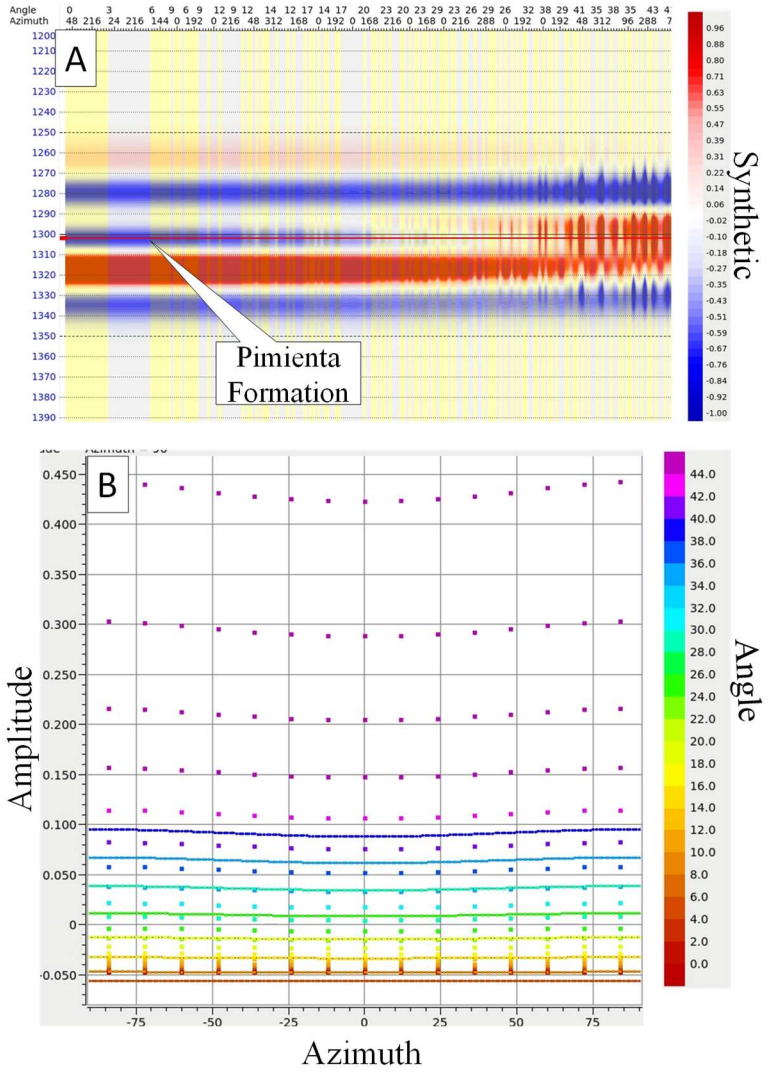

Figure 5.48. Synthetic azimuthal gather created using the velocities and densities from well logs.

In this thesis, AVA inversion (based on a simplified Zoeppritz equation) was used to estimate elastic stiffness coefficients from 3D prestack 360° data acquired at the Pimienta Formation field. These estimated isotropic elastic stiffness coefficients can be useful for identifying sweet spots, i.e., zones of high hydrocarbon potential. In addition, AVAZ inversion (based on a simplified Ruger's equation describing reflections from HTI media) was used to estimate four anisotropic parameters from azimuthally varying reflection amplitudes and NMO velocities. These estimated anisotropic parameters can be useful for estimating fracture density and orientation in subsurface rock formations. An ambiguity exists in the estimated fracture plane orientation. This ambiguity can be resolved by using results of VVAZ inversion as a priori information for the AVAZ inversion. Because, the reservoir of Pimienta Formation is unconventional and fractures play a significant role in production, anisotropy intensity and orientation maps were calculated.

Four snail gathers were performed in the Hampson and Russell software along the horizontal wellbore Anhelido-1H in order to see the residual time travel difference as a function of angle incidence (Figure 5.49). Slightly differences in the fast and slow velocities can be seen. Then a stack angle process was applied to the azimuthal gathers to separate the outputs into four azimuthal sectors (Figure 5.50) for the next step in seismic inversion (addressed in Chapter 6).

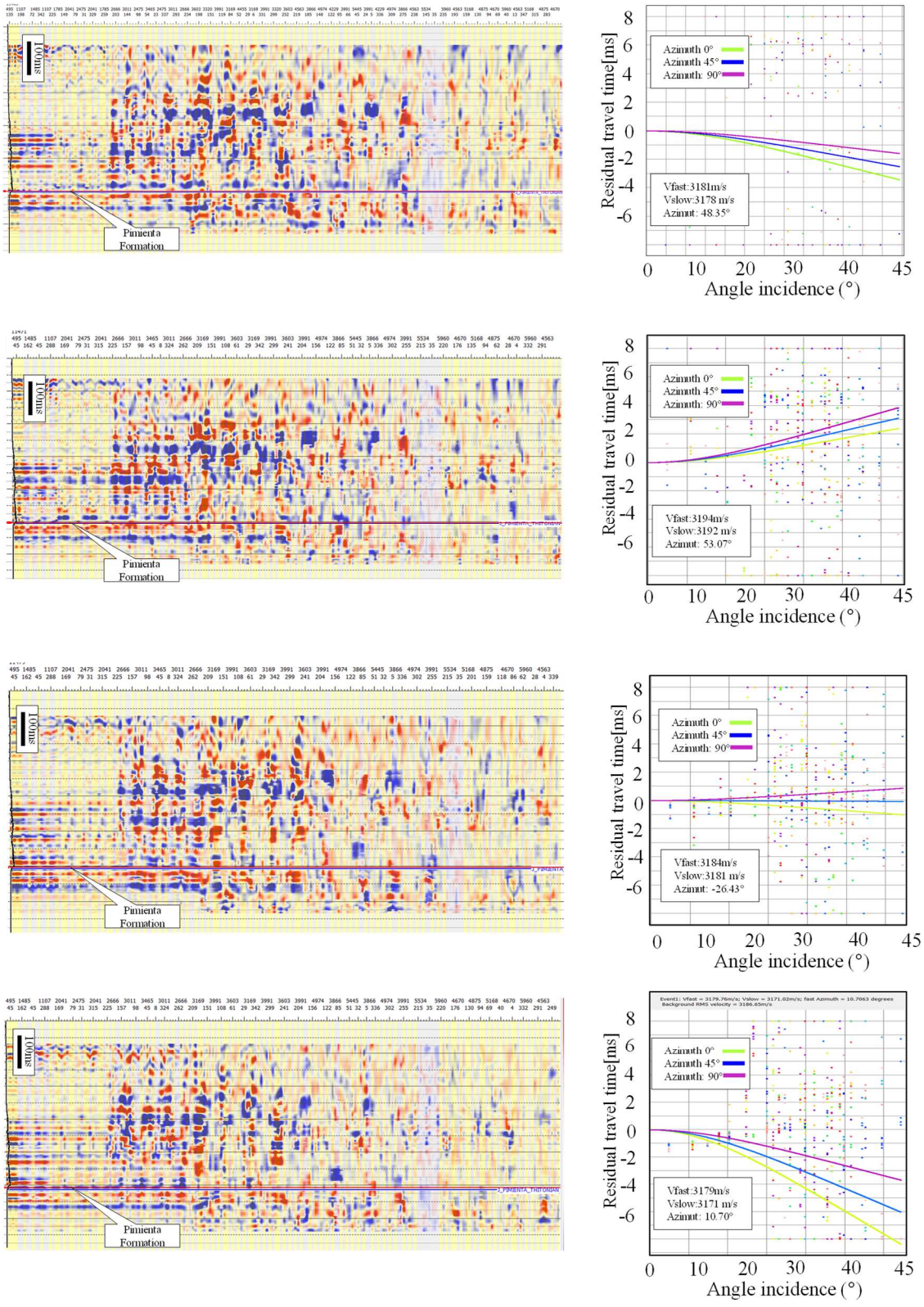

Figure 5.49. Four snail gathers along horizontal side of the wellbore Anhelido-1H to investigate the differences in residual travel time of V_{fast}, V_{slow} *and azimuth*.

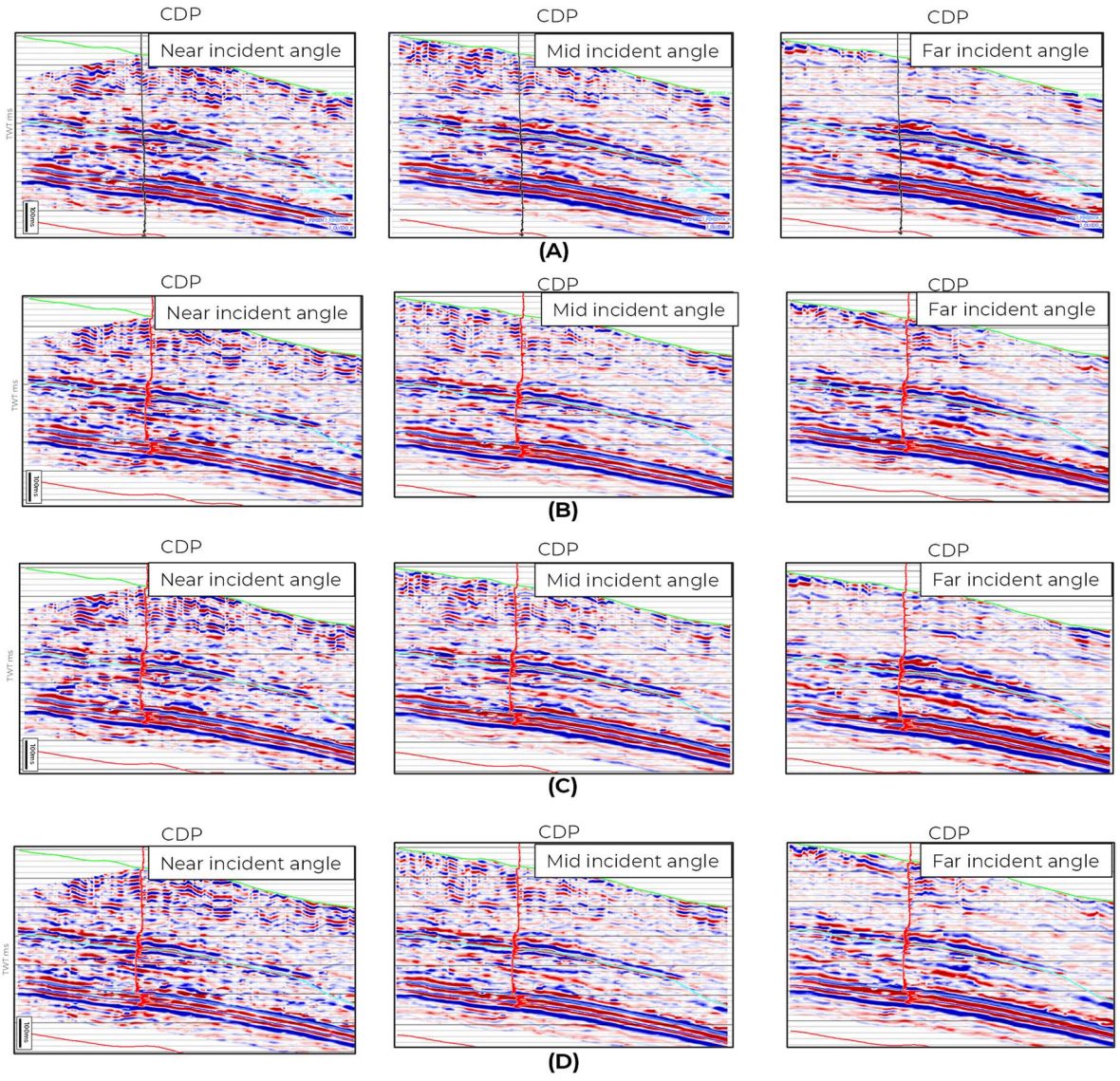

Figure 5.50. CDP angle gather subdivided in near, Mid, and far angle incidence; A) Angle gather sector 1(0-90°); B) Angle gather sector 2(90-180°); C) Angle gather sector 3(180-270°); D) Angle gather sector 4(270-360°).

Chapter 5 (section 5.3.2)

Correction in parameters for crack porosity and crack density have been made in this section (Table 5.8) and the synthetic seismic models in Hampson and Russell software

Well	Model	e *Crack density*	α *Aspect ratio*	ϕ *Crack* Porosity	ε	γ	δ	Azimuth(°)
Anhelido-1	Hudson	0.03	0.1	0.02	-0.08	-0.04	-0.07	45
	Linear-slip	-----	0.1	-----	-0.01	-0.05	-0.13	45

Table 5.8: Parameters for modelling in Hampson & Russell software at Anhelido-1.

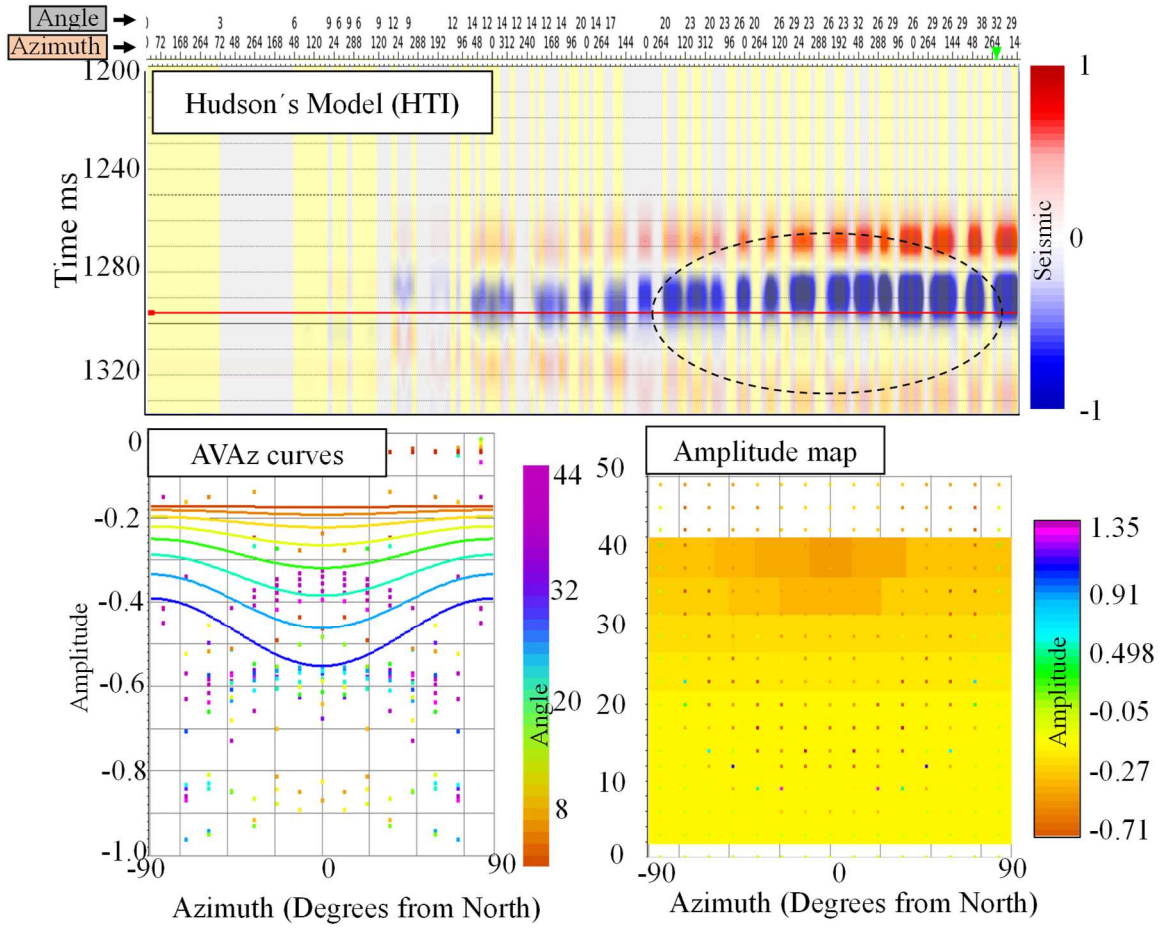

Figure 5.56. (A) Synthetic azimuthal gather at Anhelido-1 depth 2113m generated using the Hudson model based on fracture models listed in table 5.7 it is observed amplitude distortion in far angle incidence (dashed black polygon); (B) Azimuthal AVO curves are created with this model color-coded with incidence angle; (C) Amplitude map variations with azimuth to emphasize the azimuthal changes within the common angles common azimuth gather (COCA).

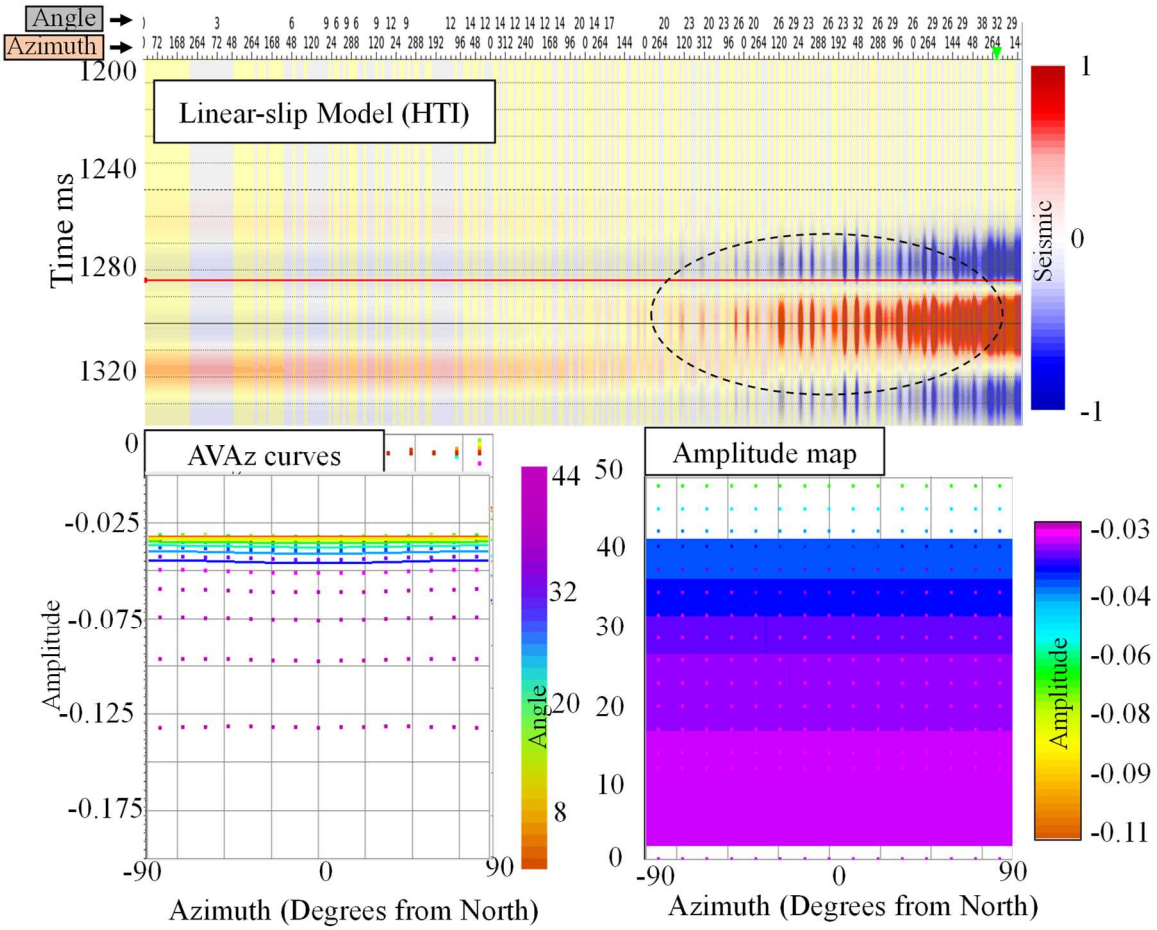

Figure 5.57. (A) Synthetic azimuthal gather at Anhelido-1 depth 2113m generated using the Linear-slip model based on fracture models listed in table 5.7. Amplitude distortion is observed in far angle incidence (dashed black polygon); (B) Azimuthal AVO curves are created with this model color-coded with incidence angle; (C) Amplitude map variations with azimuth to emphasize the azimuthal changes within the common angles common azimuth (COCA).

9. Discussion of the concept of anisotropic brittleness- what does this really mean and the limitations of the brittleness index

Chapter 5 (section 5.4.3)

Young's modulus, Poisson's ratio, and fracture excess compliances, which are related to rock brittleness and natural fractures, can be used to evaluate the hydraulic fracturing potential of a prospect or area and help identification of the optimized sweet spots in unconventional reservoirs. I aim to characterize the elastic properties of rock brittleness and compliance from the observable wide-azimuth seismic data via the inversion of Young's modulus, Poisson's ratio. Using the linear slip model, we first derive the perturbations in stiffness components in terms of Young's modulus, Poisson's ratio, and excess compliances for the case of weak anisotropy and small contrasts in elastic properties across the interface. Based on the relationship between scattering function and reflection coefficient in weakly anisotropic media, we then derive a linearized PP-wave reflection coefficient and an azimuthal impedance equation as a function of Young's modulus, Poisson's ratio, density, and excess compliances. Finally, I develop an impedance variation with incident angle and azimuth inversion method to estimate the Young's modulus, Poisson's ratio, and excess compliances in a Bayesian framework. The approach is implemented in a two-step inversion: azimuthal inversion and estimation of model parameters. A synthetic test demonstrates that the model parameter can be reasonably estimated even when containing moderate noise. A field data set test reveals that the inversion results agree well with the well log interpretation.

The anisotropic brittleness refers to the quality of brittleness with different values when measured along axes in different directions in 3D azimuthal seismic interpretation. The presence of structures such as cleavage, schistosity, foliation, joints, or lamination, and bedding planes can cause such anisotropy of brittleness in the rocks. On the whole, the anisotropy of brittleness is seldom investigated. Hou et al. (2016) investigated the brittleness anisotropy of Longmaxi shale with the

bedding angle of 0°, 30°, 60°, and 90° under triaxial compression conditions. Two kinds of stress-strain curve approaches were used to assess the anisotropic brittleness index of Longmaxi shale.

The concept of anisotropic brittleness is related to the calculation of brittleness in two principal directions from Young's modulus (θ), Poisson's ratio (θ) addressed in sub chapter 5.2.3.2. For this case the velocities P and S in these two main directions were taken into account.

Two symmetry axes of the shale formation were used in this project e.g ($\theta = (0°, 90°)$) for the estimation of anisotropic brittleness. Here the brittleness $Brit_V$ is in the symmetry axis equal to 0° and $Brit_H$ is in the symmetry axis equal to 90° based on the renormalized Young´s Modulus $E(\theta)$ and Poisson´s Ratio $v(\theta)$ (Figure 5.68).

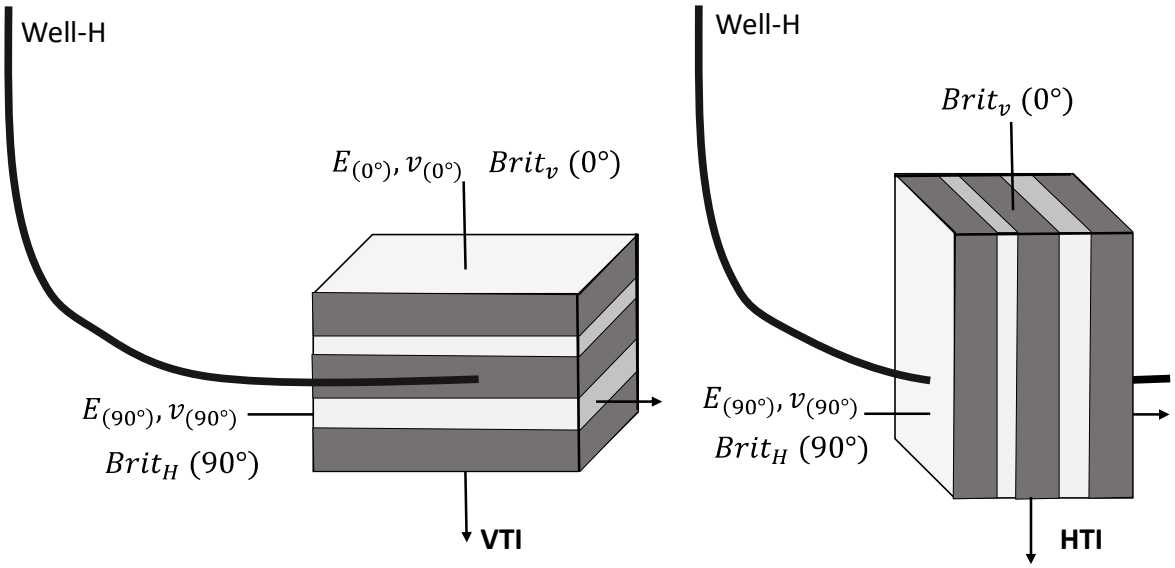

Figure 5.68. Scheme of brittleness calculation **(**$Brit_V$ (0°)) is in the symmetry axis equal to 0° **and (**$Brit_H$ (90°)) is in the symmetry axis equal to 90°.

In unconventional reservoirs brittleness is a significant parameter for the definition of a shale sweetspot and is critical in the hydraulic fracture technology and the design of horizontal well trajectories (Jarvie, et al. 2007). There are several equations in the literature to estimate this property one of the most accurate is the laboratory measurements. However, to acquire measurements are expensive and limited in samples that is why the use of 3D seismic data or logging data are more

likely alternative to be used for the calculation of brittleness (Goodway et al. 1999, 2010). This property cannot be measured directly from seismic or well log data (Li et al. 2012).

Two types of brittleness index are in the literature, the mineralogy-based method, and the elastic parameter-based method. Both methods are predictive and are widely used in the oil industry. The one preferred in this project is the elastic-parameter-based method using Young´s modulus, Poisson´s ratio, Lame constants. This method seems to give better results for brittleness estimation because it contains information pertaining to both pore fluid and mineralogy. In contrast the prediction of brittleness based on mineral composition alone is still widely used since the parameters are easy to obtain directly from core, albeit at a high cost.

Young's modulus and Poisson's ratio, related to mineral, porosity, total organic carbon (TOC) content, and rock strength, are treated as an indicator of rock brittleness, which play significant roles in seismic reservoir characterization to evaluate hydraulic fracturing and infer sweet spots of unconventional reservoirs (Harris et al. 2011; Sena et al. 2011). Young's modulus and Poisson's ratio are usually estimated from surface seismic data indirectly with the computation of P- and S-wave velocities and density to perform the "sweet spot" discrimination and optimization of horizontal well placement (Sena et al. 2011). There are, however, two difficulties. Firstly, when computing the Young's modulus, the density needed is more problematic than the inversion of P-wave and S-wave velocities even with the seismic data containing the information of large incident angles or offsets (de Nicolao et al. 1993; Debski and Tarantola 1995; Downton 2005; Kabir et al. 2006). Secondly, the indirect computation of Young's modulus and Poisson's ratio accumulates errors and causes much more bias in parameter estimation (Zong et al. 2013a, b; Yin and Zhang 2014). In this paper, we demonstrate an approach of direct inversion for Young's modulus, Poisson's ratio, and density from surface seismic data to avoid the indirect estimation and accumulated errors.

The first process of azimuthal simultaneous inversion from partial angle-stack seismic data is generally implemented incorporating the seismic wavelets at different incident angles and azimuths

convoluted with the normal-incidence reflection coefficient, in which the inversion algorithm used in this process is the same as that of post-stack seismic inversion (Russel and Hampson 1991). Here I implement the process of azimuthal simultaneous inversion for Young's modulus, Poisson's ratio, elastic parameters to use in Rickman equation in four azimuthal inversion.

Chapter 5 (section 5.4.3.1)

Limitations of brittleness index

The Brittleness Index (BI) is a widely used tool in the oil and gas industry to characterize the mechanical properties of rocks in unconventional reservoirs. The index is defined as the ratio of Young's modulus (E) to the Poisson's ratio (ν), which is used to describe the elastic behavior of a material. The BI is an indicator of the rock's brittleness, which is an important factor in determining the production potential of unconventional reservoirs. However, despite its widespread use, the BI has several limitations that must be considered when interpreting its results.

One of the major limitations of the BI is that it does not account for the influence of pore pressure on the mechanical properties of rocks. In unconventional reservoirs, pore pressure is often high, which can result in a reduction of rock strength and an increase in rock deformability. This can lead to inaccurate results when using the BI to assess the brittleness of these rocks. For example, a rock with a low BI may be considered brittle, while in reality, it may be much more deformable due to high pore pressure. This can result in incorrect predictions of the production potential of a reservoir and can lead to significant economic losses.

Another limitation of the BI is that it does not account for the effects of stress anisotropy. In unconventional reservoirs, the stress state can be highly anisotropic, which can result in different mechanical behavior in different directions, and these can be difficult to capture using the BI. In these

cases, more sophisticated techniques, such as multiaxial testing or numerical simulations, may be required to accurately characterize the mechanical properties of the rock. For example, for this thesis, The BI was computed in different directions based on the results of the seismic inversion in 4 azimuthal sectors (Chapter 6 section 6.2.3).

The BI is also subject to the usual measurement errors of the data used to calculate this parameter. In order to calculate the BI, accurate measurements of both Young's modulus and Poisson's ratio are required. However, obtaining these measurements can be challenging in unconventional reservoirs, particularly in the case of low permeability rocks. In these cases, the measurement of mechanical properties can be influenced by the presence of fluid and by the rock's microstructure, making it difficult to obtain accurate results.

Finally, the BI is limited by its simplicity. The BI is a single parameter that is used to describe the mechanical properties of rocks, and it does not account for the complex interactions between the various rock properties that can impact the production potential of an unconventional reservoir. For example, it does not account for the effects of rock grain size, mineralogy, or fluid saturation on the mechanical properties of the rock. To overcome these limitations, more comprehensive and sophisticated techniques, such as rock physics models, may be required.

In conclusion, the Brittleness Index is a widely used tool in the oil and gas industry to characterize the mechanical properties of rocks in unconventional reservoirs. However, it has several limitations that must be considered when interpreting its results. These limitations include its lack of consideration for the influence of pore pressure, stress anisotropy, data accuracy, and its simplicity. Therefore, it is important to consider these limitations and to use additional techniques when necessary to accurately assess the production potential of unconventional reservoirs.

Chapter 5 (section 5.4.3.2)

Anisotropic brittleness concept using azimuthal Inversion

Anisotropy refers to the property of a material that exhibits different physical and mechanical characteristics in different directions. This concept is of particular importance in the field of rock physics, where it is used to describe the behavior of rocks under stress and strain. Anisotropy in rock can be attributed to a number of factors, including mineral orientation, layering, and pore orientation. One important manifestation of anisotropy in rock is anisotropic brittleness. This term refers to the observation that rocks can exhibit different levels of brittleness depending on the direction of loading. For example, a rock may be relatively brittle in one direction, but more ductile in another.

The degree of anisotropic brittleness in a rock is dependent on a number of factors, including mineral composition, texture, and structure. For example, rocks that contain minerals that have a preferred orientation, such as shale, tend to be more anisotropically brittle than rocks with random mineral orientation, such as sandstone. Additionally, the presence of layering or bedding can also contribute to anisotropic brittleness, as the layers may have different mechanical properties and respond differently to stress.

The study of anisotropic brittleness in rock physics has important implications for a number of fields, including geology, mining. For example, a better understanding of the brittleness of rocks can help geologists to predict potential failure mechanisms that may have impact in the wellbore design for fracking technology.

Anisotropic brittleness is an important concept in the field of anisotropic seismic inversion, as it can affect the seismic wave propagation and, therefore, impact the results of seismic data analysis.

Anisotropic seismic inversion refers to the process of inferring the subsurface velocity structure of a rock mass from seismic data, considering the anisotropic nature of the rock (Chapter 6, section 6.2.3) The anisotropic brittleness of rocks can cause variations in seismic wave velocities and amplitudes, which can result in distorted images of the subsurface structure. This can impact the accuracy of the inversion results and lead to misinterpretation of the subsurface properties. For example, anisotropic brittleness can cause differences in the wave velocities in different directions, which can lead to errors in the estimated subsurface velocity structure.

To account for the effects of anisotropic brittleness in seismic inversion, it is necessary to consider the anisotropy of the rock. This can be done by using anisotropic seismic inversion volumes addressed in Chapter 6 and incorporating anisotropic parameters, such as the Thomsen parameters, into the inversion process used to describe the degree of anisotropy in terms of the relative wave velocities and attenuation in different directions as shown in chapter 6 where the seismic was divided into several sectors ordered by azimuth and angle of incidence to obtain P-S impedances in four main directions.

In conclusion, the concept of anisotropic brittleness is important in the field of anisotropic seismic inversion, as it can impact the seismic wave propagation and, therefore, the accuracy of the inversion results. To account for the effects of anisotropic brittleness, it is necessary to consider the anisotropy of the rock mass and incorporate anisotropic parameters into the inversion process. This can lead to more accurate images of the subsurface velocity structure and a better understanding of the subsurface properties.

10. Phase of a seismic wavelet (seismic inversion)

Chapter 6 (section 6.1.2)

The seismic wavelet is the important link between seismic data and stratigraphy as well as rock properties of the subsurface. Seismic wavelet estimation is done to deconvolve the seismic trace, tie the well log to the seismic data, and design inversion operators.

In the stationary case, the seismic trace $s(t)$ can be modeled by the convolution of the seismic wavelet $w(t)$ and the reflectivity $r(t)$ plus noise $n(t)$ (Sheriff and Geldart, 1995)

$$s(t) = w(t) * r(t) + n(t)$$

Here we ignore all the other physical effects of wave propagation such as wavefront spreading, transmission loss, multiples, attenuation, and anything else conceivable. Noise $n(t)$ is assumed to be white and stationary.

Two kinds of idealized wavelets are most common in geophysics. One is the minimum phase wavelet, which models the recorded seismic wavelet. It has no energy before time zero and has most of its energy concentrated at the front. The other is the constant-phase wavelet, which models the residual wavelet after deconvolution. It has energy before time zero and has a constant-phase across dominant frequencies. Among constant-phase wavelets, the zero-phase wavelet, which is symmetrical about time zero, is the best for interpretation (Simm and Bacon, 2014). Figure 6.2 shows a minimum-phase wavelet and a 100-degree phase wavelet in both time and frequency domains. The statistical wavelet method estimates the wavelet from the seismic data alone. Take the seismic trace $s(t)$ and calculate its autocorrelation so no well data is considered in this method.

Perhaps the most common type of wavelet used for seismic data is the zero-phase wavelet. When compared to minimum phase wavelets, these zero phase wavelets are symmetrical and are very broad band in the frequency domain. That being the case, an investigation into the changes that may occur when a zero-phase wavelet is used in the reflectivity analysis is done.

The full wavelet method uses both the seismic and reflectivity to determine the amplitude and phase spectra of the wavelet by applying a least-square filter which shapes the reflectivity to the seismic. An exact wavelet can be extracted without assumption about its amplitude or phase. However, this method is very sensitive to the quality of seismic-to-well ties (Hampson-Russell Software, 2013).

Wavelets are transient waveforms with a finite duration. They can be minimum, maximum, or mixed phase. A minimum phase wavelet has most of its energy at the onset of the time series, while a maximum phase wavelet has most of its energy at the end of the time series. Mixed phase wavelets have their energy distributed throughout the time series. In addition, a wavelet is realizable if it is finite in length (i.e., a finite time series) and is causal if it is zero for all negative times. Hence, a minimum phase wavelet is one that is minimum phase, realizable, and causal. These kinds of wavelets have the least energy delay. Mathematically, a stable inverse means that the filter coefficients make a convergent series. That is, they decrease with increasing time and vanish at infinity. This means that a stable inverse filter has finite energy. Minimum phase wavelets have stable inverses, but maximum and mixed phase wavelets do not.

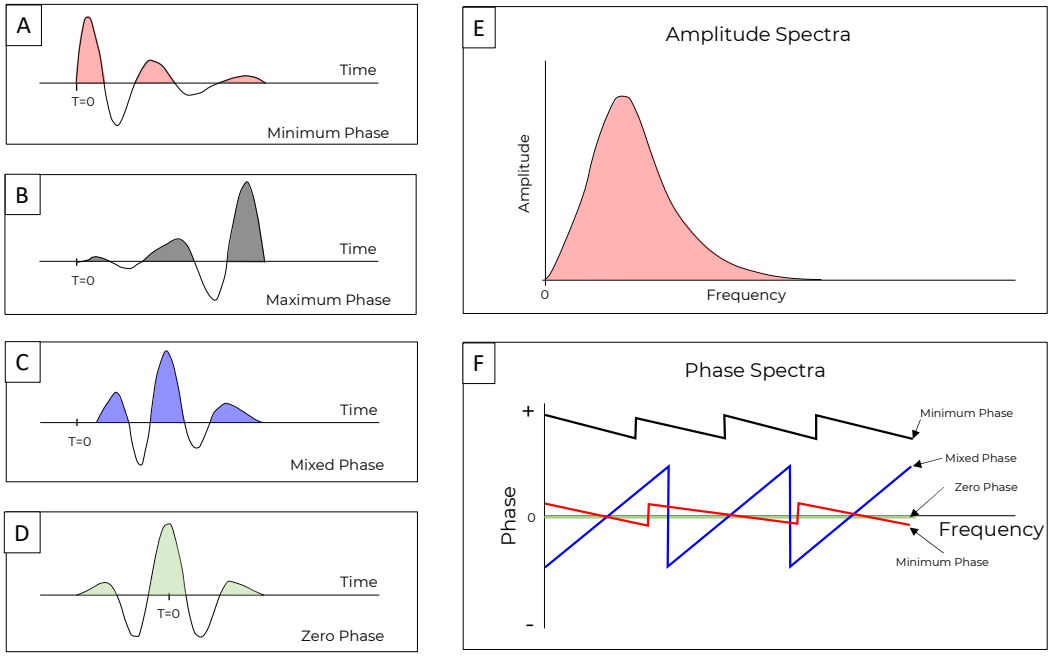

Figure 6.2 Phase wavelet examples and amplitude spectra.

Wavelet estimation process

Wavelet estimation lies at the heart of any seismic inversion project. The inferred shape of the seismic wavelet will strongly influence the assessment of the reservoir quality. I used Hampson and Russell software to generate an estimated wavelet. This exercise will go through the model driven wavelet estimation process (known as the Roy White estimation), which is the most common wavelet estimation technique for reservoir characterization.

The Roy White methodology (White, 1980) allows us to quantify how good a well tie is, and hence, demonstrate improvement after log editing or seismic conditioning. It allows us to analyze error bars on the seismic wavelet spectrum so we can see whether the wavelet is well determined.

The Roy White method is essentially a coherence matching technique. The workflow can be summarized as follows:

1. From well log data we estimate the earth reflectivity.

2. A volume of seismic data around the well is scanned for the best statistical fit to the synthetic trace, and a wavelet is estimated at that trace.

3. The filter providing the best match between the earth reflectivity and the seismic is our best estimate of the original seismic wavelet.

In an inversion, we are attempting to remove this wavelet from the seismic, so clearly, it's vital to know what it looks like. Figure 6.3 shows the schematized Roy White methodology and Figure 6.4 the wavelets used in this project.

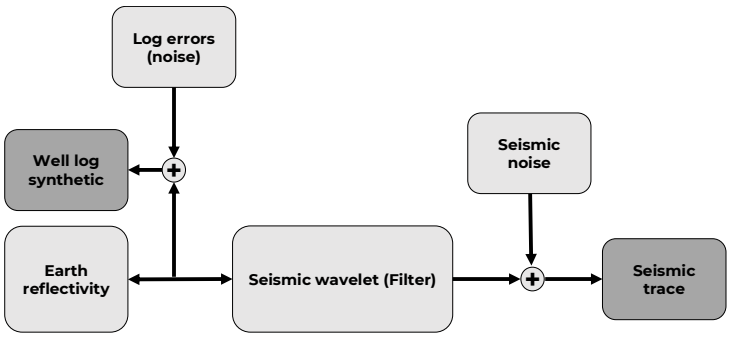

Figure.6.3 The Roy White methodology.

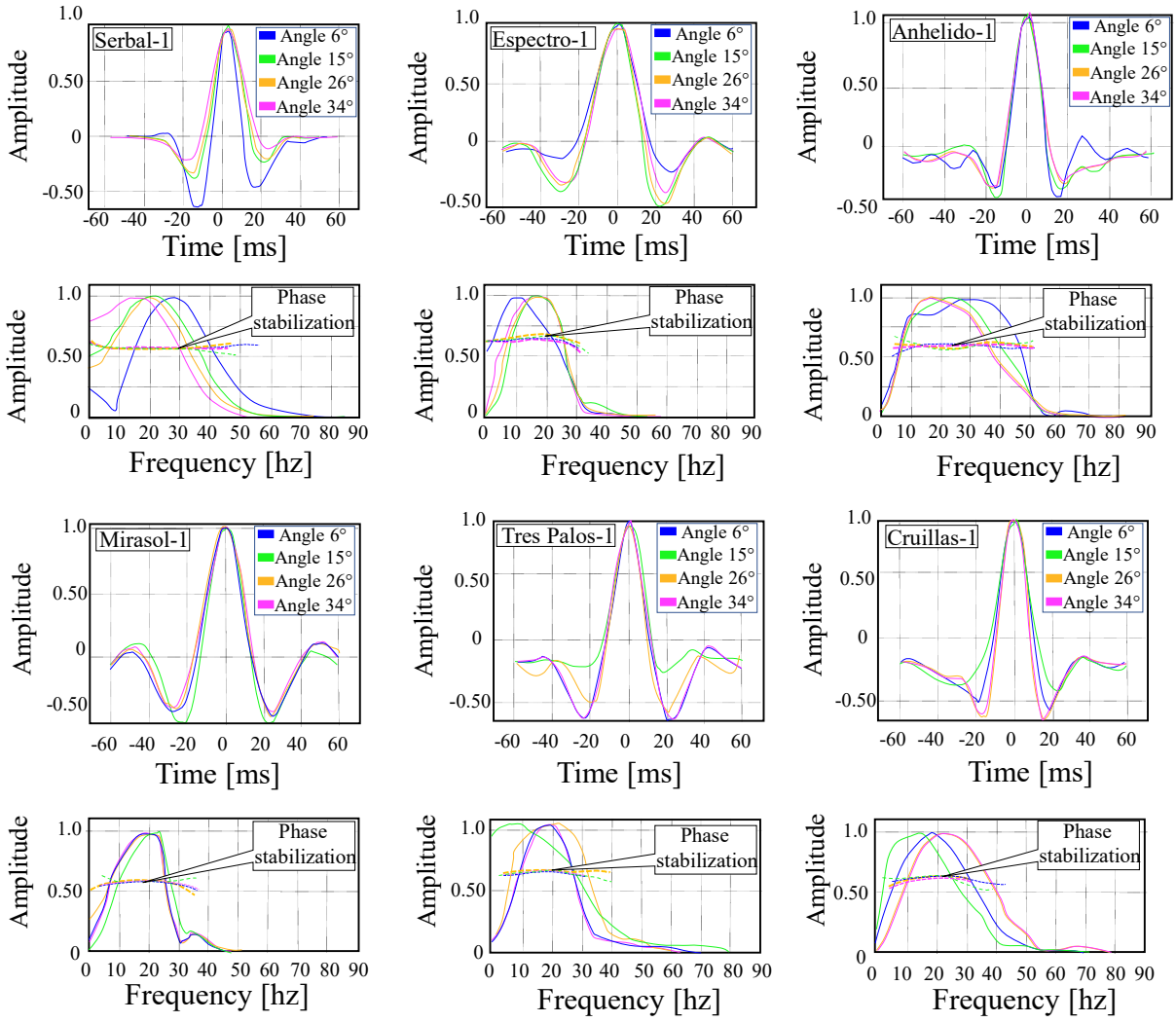

Figure 6.4. Wavelets time response used in the project using Roy White approach near zero wavelet for the inversion process (6 wells in total in the study area); then in Anhelido-1 more wavelets estimation will be calculated in for azimuthal sectors in this chapter (Figure 6.7).

When estimating a wavelet, the chosen method depends on the data availability. If there is well data available, a wavelet can be estimated with the model-driven technique in estimate wavelet amplitude and phase spectra. The algorithm uses the well log data and the seismic to find the wavelet that produces the best synthetic match to the seismic data. Use of multiple wells and multiple traces per well reduces the likelihood that noise in the seismic will be incorporated into the wavelet.

Roy White defined two important concepts useful to quantify the quality of a well tie: the goodness of fit, and the wavelet accuracy. Maximizing these two measures should deliver the best wavelet, with the smallest error bars.

The goodness of fit measurement is called PEP, the proportion of energy predicted from the synthetic. Numerically, it's approximately the square of the cross-correlation, and a value greater than 0.7 is considered good.

Goodness of fit is not a measure of the accuracy of the wavelet. The cross-correlation increases with increase in wavelet length, but the longer the wavelet is, the more chance that noise is also being matched.

If a value of one is achieved, it implies a perfect match between the seismic and the synthetic, using the estimated wavelet (i.e., the residual is zero).

The goodness of fit is defined by equation [1]:

$$PEP = 1 - (energy\ in \frac{residuals}{trace\ energy})$$

The maximum PEP value is not necessarily found at the well location or along a composite trace along the well trajectory. In practice, a seismic cube is scanned around the well location in order to find a maximum PEP. This approach is preferable since positioning of seismic energy during migration carries uncertainty, well positioning itself may be uncertain, and lateral stability of the estimation may be better understood with PEP maps.

The wavelet accuracy is given by NMSE, the normal mean squared error, that is calculated using equation [2]:

$$NMSE = \frac{0.59L}{T} * \frac{1 - PEP}{PEP}$$

Where L is the wavelet length and T is the length of the time window from which the wavelet is estimated. A good well tie has NMSE less than 0.2.

The window T we choose is a function of the frequency content of the seismic or the bandwidth. The higher the bandwidth, the smaller the time window.

The wavelet length is then simply calculated from the time window. Usually, L is a value between a 1/3 and a 1/7 of the time windows used.

The relationship between the Goodness of Fit and Wavelet Estimation error as a function of the ratio $\frac{Wavelet\ Lenght(L)}{Time\ Window\ (T)}$ can be seen in Figure 6.5.

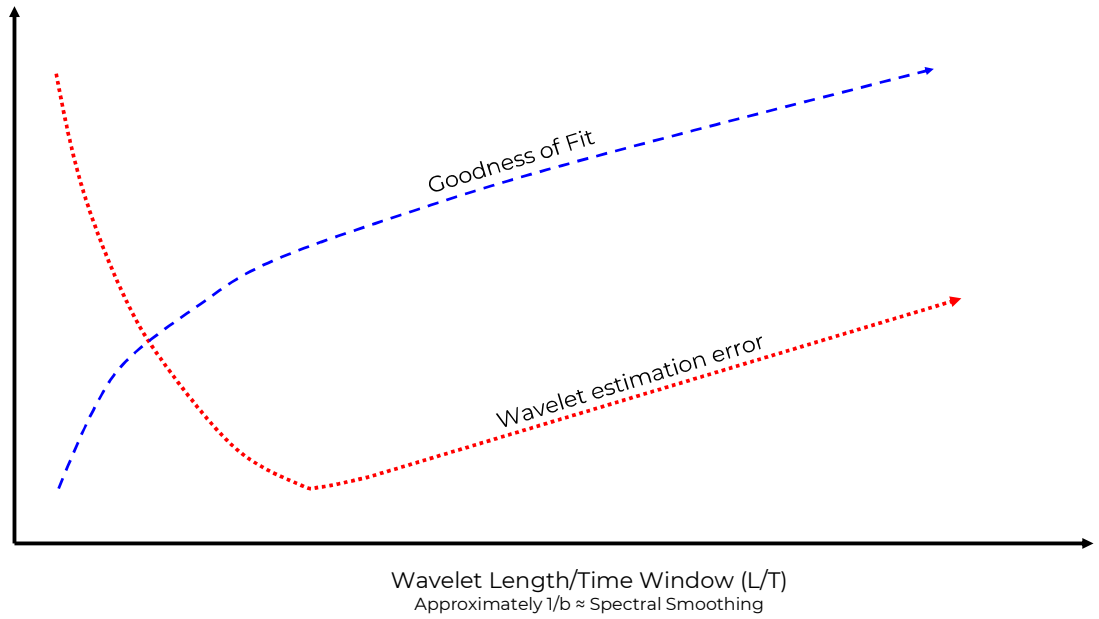

Figure 6.5. Goodness of Fit and Wavelet Estimation Error vs. L/T ratio. As the (L/T) ratio goes up, or the wavelet length to window length goes up, the goodness of fit, or PEP always increases.

The longer the ratio L/T is, the better it can fit everything in the time window. But as the wavelet gets longer, the wavelet begins to also fit noise, and the wavelet estimation error goes up. At the opposite end of the axis, the goodness of fit is poor, as we are over-smoothing in the spectral domain. The idea is to find the optimum zone, where the error is low and the goodness of fit is high.

Without well control, the wavelet estimation is based on statistical techniques. This process is done in two steps: estimation of the wavelet amplitude spectrum, followed by the estimation of its phase spectrum. When estimating the amplitude spectrum without wells, the basic inputs are the seismic

traces and a time gate. The estimate wavelet amplitude spectrum option produces a zero-phase wavelet. The phase of the seismic wavelet can be estimated with the estimate wavelet constant phase spectrum option. In this case, the operator assumes a constant wavelet phase and models the data using a range of phase rotations. The correct phase shift is assumed to be that which produces the spikiest model. Knowledge of the wavelet polarity is necessary, however, since this algorithm is insensitive to polarity.

Some projects can benefit from the use of the two methodologies together. One example of this is in areas where the well control is only available shallower than the zone of interest. In this case, a shallow wavelet can be estimated using the model-driven technique in estimate wavelet amplitude and phase spectra. The amplitude spectrum of the deeper zone of interest can be derived using an estimated wavelet amplitude spectrum. With merged wavelet amplitude and phase spectra the deeper amplitude spectrum is then merged with the shallower phase spectrum to create a composite wavelet. Another example of where combining the techniques can be beneficial is when the model-driven technique cannot adequately capture the seismic amplitude spectrum. In such case, a wavelet with the amplitude spectrum of the seismic data, derived with estimate wavelet amplitude spectrum, can be used as an *a priori* wavelet to influence the results of the model-based estimate wavelet amplitude and phase spectra.

In the case when positioning problems with the well or the seismic data are suspected, the estimated wavelet amplitude spectrum and estimated wavelet constant phase spectrum can be used with the well at the initial position. This wavelet can then be used with the well to find the optimum location for wavelet estimation using the end optimal well position (vertically and laterally) option in wavelets. Once an improved location is found, the model-driven technique in estimate wavelet amplitude and phase spectra can be used to obtain an improved wavelet.

When using the model-driven wavelet estimation scheme, it is recommended that wavelets modules are used to find the best wavelet and well tie. The wavelet is applied and the synthetic to seismic

comparison can be used to judge the quality of the wavelet. Moreover, adjustments to the well logs can be made and immediately saved for use in wavelets. In turn, in wavelets, the edited wells are used to improve the estimate of the wavelet. Here is the suggested workflow:

Within the wavelets module I created a synthetic wavelet to obtain an initial wavelet used to start the process of tying the well. Then I created and edit the time/depth relationship by bulk shifting and stretch/squeezing as necessary. When an initial tie is performed, the well is saved as first version.

Following this, I return to the embedded wavelets and calculate a new wavelet using the estimate wavelet amplitude and phase spectra option. The process of editing the time/depth relationship and estimating a new wavelet is repeated as necessary until a satisfactory wavelet and well tie is obtained.

11. TOC calculation in different azimuth sectors based on inverted data (A discussion of the concept of anisotropic TOC- how can a volume fraction be anisotropic?)

Chapter 6 (section 6.4.1)

In this section the term of anisotropic TOC has been corrected , TOC is not anisotropic and is described below as TOC calculated in different azimuths.

Total organic carbon (TOC) refers to the amount of carbon that is present in the organic matter within a rock or sediment sample and is a weight percent (https://www.sciencedirect.com/topics/earth-and-planetary-sciences/total-organic-carbon). Whilst the TOC is not inherently anisotropic, the distribution of organic matter within the rock or sediment can be highly anisotropic, which can result in anisotropy in TOC for samples measured with some directional component.

TOC values can vary greatly depending on the depositional environment, source of organic matter, and diagenetic history of the rock or sediment (Bohacs et al. 2005). For example, rocks or sediments that were deposited in environments with high organic productivity, such as swamps or lakes, tend to have higher TOC values compared to those deposited in environments with low organic productivity, such as fluvial systems. Additionally, the source of the organic matter, such as algae, plants, or bacteria, also influences the organic carbon content.

The presence of bedding or layering within the rock or sediment can result in anisotropy in organic carbon content, with higher or lower concentrations of organic matter in certain layers (Morgans-Bell et al. 2001). Additionally, the orientation of pores or fractures within the rock or sediment can also result in anisotropy in organic carbon content, as organic matter may preferentially accumulate in certain directions depending on sediment transport directions, or current patterns in the stagnating water bodies, for example.

To summarise, although TOC itself is not itself anisotropic as a single measurement, the distribution of organic matter within rocks or sediments can result in anisotropy in TOC content when sampled in different orientations. This can be due to factors such as layering, pore orientation, and other geological structures. Understanding the anisotropy in TOC content can be important for various applications, such as resource exploration, environmental monitoring, and carbon sequestration.

In my study, the TOC showed values which vary depending on the direction in which it this measure of organic carbon content estimated, as expressed in the results of the azimuthal inversion. The TOC was estimated according to the Equation 6.23 by incorporating the azimuth as an additional variable resulting in the value changes in this property in different directions where a new equation has been proposed to estimate the TOC in different azimuths updating the equation developed by Vernik (2002). The seismically estimated TOC values were computed in four sectors, of which the sector oriented 90°-180° turned out to have the highest values (Figure 6.20).

Therefore, the seismically parameterized measure of TOC can be seen to be azimuthally dependent.

12. Attribute extraction on TOC and Brittleness

Chapter 6 (section 6.4.5)

Seismic attributes are quantities (Misra and Mukherjee, 2018) derived from the inverted seismic information that describes the shape or other characteristics of a seismic inverted trace over a specified time interval. The map attributes are important because they enable interpreters to extract more information from inverted seismic information. The seismic attributes addressed in chapter 6 were derived from the inverted traces of TOC and Brittleness for each azimuthal inverted sector, or from an interpreted seismic horizon like in this case using the top and base of Pimienta Formation.

Examples of seismic attributes are wavelet shape, frequency, amplitude, phase, and complex trace information contained in transforms of the real trace. Generally, we use three types of attributes: horizon attributes, interval attributes, and surface attributes.

For his project horizon TOC/Brittleness attributes in four azimuthal sectors are measured relative to an interpreted horizon. Theses horizon attributes usually measures the properties of TOC and Brittleness estimated from inverted data (P-Impedance, S-Impedance and Density) these properties take value through the horizon that has been mapped on the volumes of TOC (four azimuth sectors) and Brittleness (four azimuth sectors (in VTI/HTI modes) between top and base of the Pimienta Formation which are roughly 80m of thickness. For this case the horizon attribute took the RMS amplitude value at a particular location of the whole horizon (Figure 6.20 and Figure 6.27). We can look at the azimuthal sectors (0-90°,90-180°,180-270° and 270-360°) for both properties TOC/Brittleness in two modes (VTI and HTI in all azimuth sectors), and we can also look at the amplitude extraction along the horizon (Top of Pimienta Formation).

These attributes attempt the characterization of the reservoir within Pimienta Formation which will give the best property prediction calibrated with well log data at the well location. For example, Brittleness is a major rock property for effective reservoir stimulation in unconventional reservoirs.

Differentiating brittle from ductile rocks is key to performing efficient well location and completion. I calculated a brittleness index (BI) volume from horizon seismic data for the whole azimuthal sectors previously explained, calibrated by well logs, in the Pimienta Formation as well as the total organic carbon (TOC) which is an excellent indicator for the organic richness and the hydrocarbon potential of shale in unconventional reservoirs. However, common methods for TOC estimation have many underlying assumptions and rely on empirical formulas. This topic is addressed in Chapter 3.4. The TOC was estimated for azimuthal ranges using the inverted seismic data.

Appendix B DEMmodR1 graphical user interface

B.1 DEMmodR1.m

The effective medium DEM theory proposed by Kuster and Toksöz (1974) has been used to calculate the elastic moduli of mixture (oil, gas, kerogen, and water) and the organic shales. S_k, S_o, S_g and S_w are the saturation of kerogen, oil, gas, and water respectively, using DEMmodR1 developed in MATLAB.

Program (MATLAB source code "DEMmodR1" based on the Differential effective medium the to estimate the bulk K_{dry} and shear modulus μ_{dry}using this analytical model

```
function varargout = DEMmodR1(varargin)
% DEMMODR1 MATLAB code for DEMmodR1.fig
%      DEMMODR1, by itself, creates a new DEMMODR1 or raises the existing
%      singleton*.
%
%      H = DEMMODR1 returns the handle to a new DEMMODR1 or the handle to
%      the existing singleton*.
%
%      DEMMODR1('CALLBACK',hObject,eventData,handles,...) calls the local
%      function named CALLBACK in DEMMODR1.M with the given input arguments.
%
%      DEMMODR1('Property','Value',...) creates a new DEMMODR1 or raises the
%      existing singleton*.  Starting from the left, property value pairs are
%      applied to the GUI before DEMmodR1_OpeningFcn gets called.  An
%      unrecognized property name or invalid value makes property application
%      stop.  All inputs are passed to DEMmodR1_OpeningFcn via varargin.
%
```

```
%      *See GUI Options on GUIDE's Tools menu.  Choose "GUI allows only one
%      instance to run (singleton)".
%
% See also: GUIDE, GUIDATA, GUIHANDLES

% Edit the above text to modify the response to help DEMmodR1

% Last Modified by GUIDE v2.5 13-Feb-2023 21:03:24

% Begin initialization code - DO NOT EDIT
gui_Singleton = 1;
gui_State = struct('gui_Name',       mfilename, ...
                   'gui_Singleton',  gui_Singleton, ...
                   'gui_OpeningFcn', @DEMmodR1_OpeningFcn, ...
                   'gui_OutputFcn',  @DEMmodR1_OutputFcn, ...
                   'gui_LayoutFcn',  [] , ...
                   'gui_Callback',   []);
if nargin && ischar(varargin{1})
    gui_State.gui_Callback = str2func(varargin{1});
end


if nargout
    [varargout{1:nargout}] = gui_mainfcn(gui_State, varargin{:});
else
    gui_mainfcn(gui_State, varargin{:});
end
% End initialization code - DO NOT EDIT
```

```
% --- Executes just before DEMmodR1 is made visible.
function DEMmodR1_OpeningFcn(hObject, eventdata, handles, varargin)
% This function has no output args, see OutputFcn.
% hObject    handle to figure
% eventdata  reserved - to be defined in a future version of MATLAB
% handles    structure with handles and user data (see GUIDATA)
% varargin   command line arguments to DEMmodR1 (see VARARGIN)

% Choose default command line output for DEMmodR1
handles.output = hObject;

% Update handles structure
guidata(hObject, handles);

% UIWAIT makes DEMmodR1 wait for user response (see UIRESUME)
% uiwait(handles.figure1);

% --- Outputs from this function are returned to the command line.
function varargout = DEMmodR1_OutputFcn(hObject, eventdata, handles)
% varargout  cell array for returning output args (see VARARGOUT);
% hObject    handle to figure
% eventdata  reserved - to be defined in a future version of MATLAB
% handles    structure with handles and user data (see GUIDATA)

% Get default command line output from handles structure
varargout{1} = handles.output;
```

```
% --- Executes on button press in pushbutton1.
function pushbutton1_Callback(hObject, eventdata, handles)
% hObject    handle to pushbutton1 (see GCBO)
% eventdata  reserved - to be defined in a future version of MATLAB
% handles    structure with handles and user data (see GUIDATA)
global Depth Vp1 Vs1 bulklog phi Sw1 toc vclay vqz vca vdol asp Rmat Rw Roil Km Um

[file,path] = uigetfile({'*.xls;*.xlsx','Excel Files'},' Select data file');
filename = strcat(path,file);
data = xlsread(filename);

Depth = data(:,1);  %Depth (m)
Vp1 = data(:,2);    % P-wave log
Vs1 = data(:,3);    % S-wave log
bulklog = data(:,4);% Bulk Modulus log
phi = data(:,6);    % Porosity
Sw1 =  data(:,7);   % Water saturation
toc = data(:,8);    % TOC log
vclay = data(:,9);  % Vclay fraction
vqz=data(:,10);     % Quartz fraction
vca=data(:,11);     % Calcite fraction
vdol=data(:,12);    % Dolomite fraction

asp = str2num(char(get(handles.edit1,'String')));  %Aspect ratio
Rmat = str2num(char(get(handles.edit2,'String'))); %Matrix density
Rw = str2num(char(get(handles.edit3,'String')));   %Water density
```

```
Roil = str2num(char(get(handles.edit4,'String'))); %Oil density
Km=str2num(char(get(handles.edit6,'String')));     %Bulk Modulus matrix
Um=str2num(char(get(handles.edit7,'String')));     %Shear Modulus matrix

% --- Executes on button press in pushbutton2.
function pushbutton2_Callback(hObject, eventdata, handles)
% hObject    handle to pushbutton2 (see GCBO)
% eventdata  reserved - to be defined in a future version of MATLAB
% handles    structure with handles and user data (see GUIDATA)

global Depth Vp1 Vs1 bulklog phi Sw1 toc vclay vqz vca vdol asp Rmat Rw Roil Km Um
So1 =  (1-Sw1 );   %OIL SATURATION
Rsat1 = Rmat.*(1-phi)+(So1.*Roil + Sw1.*Rw).*phi;
ROH = Rsat1./1000;

Mu1 = (Vs1.^2.* Rsat1)
MU = Mu1./1000000

Ksat1 = Vp1.^2.*2.32- 4/3.*Mu1;
KSAT1 = Ksat1./1000000;

VPinsitu = (sqrt((KSAT1+((4/3).*MU))./2.32)).*1000;
tet =(asp./((1-asp.^2).^(3/2))).*(acos(asp)-(asp.*sqrt(1-asp.^2)));
g = ((asp.^2)./(1-asp.^2)).*((3.*tet)-2);

KU = Km/Um;
z = (1/(pi.*asp))-(1/(pi.*asp.*((3.*Km./(Um +1)))));
```

```
%%%%%%%%%%%%%  D E M Assuming Penny Cracks

%%%%%%%%%%%%%%%%%%%%%%%%%%%%%%

%%%%%%%%%%%%%%%%%%%%%%%%%%%%%%%%%%%%%%%%%%%%%%%%%%%%%%%%%%%%%%%%%%


v1 = Km/Um;

v2 =((3*Km)/Um)+ 4 ;

v3 = ((3*Km)/Um)+ 1 ;

v4 = ((3*Km)/Um)+ 2 ;


a = (-1.*(1/5))+(KU.*v2./(pi.*asp*(v3))) - (4.*v2/(15.*pi.*asp.*(v3))) - (8.*v2/(15.*pi.*asp.*(v4))) - (KU .*
((1./pi.*asp) + (27./(5.*pi.*asp*v3.^2)) + (16./(5.*pi.*asp.*v4.^2))));

b=(1/pi.*asp) + (27/(5.*pi.*asp.*v3.^2)) + (16./(5.*pi.*asp.*v4.^2));


x = (2- (3.*g) - (2.*tet))./(2 .* ((2.*tet)- (3.*tet.^2) - (2.*g)))


KDRY1 = Km.*((1-phi).^z./(1 + (b./a).*KU - (b./a).*KU.*(1 - phi).^a).^(x./b))


Vpsat=sqrt(((KSAT1+((4./3).*MU))./Rsat1)).*1000;

Vssat=sqrt(MU./2.32).*1000;

BulkMod = (((Vpsat.^2)-((4./3).*Vs1.^2)).*2.32)./1000000;


S0 = (2-(3.*g)-(3.*tet))./(2.*((2.*tet)-(3.*tet.^2)-(2.*g)));

S1 = ((tet-g)./(2-(3.*g)-(3.*tet)));

S2 = (4./3);

S3 = (2.*(tet-g))./(3.*((2.*tet)-(3.*tet.^2)-(2.*g)));

tm1=(1-phi).*S0;
```

```
tm2 = (S1+S2-S3)-(((S1-S3).*(S2-S3))./(S3+(Km./Um)));

tm3= (1 + ((b.*Km)./(a.*Um)) - ((b.*Km)./(a.*Um)).*((1-phi).^a)).^(S0./b);

tm4= (1 + ((b.*Km)./(a.*Um)) - ((b.*Km)./(a.*Um)).*((1-phi).^a)).^((S0./b)-1);

MDRY1= (Um.* (((tm1.*tm2)-a)./tm4));

axes(handles.axes1)

plot(Vp1, Depth,'k')

set(gca,'YDir','Reverse')

grid on

xlim([0 6500])

hold on

plot(Vpsat, Depth,'r')

title('DEM modelling')

xlabel('Velocity(m\s)')

ylabel('Depth(m)')

set(gca,'YDir','Reverse')

legend('Vp logged (m\s)','Vp model (m\s)');


axes(handles.axes2)

plot(Vs1, Depth,'k')

set(gca,'YDir','Reverse')

grid on

xlim([0 6500])

hold on

plot(Vssat, Depth,'R')

title('DEM modelling')

xlabel('Velocity(m\s)')

ylabel('Depth(m)')

set(gca,'YDir','Reverse')
```

```
legend('Vs logged (m\s)','Vs model (m\s)');


function edit6_Callback(hObject, eventdata, handles)
% hObject    handle to edit6 (see GCBO)
% eventdata  reserved - to be defined in a future version of MATLAB
% handles    structure with handles and user data (see GUIDATA)

% Hints: get(hObject,'String') returns contents of edit6 as text
%        str2double(get(hObject,'String')) returns contents of edit6 as a double
% --- Executes during object creation, after setting all properties.
function edit6_CreateFcn(hObject, eventdata, handles)
% hObject    handle to edit6 (see GCBO)
% eventdata  reserved - to be defined in a future version of MATLAB
% handles    empty - handles not created until after all CreateFcns called

% Hint: edit controls usually have a white background on Windows.
%       See ISPC and COMPUTER.
if ispc && isequal(get(hObject,'BackgroundColor'), get(0,'defaultUicontrolBackgroundColor'))
    set(hObject,'BackgroundColor','white');
end


function edit7_Callback(hObject, eventdata, handles)
% hObject    handle to edit7 (see GCBO)
% eventdata  reserved - to be defined in a future version of MATLAB
% handles    structure with handles and user data (see GUIDATA)
% Hints: get(hObject,'String') returns contents of edit7 as text
%        str2double(get(hObject,'String')) returns contents of edit7 as a double
```

```
% --- Executes during object creation, after setting all properties.
function edit7_CreateFcn(hObject, eventdata, handles)
% hObject    handle to edit7 (see GCBO)
% eventdata  reserved - to be defined in a future version of MATLAB
% handles    empty - handles not created until after all CreateFcns called
% Hint: edit controls usually have a white background on Windows.
%       See ISPC and COMPUTER.
if ispc && isequal(get(hObject,'BackgroundColor'), get(0,'defaultUicontrolBackgroundColor'))
    set(hObject,'BackgroundColor','white');
end


function edit2_Callback(hObject, eventdata, handles)
% hObject    handle to edit2 (see GCBO)
% eventdata  reserved - to be defined in a future version of MATLAB
% handles    structure with handles and user data (see GUIDATA)
% Hints: get(hObject,'String') returns contents of edit2 as text
%        str2double(get(hObject,'String')) returns contents of edit2 as a double
% --- Executes during object creation, after setting all properties.
function edit2_CreateFcn(hObject, eventdata, handles)
% hObject    handle to edit2 (see GCBO)
% eventdata  reserved - to be defined in a future version of MATLAB
% handles    empty - handles not created until after all CreateFcns called
% Hint: edit controls usually have a white background on Windows.
%       See ISPC and COMPUTER.
if ispc && isequal(get(hObject,'BackgroundColor'), get(0,'defaultUicontrolBackgroundColor'))
    set(hObject,'BackgroundColor','white');
end
```

```
function edit3_Callback(hObject, eventdata, handles)
% hObject    handle to edit3 (see GCBO)
% eventdata  reserved - to be defined in a future version of MATLAB
% handles    structure with handles and user data (see GUIDATA)
% Hints: get(hObject,'String') returns contents of edit3 as text
%        str2double(get(hObject,'String')) returns contents of edit3 as a double
% --- Executes during object creation, after setting all properties.
function edit3_CreateFcn(hObject, eventdata, handles)
% hObject    handle to edit3 (see GCBO)
% eventdata  reserved - to be defined in a future version of MATLAB
% handles    empty - handles not created until after all CreateFcns called
% Hint: edit controls usually have a white background on Windows.
%       See ISPC and COMPUTER.
if ispc && isequal(get(hObject,'BackgroundColor'), get(0,'defaultUicontrolBackgroundColor'))
    set(hObject,'BackgroundColor','white');
end


function edit4_Callback(hObject, eventdata, handles)
% hObject    handle to edit4 (see GCBO)
% eventdata  reserved - to be defined in a future version of MATLAB
% handles    structure with handles and user data (see GUIDATA)
% Hints: get(hObject,'String') returns contents of edit4 as text
%        str2double(get(hObject,'String')) returns contents of edit4 as a double
% --- Executes during object creation, after setting all properties.
function edit4_CreateFcn(hObject, eventdata, handles)
% hObject    handle to edit4 (see GCBO)
% eventdata  reserved - to be defined in a future version of MATLAB
% handles    empty - handles not created until after all CreateFcns called
```

```
% Hint: edit controls usually have a white background on Windows.
%       See ISPC and COMPUTER.
if ispc && isequal(get(hObject,'BackgroundColor'), get(0,'defaultUicontrolBackgroundColor'))
set(hObject,'BackgroundColor','white');
end
function edit1_Callback(hObject, eventdata, handles)
% hObject    handle to edit1 (see GCBO)
% eventdata  reserved - to be defined in a future version of MATLAB
% handles    structure with handles and user data (see GUIDATA)
% Hints: get(hObject,'String') returns contents of edit1 as text
%        str2double(get(hObject,'String')) returns contents of edit1 as a double
% --- Executes during object creation, after setting all properties.
function edit1_CreateFcn(hObject, eventdata, handles)
% hObject    handle to edit1 (see GCBO)
% eventdata  reserved - to be defined in a future version of MATLAB
% handles    empty - handles not created until after all CreateFcns called
% Hint: edit controls usually have a white background on Windows.
%       See ISPC and COMPUTER.
if ispc && isequal(get(hObject,'BackgroundColor'), get(0,'defaultUicontrolBackgroundColor'))
    set(hObject,'BackgroundColor','white');
end
% --- Executes on button press in pushbutton3.
function pushbutton3_Callback(hObject, eventdata, handles)
% hObject    handle to pushbutton3 (see GCBO)
% eventdata  reserved - to be defined in a future version of MATLAB
% handles    structure with handles and user data (see GUIDATA)
global Depth Vp1 Vs1 bulklog phi Sw1 toc vclay vqz vca vdol asp Rmat Rw Roil Km Um
```

```
% figure

asp2 = 0.1:0.2:1;

hold on

for i = 1:5

So1 =  (1-Sw1 );   %Oil saturation

Rsat1 = Rmat.*(1-phi)+(So1.*Roil + Sw1.*Rw).*phi;

ROH = Rsat1./1000;

Mu1 = (Vs1.^2.* Rsat1);

MU = Mu1./1000000

Ksat1 = Vp1.^2.*2.32- 4/3.*Mu1;

KSAT1 = Ksat1./1000000;

VPinsitu = (sqrt((KSAT1+((4/3).*MU))./2.32)).*1000;

tet2 =(asp2./((1-asp2.^2).^(3/2))).*(acos(asp2)-(asp2.*sqrt(1-asp2.^2)));

g2 = ((asp2.^2)./(1-asp2.^2)).*((3.*tet2)-2);

KU = Km./Um;

z = (1./(pi.*asp2))-(1./(pi.*asp2.*((3.*Km./(Um +1)))));

%%%%%%%%%%%%%%%%%%%%%Assuming Penny Cracks%%%%%%%%%%%%%%%%%%%%%

v1 = Km/Um;

v2 =((3*Km)/Um)+ 4 ;

v3 = ((3*Km)/Um)+ 1 ;

v4 = ((3*Km)/Um)+ 2 ;


a = (-1.*(1/5))+(KU.*v2./(pi.*asp2*(v3))) - (4.*v2./(15.*pi.*asp2.*(v3))) - (8.*v2./(15.*pi.*asp2.*(v4))) -

(KU .* ((1./pi.*asp2) + (27./(5.*pi.*asp2.*v3.^2)) + (16./(5.*pi.*asp2.*v4.^2))));

b=(1./pi.*asp2) + (27./(5.*pi.*asp2.*v3.^2)) + (16./(5.*pi.*asp2.*v4.^2));

x = (2- (3.*g2) - (2.*tet2))./(2 .* ((2.*tet2)- (3.*tet2.^2) - (2.*g2)))

KDRY1 = Km.*((1-phi).^z./(1 + (b./a).*KU - (b./a).*KU.*(1 - phi).^a).^(x./b))

axes(handles.axes3)
```

```
s=scatter(phi, KDRY1(:,1),'.');
s.LineWidth = 0.6;
s.MarkerEdgeColor = 'k';
s.MarkerFaceColor = [0 0 0];
grid on

xlim([0.02 0.1])
ylim([20 45])
hold on
s5=scatter(phi, KDRY1(:,2),'.');
s5.LineWidth = 0.6;
s5.MarkerEdgeColor = 'b';
s5.MarkerFaceColor = [0 0 0];
grid on

hold on
s5=scatter(phi, bulklog,'.');
s5.LineWidth = 0.6;
s5.MarkerEdgeColor = 'm';
s5.MarkerFaceColor = [0 0 0];
grid on
hold on
s5=scatter(phi, KDRY1(:,4),'.');
s5.LineWidth = 0.6;
s5.MarkerEdgeColor = 'r';
s5.MarkerFaceColor = [0 0 0];
grid on
hold on
```

```
s5=scatter(phi, KDRY1(:,5),'.');
s5.LineWidth = 0.6;
s5.MarkerEdgeColor = 'g';
s5.MarkerFaceColor = [0 0 0];
grid on
hold on
s5=scatter(phi, KDRY1(:,5),'.');
s5.LineWidth = 0.6;
s5.MarkerEdgeColor = 'g';
s5.MarkerFaceColor = [0 0 0];
hold on
f2=toc;
s5=scatter(phi, bulklog,45,f2,'filled');
s5.LineWidth = 0.9;
s5.MarkerEdgeColor = 'k';
s5.MarkerFaceColor = [0 0.9 0.1];
grid on
end
title('DEM analysis Phi vs Bulk Modulus    \alpha=aspect ratio')
xlabel('PHI (dec)')
ylabel('Bulk Modulus (GPa) DEM')
legend('\alpha=0.1','\alpha=0.3','\alpha=0.5','\alpha=0.7','\alpha=0.9','log samples')
% --- Executes on selection change in popupmenu1.
function popupmenu1_Callback(hObject, eventdata, handles)
% hObject    handle to popupmenu1 (see GCBO)
% eventdata  reserved - to be defined in a future version of MATLAB
% handles    structure with handles and user data (see GUIDATA)
% Hints: contents = cellstr(get(hObject,'String')) returns popupmenu1 contents as cell array
```

```
%       contents{get(hObject,'Value')} returns selected item from popupmenu1
global Vp1 vclay toc popVal popVal1 popVal2 popVal3


contents = cellstr(get(hObject,'String'));
popChoice = contents{get(hObject,'Value')};
assignin('base','popChoice',popChoice);
if (strcmp(popChoice,'Vp'))
   popVal = Vp1;
elseif (strcmp(popChoice,'Vclay'))
popVal = vclay;
elseif (strcmp(popChoice,'TOC'))
popVal = toc;
end
assignin('base','popVal',popVal)
guidata(hObject, handles);
% --- Executes during object creation, after setting all properties.
function popupmenu1_CreateFcn(hObject, eventdata, handles)
% hObject    handle to popupmenu1 (see GCBO)
% eventdata  reserved - to be defined in a future version of MATLAB
% handles    empty - handles not created until after all CreateFcns called
% Hint: popupmenu controls usually have a white background on Windows.
%       See ISPC and COMPUTER.
if ispc && isequal(get(hObject,'BackgroundColor'), get(0,'defaultUicontrolBackgroundColor'))
set(hObject,'BackgroundColor','white');
end
% --- Executes on selection change in popupmenu2.
function popupmenu2_Callback(hObject, eventdata, handles)
% hObject    handle to popupmenu2 (see GCBO)
```

```
% eventdata  reserved - to be defined in a future version of MATLAB
% handles    structure with handles and user data (see GUIDATA)
% Hints: contents = cellstr(get(hObject,'String')) returns popupmenu2 contents as cell array
%        contents{get(hObject,'Value')} returns selected item from popupmenu2
global Vp1 vclay toc


contents = cellstr(get(hObject,'String'));
popChoice = contents{get(hObject,'Value')};
assignin('base','popChoice',popChoice);
if (strcmp(popChoice,'Vp'))
popVal1 = Vp1;
elseif (strcmp(popChoice,'Vclay'))
popVal1 = vclay;
elseif (strcmp(popChoice,'TOC'))
popVal1 = toc;
end
assignin('base','popVal1',popVal1)
guidata(hObject, handles);
% --- Executes during object creation, after setting all properties.
function popupmenu2_CreateFcn(hObject, eventdata, handles)
% hObject    handle to popupmenu2 (see GCBO)
% eventdata  reserved - to be defined in a future version of MATLAB
% handles    empty - handles not created until after all CreateFcns called
% Hint: popupmenu controls usually have a white background on Windows.
%       See ISPC and COMPUTER.
if ispc && isequal(get(hObject,'BackgroundColor'), get(0,'defaultUicontrolBackgroundColor'))
set(hObject,'BackgroundColor','white');
end
```

```
% --- Executes on selection change in popupmenu3.
function popupmenu3_Callback(hObject, eventdata, handles)
% hObject    handle to popupmenu3 (see GCBO)
% eventdata  reserved - to be defined in a future version of MATLAB
% handles    structure with handles and user data (see GUIDATA)
% Hints: contents = cellstr(get(hObject,'String')) returns popupmenu3 contents as cell array
%        contents{get(hObject,'Value')} returns selected item from popupmenu3
global Vp1 vclay toc popVal popVal1 popVal2 popVal3


contents = cellstr(get(hObject,'String'));
popChoice = contents{get(hObject,'Value')};
assignin('base','popChoice',popChoice);
if (strcmp(popChoice,'Vp'))
popVal2 = Vp1;
elseif (strcmp(popChoice,'Vclay'))
popVal2 = vclay;
elseif (strcmp(popChoice,'TOC'))
popVal2 = toc;
end
assignin('base','popVal2',popVal2)
guidata(hObject, handles);
% --- Executes during object creation, after setting all properties.
function popupmenu3_CreateFcn(hObject, eventdata, handles)
% hObject    handle to popupmenu3 (see GCBO)
% eventdata  reserved - to be defined in a future version of MATLAB
% handles    empty - handles not created until after all CreateFcns called
% Hint: popupmenu controls usually have a white background on Windows.
% See ISPC and COMPUTER.
```

```
if ispc && isequal(get(hObject,'BackgroundColor'), get(0,'defaultUicontrolBackgroundColor'))
    set(hObject,'BackgroundColor','white');
end



% --- Executes on selection change in popupmenu4.
function popupmenu4_Callback(hObject, eventdata, handles)
% hObject    handle to popupmenu4 (see GCBO)
% eventdata  reserved - to be defined in a future version of MATLAB
% handles    structure with handles and user data (see GUIDATA)
% Hints: contents = cellstr(get(hObject,'String')) returns popupmenu4 contents as cell array
%        contents{get(hObject,'Value')} returns selected item from popupmenu4
global Vp1 vclay toc popVal popVal1 popVal2 popVal3


contents = cellstr(get(hObject,'String'));
popChoice = contents{get(hObject,'Value')};
assignin('base','popChoice',popChoice);


if (strcmp(popChoice,'Vp'))
popVal3 = Vp1;
elseif (strcmp(popChoice,'Vclay'))
popVal3 = vclay;
elseif (strcmp(popChoice,'TOC'))
popVal3 = toc;
end
assignin('base','popVal3',popVal3)
guidata(hObject, handles);
```

```
% --- Executes during object creation, after setting all properties.
function popupmenu4_CreateFcn(hObject, eventdata, handles)
% hObject    handle to popupmenu4 (see GCBO)
% eventdata  reserved - to be defined in a future version of MATLAB
% handles    empty - handles not created until after all CreateFcns called
% Hint: popupmenu controls usually have a white background on Windows.
%       See ISPC and COMPUTER.
if ispc && isequal(get(hObject,'BackgroundColor'), get(0,'defaultUicontrolBackgroundColor'))
    set(hObject,'BackgroundColor','white');
end
% --- Executes on button press in pushbutton4.
function pushbutton4_Callback(hObject, eventdata, handles)
% hObject    handle to pushbutton4 (see GCBO)
% eventdata  reserved - to be defined in a future version of MATLAB
% handles    structure with handles and user data (see GUIDATA)


x = evalin('base','popVal');
y = evalin('base','popVal1');
z = evalin('base','popVal2');
C1 = evalin('base','popVal3');


axes(handles.axes4)


sr = scatter3(x,y,z,30,C1,'filled')
sr.MarkerEdgeColor = 'k';
InteractiveColorbar
```

```
grid on

set(gca, 'Projection','perspective')


title('3D Crossplot')

get(hObject,'Value')

xlabel('x')

ylabel('y')

zlabel('z')

guidata(hObject, handles);
```

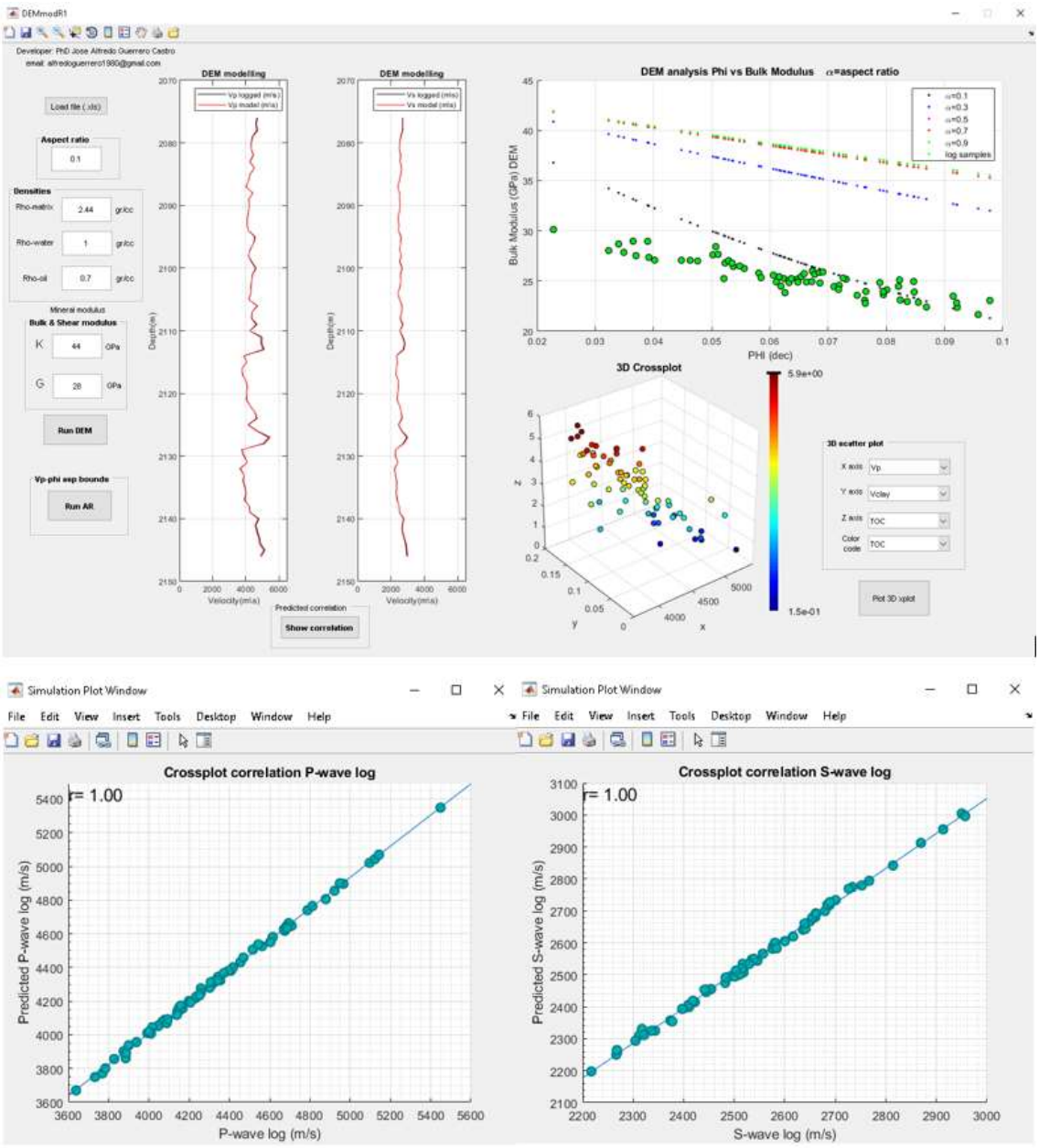

DEMmodR1 GUI graphical user interface